ON THE CHARACTERISTICS OF DIVIDING STEAM-WATER FLOW IN A HORIZONTAL TEE JUNCTION

ON THE CHARACTERISTICS OF DIVIDING STEAM-WATER FLOW IN A HORIZONTAL TEE JUNCTION

By

JOHN D. BALLYK, B.Sc., B.Eng.

A Thesis
Submitted to the School of Graduate Studies
in Partial Fulfilment of the Requirements
for the Degree
Master of Engineering

McMaster University

December 1986

TO MY PARENTS

MASTER OF ENGINEERING (1986)
(Mechanical)

McMASTER UNIVERSITY
Hamilton, Ontario

TITLE: On the Characteristics of Dividing Steam-Water Flow in a Horizontal Tee Junction

AUTHOR: John D. Ballyk, B.Sc., B.Eng. (Memorial University)

SUPERVISOR: Dr. M. Shoukri

NUMBER OF PAGES: (xiii) 117

ABSTRACT

The results of an experimental investigation of the separation phenomena in dividing two-phase flow is presented. This work involved the commissioning of a steam-water loop to obtain detailed data on the characteristics of steam-water flow in a horizontal tee junction. Measurements included the pressure and void fraction distributions as well as the total flow rate and quality along the inlet and branching legs. A detailed set of experiments were performed enabling the effects of flow split, inlet quality and inlet mass flux on the separation and pressure characteristics to be determined.

For the annular inlet flow conditions considered herein, total separation was approached when more than 40% of the inlet flow was removed through the branch. At lower branch flow rates, the degree of phase separation was strongly dependent on the branch flow split and the inlet quality.

The pressure change from the inlet through the run of the tee was modelled from an axial momentum balance at the junction for both homogeneous and separated flow assumptions. The separated flow momentum correction factor was distributed about a value of unity indicating that the branching flow carriers little or no axial component of momentum. The pressure change from the inlet through the branch was considered in terms of reversible and irreversible components for separated and homogeneous flow assumptions. Both models yielded loss coefficients that were strongly dependent on the branch flow split and inlet quality.

ACKNOWLEDGEMENTS

The author wishes to express his appreciation to Dr. M. Shoukri for his supervision and guidance throughout the course of this study.

A sincere thank you to Mr. A. Calka for his supervision of the loop construction and to Mr. G. Spies for his assistance in data collection.

Thanks are also extended to Mr. D.P. Schick and Mr. J. Verhaeghe for their aid in technical matters.

Thanks are due to Ontario Hydro and the Canadian Electrical Association for the opportunity to be involved in this project (CEA #325-G430). The financial support of the Natural Sciences and Engineering Research Council of Canada is greatly appreciated.

The author is especially grateful to his wife, Cathy, and children, Laura and Matthew, for their love and patience.

TABLE OF CONTENTS

		Page
NOMENCLATURE		vii
LIST OF FIGURES		ix
LIST OF TABLES		xiii
CHAPTER 1	**INTRODUCTION**	1
CHAPTER 2	**LITERATURE SURVEY**	3
2.1	**Two-Phase Flow Regimes**	3
2.2	**Two-Phase Flow Division in Tee Junctions**	9
	2.2.1 Introduction	9
	2.2.2 Phase Separation	11
	2.2.3 Phase Separation Modelling	13
	2.2.4 Correlation of Pressure Distribution	17
CHAPTER 3	**EXPERIMENTAL ARRANGEMENTS**	21
3.1	**Experimental Facility**	21
	3.1.1 Steam-Water Loop	21
	3.1.2 Two-Phase Mixer	23
	3.1.3 Test Section	27
3.2	**Measurement and Calibration**	30
	3.2.1 Water Flow Rate Measurements	30
	3.2.2 Steam Flow Rate Measurements	30
	3.2.3 Temperature Measurements	31
	3.2.4 Pressure Distribution Measurements	33
	3.2.5 Void Fraction Measurements	35
	3.2.6 Data Acquisition System	39
	3.2.7 Computational Procedure for Data Reduction	39
3.3	**System Operation**	43
	3.3.1 Start up Procedure	43
	3.3.2 Test Procedure	44
	3.3.3 Shut Down Procedure	46
	3.3.4 Test Conditions	46

TABLE OF CONTENTS (Continued)

		Page
CHAPTER 4	**RESULTS AND DISCUSSION**	48
4.1	**Phase and Energy Balances**	48
4.2	**Phase Separation**	49
	4.2.1 Effect of Inlet Quality	58
	4.2.2 Effect of Inlet Mass Flux	62
4.3	**Single Phase Pressure Distribution**	62
	4.3.1 Axial Pressure Recovery	65
	4.3.2 Radial Pressure Drop	68
4.4	**Two-Phase Pressure Distribution**	72
	4.4.1 Two-Phase Axial Pressure Recovery	72
	4.4.2 Two-Phase Radial Pressure Drop	84
CHAPTER 5	**CONCLUSIONS AND RECOMMENDATIONS**	91
REFERENCES		93
APPENDIX A	**CALIBRATION DATA**	95
APPENDIX B	**GAMMA DENSITOMETER**	103
B.1	Operating Principle	103
B.2	Densitometer Design	104
APPENDIX C	**SATURATED WATER AND STEAM PROPERTIES**	111
APPENDIX D	**EXPERIMENTAL DATA**	112

NOMENCLATURE

A	= Cross sectional area	
D	= Diameter	
E	= Energy	
F_d	= Volumetric interfacial drag force	
F_w	= Volumetric wall drag force	
G	= Mass flux	
h	= enthalpy	
J	= Superficial velocity	
k_{1-2}	= Axial momentum correction factor	
k_{1-3}	= Branch loss coefficient	
$\dot{m}$	= Mass flow rate	
N	= Photon Count	
P	= Pressure	
$(\Delta P_{2-1})_j$	= Run junction pressure differential	
$(\Delta P_{1-3})_j$	= Branch junction pressure differential	
S	= Correlation parameter	(eqn. 2.3)
u	= Velocity	
x	= Quality	

Subscripts

1	= Inlet
2	= Run
3	= Branch
a	= Air
c	= Condensate
cw	= Cooling water
g	= Gas
h	= Homogeneous
i	= In
irrev	= Irreversible
j	= Junction
ℓ	= Liquid

Nomenclature (Continued)

m	= Mixer	
nom	= Nominal	
o	= Out	
rev	= Reversible	
s	= Separated flow	
t	= Test section	
w	= Water	

Greek Symbols

α	= Void fraction	
γ	= Pipe angle of inclination	
θ	= Correlation parameter	(eqn. 2.6)
θ'	= Correlation parameter	(eqn. 2.9)
λ	= Fluid property correction factor	(eqn. 2.2)
μ	= Dynamic viscosity	
ρ	= Density	
ρ'	= Momentum weighted density	(eqn. 4.20)
ρ'''	= Energy weighted density	(eqn. 2.27)
σ	= Surface tension	
Φ	= Branch two-phase multiplier	
ψ	= Fluid property correction factor	(eqn. 2.1)

LIST OF FIGURES

		Page
2.1	Flow Regimes in Horizontal Two-Phase Flow	4
2.2	Flow Regime Map Proposed by Baker [3]	7
2.3	Correction Factors (λ and ψ) for Steam-Water Flow (after [4])	7
2.4	Flow Regime Map Proposed by Mandhane et al. [5]	8
2.5	Comparison of Theoretical and Experimental Transition Boundaries for Air-Water Flow (1 bar, 25°C, 25mm I.D.)	10
2.6	Nomenclature Used for Two-Phase Flow in a Tee Junction	10
2.7	Control Volume for an Axial Momentum Balance at a Tee Junction	18
3.1	Schematic Diagram of the Steam-Water Loop	22
3.2	Overall View of the Experimental Facility	24
3.3	Measurement Systems at the Test Section	25
3.4	Two-Phase Mixer	26
3.5	Schematic Diagram of the Test Section	28
3.6	Test Section	29
3.7	Orifice Meter Assembly	32
3.8	Schematic Diagram of the Pressure Measurement System	34
3.9	Signal Processing System for Void Fraction Measurements	36
3.10	Void Fraction Measurement System	37
3.11	Void Fraction Measurement Stations	38
3.12	Data Acquisition System	40
3.13	Schematic Diagram of a Typical Pressure Distribution in Dividing Flow	42

LIST OF FIGURES (Continued)

		Page
4.1	Branch Quality vs. Flow Split (G_1 = 450 kg/m^{2}s, x_1 = 4.7%)	50
4.2	Branch Quality vs. Flow Split (G_1 = 450 kg/m^{2}s, x_1 = 15.2%)	51
4.3	Branch Quality vs. Flow Split (G_1 = 600 kg/m^2/s, x_1 = 2.2%)	52
4.4	Branch Quality vs. Flow Split (G_1 = 600 kg/m^{2}s, x_1 = 4.6%)	53
4.5	Branch Quality vs. Flow Split (G_1 = 600 kg/m^{2}s, x_1 = 8.0%)	54
4.6	Branch Quality vs. Flow Split (G_1 = 900 kg/m^{2}s, x_1 = 2.0%)	55
4.7	Branch Quality vs. Flow Split (G_1 = 900 kg/m^{2}s, x_1 = 4.3%)	56
4.8	Branch Quality vs. Flow Split (G_1 = 1200 kg/m^{2}s, x_1 = 2.0%)	57
4.9	Branch Phase Separation Ratio vs. Flow Split, Effect of Inlet Quality (G_1 = 450 kg/m^{2}s)	59
4.10	Branch Phase Separation Ratio vs. Flow Split, Effect of Inlet Quality (G_1 = 600 kg/m^{2}s)	60
4.11	Branch Phase Separation Ratio vs. Flow Split, Effect of Inlet Quality (G_1 = 900 kg/m^{2}s)	61
4.12	Branch Phase Separation Ratio vs. Flow Split, Effect of Inlet Mass Flux (x_1 = 2.1%)	63
4.13	Branch Phase Separation Ratio vs. Flow Split, Effect of Inlet Mass Flux (x_1 = 4.5%)	64
4.14	Single Phase Pressure Distribution (G_1 = 900 kg/m^{2}s, $\dot{m}_3/\dot{m}_1$ = 0.7)	66
4.15	Single Phase Axial Pressure Rise and Momentum Correction Factor vs. Flow Split	67
4.16	Single Phase Axial Pressure Rise vs. Flow Split (after [18])	69
4.17	Single Phase Branch Loss Coefficient vs. Flow Split	70

LIST OF FIGURES (Continued)

		Page
4.18	Single Phase Branch Loss Coefficient vs. Flow Split (after [18])	71
4.19	Two-Phase Pressure Distribution (G_1 = 600 kg/m^{2}s, x_1 = 4.5%, $\dot{m}_3/\dot{m}_1$ = 0.18)	73
4.20	Two-Phase Pressure Distribution (G_1 = 600 kg/m^{2}s, x_1 = 4.9%, $\dot{m}_3/\dot{m}_1$ = 0.31)	74
4.21	Void Fraction Distribution (G_1 = 600 kg/m^{2}s, x_1 = 4.5%, $\dot{m}_3/\dot{m}_1$ = 0.18)	75
4.22	Void Fraction Distribution (G_1 = 600 kg/m^{2}s, x_1 = 4.9%, $\dot{m}_3/\dot{m}_1$ = 0.31)	76
4.23	Run Flow Conditions Plotted on Baker's Map (G_1 = 600 kg/m^{2}s, x_1 = 4.6%)	77
4.24	Homogeneous Momentum Correction Factor vs. Flow Split, Effect of Inlet Mass Flux (x_1 = 2.1%)	79
4.25	Homogeneous Momentum Correction Factor vs. Flow Split, Effect of Inlet Quality (G_1 = 600 kg/m^{2}s)	80
4.26	Separated Flow Momentum Correction Factor vs. Flow Split, Effect of Inlet Mass Flux (x_1 = 2.1%)	82
4.27	Separated Flow Momentum Correction Factor vs. Flow Split, Effect of Inlet Quality (G_1 = 600 kg/m^{2}s)	83
4.28	Homogeneous Two-Phase Multiplier vs. Flow Split, Effect of Inlet Quality (G_1 = 600 kg/m^{2}s)	85
4.29	Homogeneous Two-Phase Multiplier vs. Flow Split, Effect of Inlet Mass Flux (x_1 = 2.1%)	87

LIST OF FIGURES (Continued)

		Page
4.30	Separated Flow Two-Phase Multiplier vs. Flow Split, Effect of Inlet Quality (G_1 = 600 kg/m^{2}s)	88
4.31	Separated Flow Two-Phase Multiplier vs. Flow Split, Effect of Inlet Mass Flux (x_1 = 2.1%)	90
A.1	Calibration Results for the Orifice Meter	97
A.2	Calibration Results for Pressure Transducer DP15-36	98
A.3	Calibration Results for Pressure Transducer DP15-38	99
A.4	Calibration Results for Pressure Transducer DP15-46	100
A.5	Calibration Results for Pressure Transducer DP103-20	101
A.6	Calibration Results for Pressure Transducer DP103-28	102
B.1	Test Section Cross Section for Gamma Densitometer Design	105
B.2	Gamma Densitometer Source Casket	110

LIST OF TABLES

		Page
2.1	Applicable Parameter Ranges for Map by Mandhane et al. [5]	8
3.1	Single Phase Test Conditions	47
3.2	Two-Phase Test Conditions	47
B.1	Shielding Thickness/weight	109
D.1	Single Phase Data	113
D.2	Two-Phase Data for $G_l = 450$ kg/m^{2}s	114
D.3	Two-Phase Data for $G_l = 600$ kg/m^{2}s	115
D.4	Two-Phase Data for $G_l = 900$ kg/m^{2}s	116
D.5	Two-Phase Data for $G_l = 1200$ kg/m^{2}s	117

CHAPTER 1

INTRODUCTION

Dividing and combining two-phase flows are encountered in many engineering systems in the power and process industries. A particular case of interest is that of loss-of-coolant accident (LOCA) in nuclear reactor safety analysis. This requires the accurate prediction of phase and pressure distribution for steam-water flow in complex branching conduits. Since the behaviour of two-phase flows in such situations is not well understood, it is commonly assumed that the quality in all downstream legs of a manifold are equal and hence equal to the inlet quality. Experimental evidence indicates that this assumption may be significantly in error. Under most conditions, the two phases separate at flow junctions with the gas phase preferentially entering the branching port.

Experimental investigations carried out to date have shown the separation phenomena to be dependent on a variety of hydraulic and geometrical parameters. These include inlet quality, flow regime and mass flux, the system pressure and orientation with respect to gravity and the branch to inlet ratios of diameter and flow rate. Due to the large number of parameters involved, empirically based models would be impractical to develop. A more realistic approach is to model the flow behaviour by identifying the governing mechanisms, applying the appropriate conservation laws and closing with experimentally based constitutive equations.

In the present work, the results of an experimental investigation into the characteristics of dividing steam-water flow are presented. The experimental facility assembled at McMaster University allowed for measured amounts of steam and water to be

mixed to thermodynamic equilibrium and delivered to a horizontal tee test section. The measurement systems allowed the time averaged distributions of pressure and void fraction and the flow quality in each leg of the tee to be determined. A set of detailed experiments were carried out to isolate the effects of inlet mass flux, inlet quality and branch flow split on the measured parameters.

CHAPTER 2

LITERATURE SURVEY

2.1 Two-Phase Flow Regimes

Analysis of a single phase flow requires identification of the flow regime (laminar or turbulent) established within the system. Transition from one regime to the other is predicted by the Reynolds number and the physical properties of the system. These regimes require different models to accurately describe the existing physical phenomena.

Similarly, flow regimes significantly affect the constitutive equations used in modelling a two-phase flow. A two-phase system is more complex in that the number of possible flow regimes greatly increases, their transition boundaries are not well defined and there are numerous fluid and system properties affecting the occurrence of a particular regime.

Two-phase flow regimes are characterized by the distribution of the phases in the conduit cross section. For horizontal flow in a pipe it is generally accepted that six flow regimes can be identified. The classification proposed by Alves [1] is shown in Figure 2.1. Physical descriptions of these flow regimes and transition mechanisms suggested by Taitel and Dukler [2] are outlined below.

Bubble Flow: When a gas and a liquid flow together in a pipe, gravity will tend to separate the two phases. For high liquid and low gas flow rates, the liquid level in the pipe is high and turbulent fluctuations tend to break up any gas pockets. When turbulent forces exceed buoyant forces the gas phase flows as dispersed bubbles in the upper portion of the pipe.

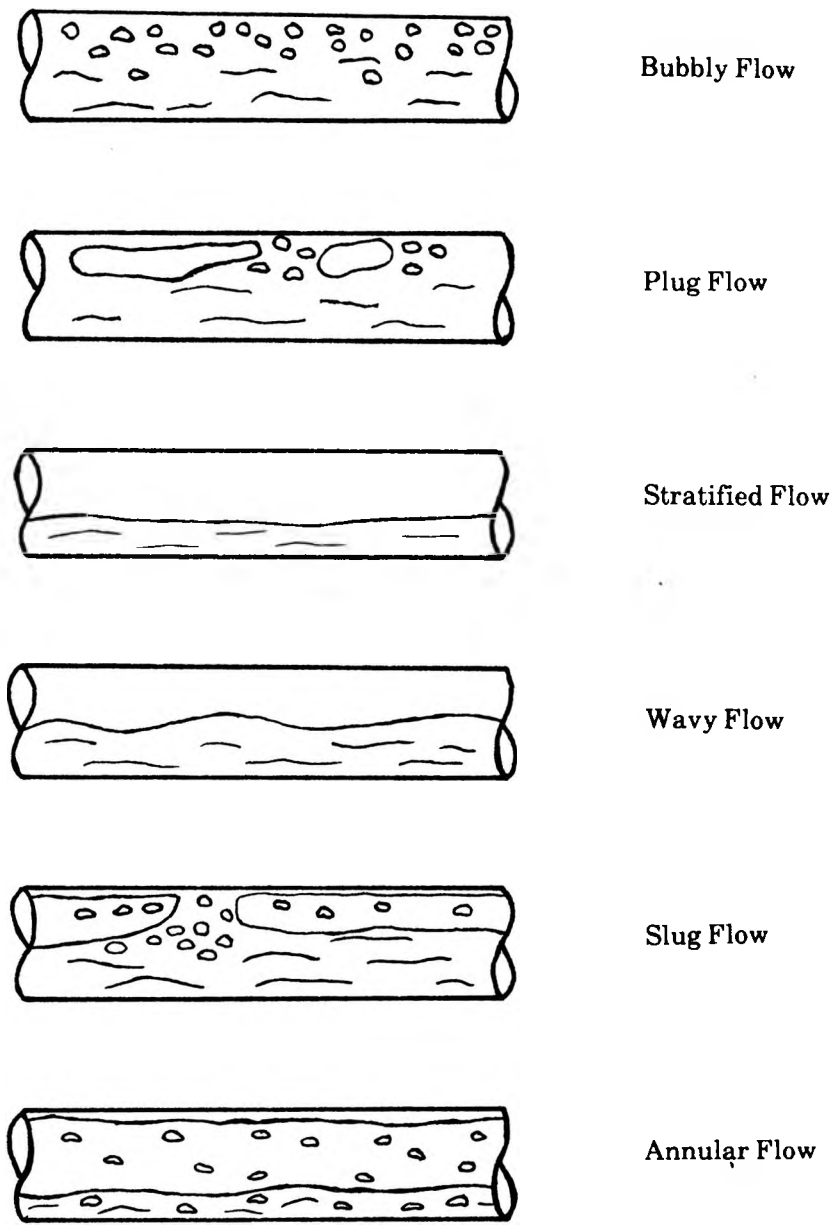

Figure 2.1 Flow Regimes in Horizontal Two-Phase Flow

Plug Flow: At lower liquid flow rates the turbulent fluctuations decrease allowing some of the bubbles to coalese into larger bubbles. These flow as gas plugs at the top of the pipe.

Stratified Flow: At still lower liquid flowrates the gas plugs may coalese and the gas and liquid phases flow separately. For sufficiently low gas flow rates, the interface between the two phases remains smooth.

Wavy Flow: When the two phases flow separately, energy is transferred from the higher velocity gas to the liquid on the sloping surface of a wave. This wave action will tend to dampen itself out due to viscous dissipation. If the energy transferred is less than that dissipated the wave will decay and the surface remains smooth. If transferred energy exceeds dissipated energy the wave will grow and the interface between the two phases appears wavy.

Slug Flow: For increased liquid flow rates the mean liquid level in the pipe is higher and the gas velocity must increase. As the gas flows over the peak of a wave it must accelerate and the pressure decreases due to Bernoulli effects. A force is then acting upward on the volume of the wave as gravity tends to pull it downward. The wave will grow when the pressure forces exceed gravitational forces. For sufficiently high liquid flow rates these waves may bridge the entire pipe forming liquid slugs between gas pockets. The slug velocity is generally higher than the mean fluid velocity.

Annular Flow: At very high gas flow rates the liquid level is not sufficient to form a complete bridge of the pipe. The liquid is then swept around the pipe to form an annular flow with a thicker layer of liquid at the bottom. Depending on the relative flow rates of the two phases, the high velocity gas core will carry varying amounts of entrained liquid droplets.

In the development of sophisticated two-phase flow models, separate conservation equations may be written for each phase. For this application it is convenient to combine these flow regimes into three categories based on the degree of coupling between the two

phases. Annular and stratified flows are called "separated" flows because the vapour and liquid streams are, in general, continuous and loosely coupled. Bubbly and droplet flows can be distinguished by the existence of a continuous phase and a dispersed phase. These are classified as "distributed" flows. Due to the intermittent nature of slug and plug flow they are grouped together as "intermittent" flows.

Two methods have been used for predicting the occurrence of these flow regimes. They are (i) the correlation of experimental data in terms of two dimensional maps, (ii) the development of physically based models for flow regime transitions.

One of the earliest flow regime maps for horizontal pipes still commonly used today is that of Baker [3] shown in Figure 2.2. Baker's map is a plot of the superficial gas mass flux (Gx) versus the superficial liquid mass flux (G(1 – x)), where G is the total mass flux and x is the flow quality. For mixtures other than low pressure air and water, Baker incorporated correction factors defined as

$$\lambda = \left[\left(\frac{\rho_g}{\rho_a}\right)\left(\frac{\rho_\ell}{\rho_w}\right)\right]^{1/2} \tag{2.1}$$

and

$$\psi = \left(\frac{\sigma_w}{\sigma_\ell}\right)\left[\left(\frac{\mu_\ell}{\mu_w}\right)\left(\frac{\rho_w}{\rho_\ell}\right)^2\right]^{1/3} \tag{2.2}$$

where ρ, σ and μ refer to density, surface tension and dynamic viscosity respectively. Subscripts a and w indicate the physical properties of air and water at atmospheric pressure and 20°C. Subscripts g and ℓ refer to the properties of the flowing gas and liquid respectively. These factors are used as shown in Figure 2.2. Collier [4] presented the values of λ and ψ for steam-water flow as shown in Figure 2.3.

More recently, Mandhane et al. [5] developed the two dimensional map shown in Figure 2.4 from a large two-phase data bank. The effect of fluid properties on the proposed map is not as significant as implied in the Baker map [3]. The coordinates are the superficial

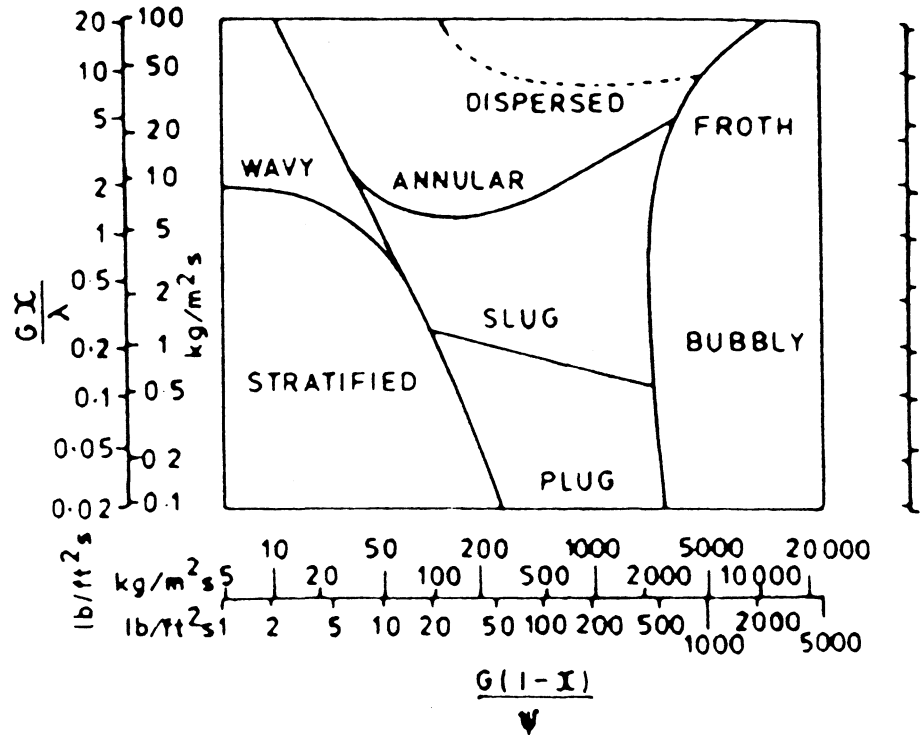

Figure 2.2 Flow Regime Map Proposed by Baker [3]

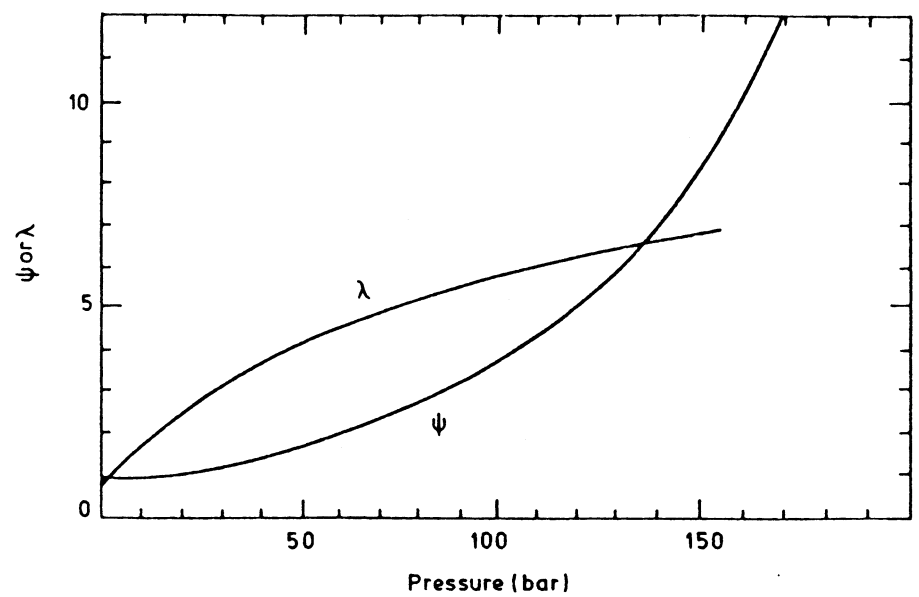

Figure 2.3 Correction Factors (λ and ψ) for Steam-Water Flow (after [4])

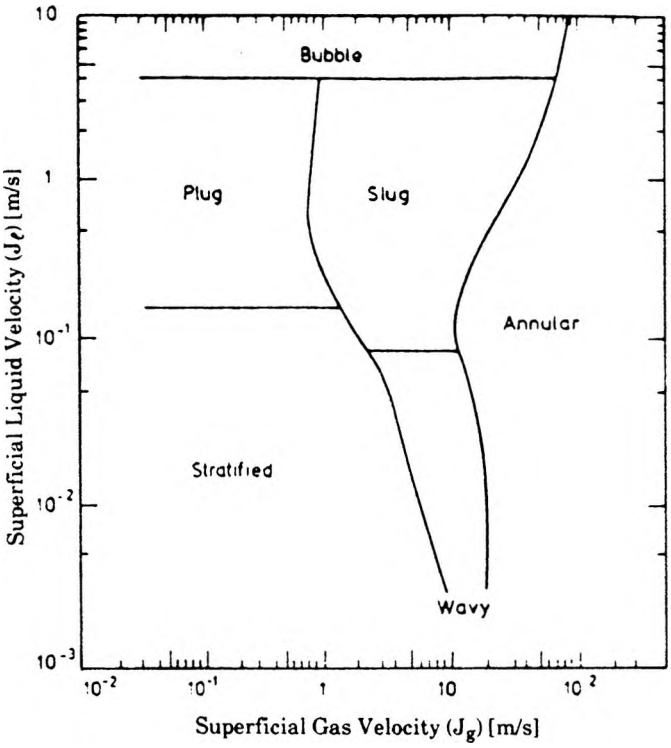

Figure 2.4 Flow Regime Map Proposed by Mandhane et. al. [5]

TABLE 2.1 APPLICABLE PARAMETER RANGES FOR MAP BY MANDHANE et. al. [5]

Pipe Inner Diameter	12.7 – 165.1	[mm]
Liquid Phase Density	705 – 1009	[kg/m^3]
Gas Phase Density	0.80 – 50.5	[kg/m^3]
Liquid Phase Viscosity	$3 \times 10^{-4} - 9 \times 10^{-2}$	[kg/ms]
Gas Phase Viscosity	$10^{-5} - 2.2 \times 10^{-5}$	[kg/ms]
Surface Tension	0.024 – .103	[N/m]
Superficial Liquid Velocity	$9 \times 10^{-4} - 7.31$	[m/s]
Superficial Gas Velocity	0.04 – 171	[m/s]

liquid velocity (J_ℓ) and superficial gas velocity (J_g) calculated at the system temperature and pressure. The applicable parameter ranges from Mandhane et al. are shown in table 2.1.

From a theoretical analysis of the transition mechanism between flow regimes Taitel and Dukler [2] predicted the general trends of Mandhane's map [5]. The models suggested by Taitel et al. also include the pipe angle of inclination. A comparison between the Taitel and Dukler theoretical map and the empirical map of Mandhane for a horizontal air-water mixture at 1 bar and 25°C is shown in Figure 2.5.

2.2 Two Phase Flow Division in Tee Junctions

2.2.1 Introduction

Most experimental investigations into the division of two-phase flows have been carried out with single tee junctions as shown schematically in Figure 2.6. Throughout this thesis the nomenclature used will be as shown, with subscripts 1, 2, and 3 referring to the inlet, run and branch respectively.

The characteristics of interest in the analysis of dividing two-phase flow are the phase and pressure distributions within the branching conduits. Experimental evidence indicates that a large degree of phase separation occurs under most flow conditions with the gas phase preferentially entering the branch. The flow in the axial direction past the branching port experiences a pressure rise as predicted by an axial momentum balance at the junction. A pressure drop is experienced by the dividing flow as it accelerates into the branch.

For engineering applications in two-phase flow, steam and water is most often the gas-liquid combination of interest. Very few data has been reported in the literature for steam-water separation phenomena. Experimentally, it is more convenient to use a non-condensible mixture such as air and water. This reduces equipment and energy requirements

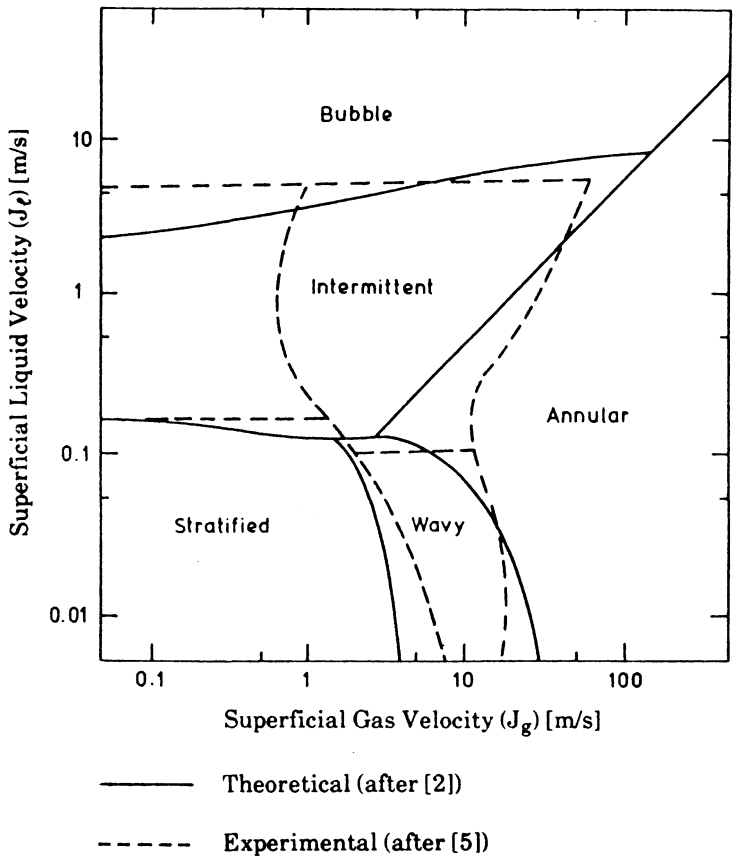

Figure 2.5 Comparison of Theoretical [2] and Experimental [5] Transition Boundaries for Air-Water Flow (1 bar, 25°C, 25mm I.D.)

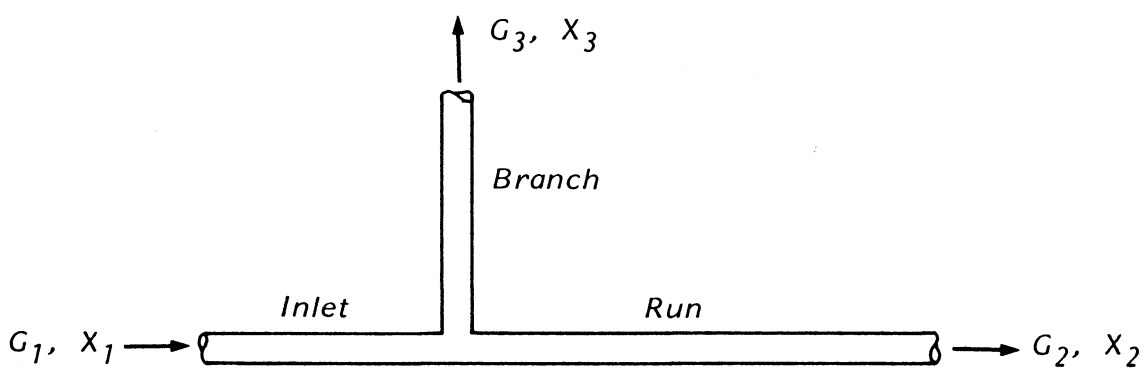

Figure 2.6 Nomenclature Used for Two-Phase Flow in a Tee Junction

and the two phases are easily separated for flow measurements. Virtually all experimental work to date has been carried out with air-water mixtures. A further simplification has been made by most investigators in considering an isolated tee junction under fully developed conditions. More complex geometries may then be analyzsed in terms of deviations from these results.

These investigations have shown the separation phenomena to be dependent on a variety of hydraulic and geometrical parameters. These include inlet flow regime, inlet quality, inlet mass flux, branch to inlet flow ratio, branch to inlet diameter ratio and the system orientation with respect to gravity.

2.2.2 Phase Separation

From their investigation of air-water flow in a horizontal tee section, St. Pierre and Glastonbury [6] reported that separation was more pronounced for annular inlet flows than for stratified flows. The authors suggested that in stratified flow, a larger portion of the liquid is travelling at a low velocity relative to annular flow enhancing liquid take off. Azzopardi and Whalley [7] investigated the separation phenomena of air-water flow in vertical tee sections. The authors explained the influence of flow regimes in terms of their effect on the distribution of axial momentum flux through the tube cross section. It was suggested that the liquid with a momentum flux near that of the gas is diverted into the branch. In annular flow, the liquid removed then comes from the low velocity liquid film flowing at the tube walls. In bubbly flow the momentum flux of the gas is significantly lower than that of the bulk fluid, due to a lower slip ratio, enhancing gas removal.

Henry [8] investigated the separation phenomena with annular flow in a horizontal tee section. His results and those of Azzopardi and Whalley [7] indicated that the rate of liquid removal through the branch will approach some limiting value as the gas removal rate

approaches zero. This implies that for small values of flow split the branch quality will be lower than the inlet quality. The branch quality increased with increasing flow split eventually leveling off at some value above that of the inlet [8]. This trend must reverse for higher flow splits since the branch and inlet qualities must be equal when all the flow is diverted through the branch. Honan and Lahey [9] and Saba and Lahey [10] reported decreasing branch quality with increasing flow split for greater than 30% of the flow removed through the branch.

St. Pierre and Glastonbury [6] reported that for a constant inlet mass flux under stratified and slug flow conditions in a horizontal tee, phase separation became more pronounced with increasing quality. Increasing inlet quality requires the liquid level in the test section to fall resulting in a reduced portion of the banching port being bridged by liquid. This coupled with the increased liquid momentum inhibits liquid take off.

St. Pierre and Glastonbury [6] further reported that separation became less severe with increasing quality for annular inlet flows in a horizontal tee section. As the quality is increased, more of the liquid is swept up the sides of the tube from the thick layer of liquid on bottom. This brings more liquid in contact with the branching port and a resultant improvement in separation characteristics. Similar results were reported by Henry [8] for annular flow in a horizontal tee section.

The investigations by St. Pierre and Glastonbury [6] included branch to inlet diameter ratios of 0.67 and 0.33. For identical inlet conditions they reported that separation was always more severe with the smaller diameter branch. They pointed out that the small branch diameter requires a higher radial acceleration of the flow for the same total flow fractions to be removed. This enhances air take off relative to water. Similar results are reported by Azzopardi and Freeman-Bell [11] for vertical annular flow in a tee junction.

In general the effect of inlet mass flux was found to be less significant than that of flow regime or quality. In their analysis of separation phenomena in a vertical tee section, Honan and Lahey [9] found no inlet mass flux dependence for the range of data tested. Some results for the three values of mass flux used were represented by a single line.

The previous discussions have considered the inlet section to be orientated in either a horizontal or vertical position. The most significant effect of these geometries is seen to result from their influence on the inlet flow regime. No studies have been carried out for other than these two inlet orientations.

The take off angle between the inlet and branch section in vertical upflow was considered by Honan and Lahey [9]. Angles of 45°, 90° and 135° were studied. Their results indicated that phase separation has essentially no dependence on take off angle for the range of data used. The authors concluded that this implies the momentum of the flowing mixture does not appreciably affect the separation process.

Whalley and Azzopardi [12] performed experiments on a horizontal inlet section for annular flow where the branch was inclined at various angles to the vertical. For identical portions of the inlet air flow removed the water take off rate was seen to increase as the branch inclination from the vertical was increased. This is expected due to the corresponding increase in local film thickness.

2.2.3 Phase Separation Modelling

Henry [8] investigated the separation phenomena using annular air-water flow in a horizontal 100 mm diameter test section with a 20 mm diameter horizontal branch. For less than 6 percent of the total flow removed through the branch, the branch liquid flow rate was seen to vary approximately linearily with the branch gas flow rate. This observation formed the basis for an empirical correlation of the form:

$$x_3 = \frac{1}{S+1}\left(1 - \frac{G_i}{G_3}\right) \tag{2.3}$$

where S is the slope of the linear relationship betwen the branch liquid and gas flow rates. The parameter G_i can be interpreted as the branch liquid mass flux when the branch gas flow rate is reduced to zero. This value was determined from the experiment by extrapolation. For inlet qualities greater than 0.05, both parameters were assumed to be functions of the inlet mass flux and quality and were best represented by an empirical fit of the form:

$$S\left(\frac{x_1}{1-x_1}\right) = 8.1 \times 10^{-7} G_{g1}^3 \tag{2.4}$$

and

$$G_i\left(\frac{x_1}{1-x_1}\right) = 0.00007\,(G_{g1} - 10)^3 \tag{2.5}$$

where G_{g1} is the inlet gas mass flux [kg/m^{2}s]. Agreement between the model and experimental values was best for higher inlet qualities.

Azzopardi and Whalley [7] investigated the separation phenomena for annular air-water flow in a 32 mm diameter vertical tee section with horizontal branches. Branch to inlet diameter ratios of 0.2, 0.4 and 0.6 where used. By passing measured amounts of air and water through the inlet tube with a porous section of wall, the liquid film was drawn off while entrained droplets passed through without being diverted. In this way the film flow rate for each inlet flow condition was determined. For phase separation experiments, the porous section was replaced by a tee junction.

The data was analyzed by defining θ (the apparent angle over which the film flow is extracted) as

$$\theta = \frac{360 \times \text{branch water flowrate}}{\text{total water film flow rate}} \tag{2.6}$$

This parameter was plotted against the air mass flux in the branch and a straight line was fit through the data of the form:

$$\theta = A + B G_{g3} \tag{2.7}$$

where G_{g3} is the branch air mass flux. The parameter A is similar to G_i in Henry's [8] model and can be interpreted as the limiting angle over which the film flow is extracted as the gas extraction rate is reduced to zero. The experimental value of A, determined by extrapolation, was compared with the actual angle subtended by the branching port and the centre of the inlet tube. Better results were obtained when compared with the angle subtended by a square port of equal area. No attempt was made to relate B to any hydraulic or geometrical parameters.

As a first approximation it was assumed that the gas and liquid extracted through the branch comes from the segment of the inlet tube defined by θ. The portion of gas extracted (P_g) is then related to θ by:

$$P_g = \frac{1}{2\pi}(\theta - \sin\theta) \tag{2.8}$$

Azzopardi and Freeman-Bell [11] extended this work to include diameter ratios of 0.8 and 1.0. They noted that the effect of branch diameter was best represented by

$$\frac{\theta}{\theta'} = 1.2\left(\frac{d}{D}\right)^{0.4} \tag{2.9}$$

when the portion of gas removed (P_g) is given by

$$P_g = \frac{1}{2\pi}(\theta' - \sin\theta') \tag{2.10}$$

The authors reported that most of the data was predicted to within ±30% with results from higher inlet qualities deviating most significantly.

Saba and Lahey [10] identified eight parameters of interest in the separation phenomena. These are the inlet, run and branch mass fluxes (G_1, G_2, G_3 respectivly), the inlet, run and branch qualities (x_1, x_2, x_3 respectively), the pressure drop from the inlet through the branch ($\Delta P_{1\text{-}3}$) and the pressure change from the inlet through the run ($\Delta P_{1\text{-}2}$).

Assuming 3 of these parameters to be specified, five conservation equations are required to obtain a solution. The equations used are:

i) The mixture continuity equation

$$G_1 A_1 = G_2 A_2 + G_3 A_3 \tag{2.11}$$

ii) The vapour phase continuity equation

$$G_1 x_1 A_1 = G_2 x_2 A_2 + G_3 x_3 A_3 \tag{2.12}$$

iii) The linear momentum equation for the branch

$$\Delta P_{1-3} = P_1 - P_{1j} + (\Delta P_{1-3})_j + P_{3j} - P_3 \tag{2.13}$$

where $P_1 - P_{1j}$ is the frictional pressure drop along the inlet to the junction and P_{3j}-P_3 is the frictional pressure drop from the junction along the branch. The term $(\Delta P_{1\text{-}3})_j$ represents the branch pressure drop due to the tee section. Its value was determined experimentally by extrapolating the fully developed profiles in each leg to the junction and is equal to $P_{1j} - P_{3j}$.

iv) The mixture linear momentum equation for the run

$$(\Delta P_{1-2}) = P_1 - P_{1j} + (\Delta P_{1-2})_j + P_{2j} - P_2 \tag{2.14}$$

The terms in this equation are defined as for the branch.

v) The vapour phase linear momentum equation for the branch

$$-\alpha \frac{dP}{dz} = \alpha F_d + \alpha \rho_g u_g \frac{du_g}{dz} + \alpha F_w + g \rho_g \alpha \sin\gamma_{1-3} \tag{2.15}$$

where F_d and F_w are the volumetric interfacial and wall drag forces on the vapour at the junction. The branch inclination to the horizontal is represented by $\gamma_{1\text{-}3}$.

The terms in the momentum equations are determined from empirical relationships developed by Saba and Lahey [13] based on separation data from their experiments on a horizontal tee section. Relationships developed previously by other investigators were also used. These equations were simplified based on the following assumptions:

- low inlet qualities ($\leq$ 1.0%)
- all legs of the tee section are horizontal
- high Reynolds number
- all legs of the tee have equal flow areas.

These assumptions were consistent with their experimental conditions. The resulting equations were solved for both homogeneous and slip flow conditions. The model predictions for homogeneous flow ($C_0 = 1.0$) are reported to best represent the measured data.

When the model predictions were compared with available higher inlet quality data, the best agreement was obtained for slip flow conditions ($C_0 = 1.2$). The equations were also solved for hypothetical steam-water conditions. The authors pointed out that the asymptotic behaviour of the model is correct in that the branch and inlet qualities are equal at the critical pressure.

2.2.4 Correlation of Pressure Distribution

The pressure effects of interest in the division of a flow stream at a tee junction are the axial pressure rise through the run of the tee and the radial pressure drop through the branch. For a tee junction in which the inlet and run have equal areas and the average fluid properties are assumed to define the flow field, a single phase axial momentum balance may be written

$$(\Delta P_{2-1})_j = P_{2j} - P_{1j} = k_{1-2}\,\rho\,(u_1^2 - u_2^2) = -(\Delta P_{1-2})_j \qquad (2.16)$$

where P_{1j}, P_{2j}, u_1 and u_2 are the pressures and velocities at stations 1 and 2 as shown in Figure 2.7. The coefficient k_{1-2} accounts for the axial momentum carried out of the control volume by the branching flow. When written as $(\Delta P_{2-1})_j$, an axial pressure rise is associated with a positive sign.

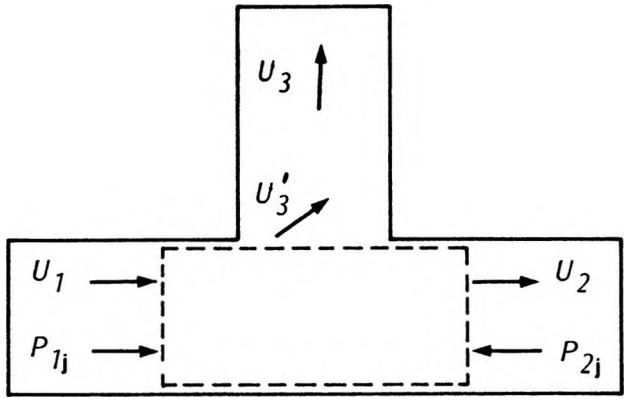

Figure 2.7 Control Volume For an Axial Momentum Balance at a Tee Junction

By considering a two-phase flow to be a homogeneous mixture in which the two phases have equal velocities, the mixture values of density and velocity may be written

$$\rho_h = \frac{\rho_g \rho_\ell}{x\,\rho_\ell + (1 - x)\,\rho_g} \tag{2.17}$$

and

$$u_h = \frac{G}{\rho_h} \tag{2.18}$$

respectively, where G is the total mass flux. Substituting equations (2.17) and (2.18) into (2.16) yields a homogeneous model for the run pressure rise, i.e.

$$(\Delta P_{2-1})_j = k_{(1-2)h}[(\rho_h u_h^2)_1 - (\rho_h u_h^2)_2] \tag{2.19}$$

where $k_{(1-2)h}$ is the homogeneous momentum correction factor.

By considering the flow of each phase separately through surfaces 1 and 2 and introducing $k_{(1-2)s}$, the separated flow momentum correction factor, equation (2.16) becomes.

$$(\Delta P_{2-1})_j = k_{(1-2)s}\left[\left(\frac{G_1^2 x_1^2}{\rho_g \alpha_1} + \frac{G_1^2(1-x_1)^2}{\rho_\ell(1-\alpha_1)}\right) - \left(\frac{G_2^2 x_2^2}{\rho_g \alpha_2} + \frac{G_2^2(1-x_2)^2}{\rho_\ell(1-\alpha_2)}\right)\right] \tag{2.20}$$

Fouda [14] and Fouda and Rhodes [15] investigated air-water annular flow in a 50.8 mm diameter inlet tube with a 25.4 mm vertical branch. The data obtained was analysed based on equations (2.19) and (2.20). The authors suggested that the separated flow model be used for simple tee junctions with a momentum correction factor of 0.533.

St. Piere and Glastonbury [6] used the separated flow model to determine $k_{(1-2)s}$ for various flow splits through the branch. The results for annular flow upstream of the junction were reported to be in good agreement with single phase air values. When the inlet flow was wavy, slug or stratified agreement was poor.

Fouda and Rhodes [15] modelled the radial pressure drop through the branch in three ways. Treating the branching port as an orifice and assuming a homogeneous mixture the orifice equation yields

$$\dot{m}_3 = C_{th} A_3 [2 \rho_{h3} (\Delta P_{1-3})_j]^{1/2} \tag{2.21}$$

where C_{th} is the two-phase homogeneous discharge coefficient. The phases were also assumed to flow through the branch without mutual interaction and the orifice equation was applied to each phase separately. Since the pressure drop is identical for each phase the orifice equation becomes

$$\dot{m}_3(1-x_3) = C_{t\ell}(1-\alpha_3) A_3 [2 \rho_\ell (\Delta P_{1-3})_j]^{1/2} \tag{2.22}$$

and

$$\dot{m}_3 x_3 = C_{tg} \alpha_3 A_3 [2 \rho_g (\Delta P_{1-3})_j]^{1/2} \tag{2.23}$$

for the liquid and gas phases respectively.

A separated flow model similar to that developed for the run was also used in the form

$$(\Delta P_{1-3})_j = k_{(1-3)s} \frac{G_3^2}{2} \left[\frac{x_3^2}{\rho_g \alpha_3} + \frac{(1-x_3)^2}{\rho_\ell (1-\alpha_3)} \right] \tag{2.24}$$

The data presented suggested that the homogeneous orifice model (eq. 2.21) best represented the experimental results with a homogeneous discharge coefficient (C_{th}) of 1.22.

St. Pierre and Glastonbury [6] reported that the pressure drop from the inlet through the branch, based on a homogeneous model, was essentially one branch velocity head for a branch to inlet diameter ratio of 0.67. For a ratio of 0.33 the losses were 1.5 velocity heads.

Saba and Lahey [10] split the branch pressure drop into a reversible and an irreversible component. The irreversible component was modelled as the product of the single phase water loss and a two phase multiplier (Φ), i.e.

$$(\Delta P_{1-3})_{j(irrev)} = \frac{k_{1-3}}{2} \frac{G_1^2}{\rho_\ell} \Phi \tag{2.25}$$

where k_{1-3} is the single phase loss coefficient. The reversible pressure change is modelled from the two-phase Bernoulli equation in the form

$$(\Delta P_{1-3})_{j(rev)} = \frac{\rho_{h3}}{2} \left[\frac{G_3^2}{(\rho_3''')^2} - \frac{G_1^2}{(\rho_1''')^2} \right] \tag{2.26}$$

where the energy weighted density (ρ''') is given by

$$\frac{1}{(\rho''')^2} = \left[\frac{(1-x)^3}{\rho_\ell^2 (1-\alpha)^2} + \frac{x^3}{\rho_g^2 \alpha^2} \right] \tag{2.27}$$

A homogeneous model was obtained by replacing the energy weighted densities in equation 2.26 with the appropriate homogeneous density. The authors reported good agreement between experimentally measured values and the homogeneous model.

CHAPTER 3

EXPERIMENTAL ARRANGEMENTS

3.1 Experimental Facility

3.1.1 Steam-Water Loop

The steam-water loop assembled at McMaster University is shown schematically in Figure 3.1. The system consists of a two horsepower Moyno Progressive Cavity Pump (Model 1L4, SSF ACC) capable of delivering water at a rate of 0.6 l/s at a differential pressure of 4.8 bar. Water is supplied to the pump from a 450 l hot water storage tank. The inlet water flow is controlled by way of valves located in the main water line and loop bypass. From the pump the water flows to a 6 kilowatt Chromalox circulation heater. To protect the equipment and measuring instruments from impurities in the water it is then passed through a filter (GAF, Model RBXAS-HD) capable of removing particles to 10 μm diameter. From the filter the water flows through a check valve to the two phase mixer.

Steam is taken from the main supply at approximately 6.9 bar (100 psi) and passed through a filter identical to that for the inlet water. This section of the steam line is also equipped with an inverted bucket steam trap (Spirax Sarco, Model 1/2 NPT-BIX125) to collect any condensate that may be present. The steam pressure is then reduced to the desired pressure through a Spence, Type EC, 1/2 inch pressure regulator. The steam flow rate is measured by an orifice plate assembly as described in section 3.2.2. From the orifice meter the flow passes through a check valve and a flow control valve to the two phase mixer where it is combined with the inlet water.

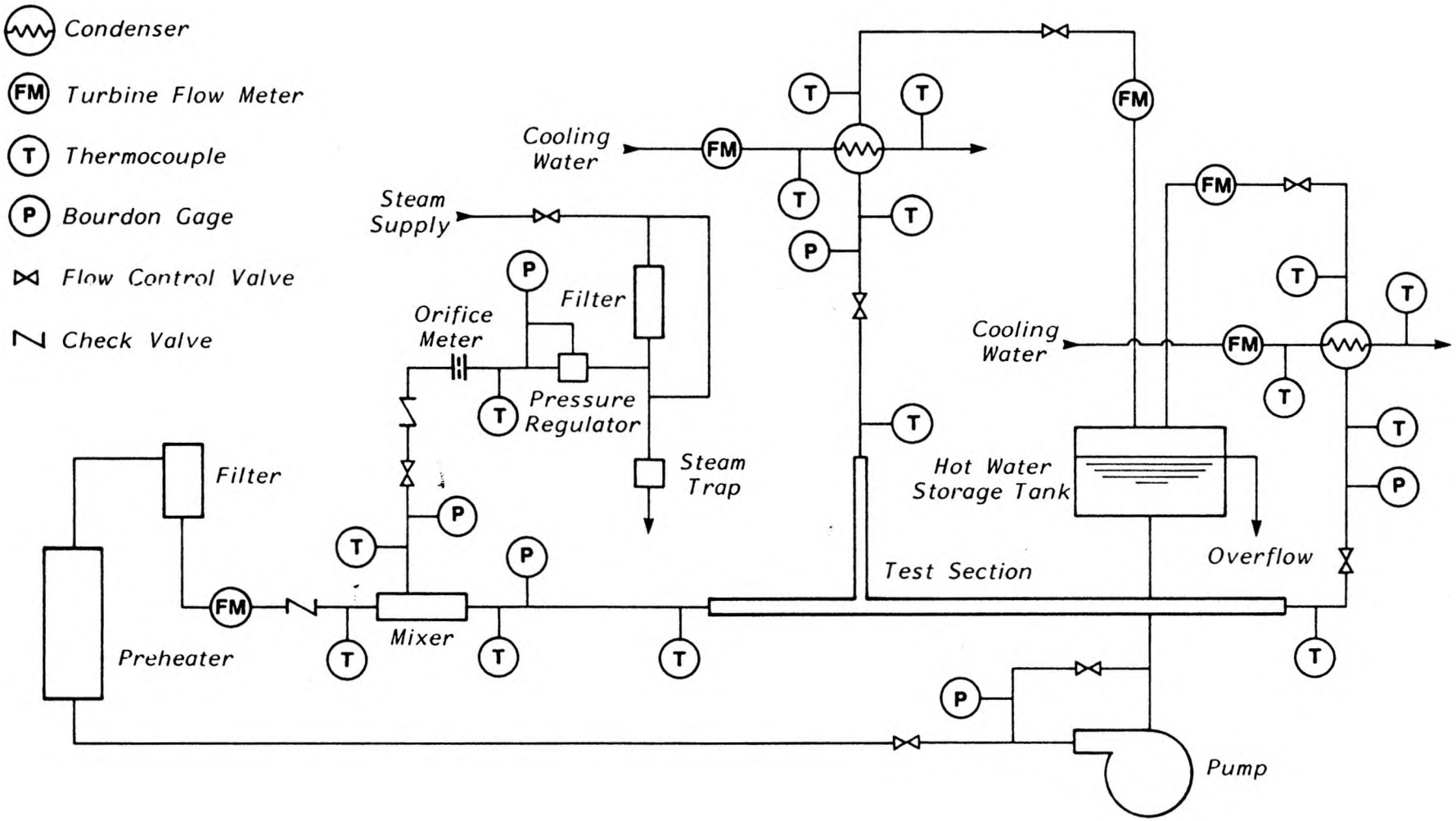

Figure 3.1 Schematic Diagram of the Steam-Water Loop

The steam and water are well mixed within the two phase mixer. From the mixer the flow becomes fully developed and reaches thermodynamic equilibrium through a 3.6 m long section of 1 inch sch. 40 stainless steel pipe before reaching the test section.

The test section used in the experiments presented herein was a horizontal tee test section, in which all legs were in the horizontal plane. The tee was made up of a 25.65 mm I.D. inlet with a 25.65 mm I.D. branch. The test section is described in detail in section 3.1.2. At the junction the flow is split into two streams; one in the axial direction through the run of the tee, the other in the radial direction through the branch. At the outlet from each leg the steam water mixture enters a 50 kilowatt, multipass, shell and tube condenser (American Standard P/N 5-030-05-014-004) exiting as single phase water. Cooling water is supplied from the mains at approximately 6-10 degrees Celsius. There are two flow control valves located in each branch of the tee, one upstream and one downstream of the condensers. The condensate from each branch is then directed back to the storage tank. The water level in the tank is kept constant by means of an open outflow.

The entire loop and tank are insulated with Micro Lok Fiberglass pipe or blanket insulation. An overall view of the experimental facility is shown in Figure 3.2. The measurement systems at the test section are isolated in Figure 3.3.

3.1.2 Two Phase Mixer

The mixer design, shown schematically in Figure 3.4, is similar to that used by Hasan [16]. The mixer is approximately 0.44 m long and is made up of two concentric stainless steel tubes and a reducing section. The inner and outer tubes are 2 inch sch. 40 and 1 inch sch. 40 stainless steel pipes respectively. At the upstream end of the mixer the inner tube protrudes through an end cap to connect with the inlet water supply. The outer tube is fitted with two 1 inch nipples on opposite sides connecting to the inlet steam supply. The

Figure 3.2 Overall View of the Experimental Facility

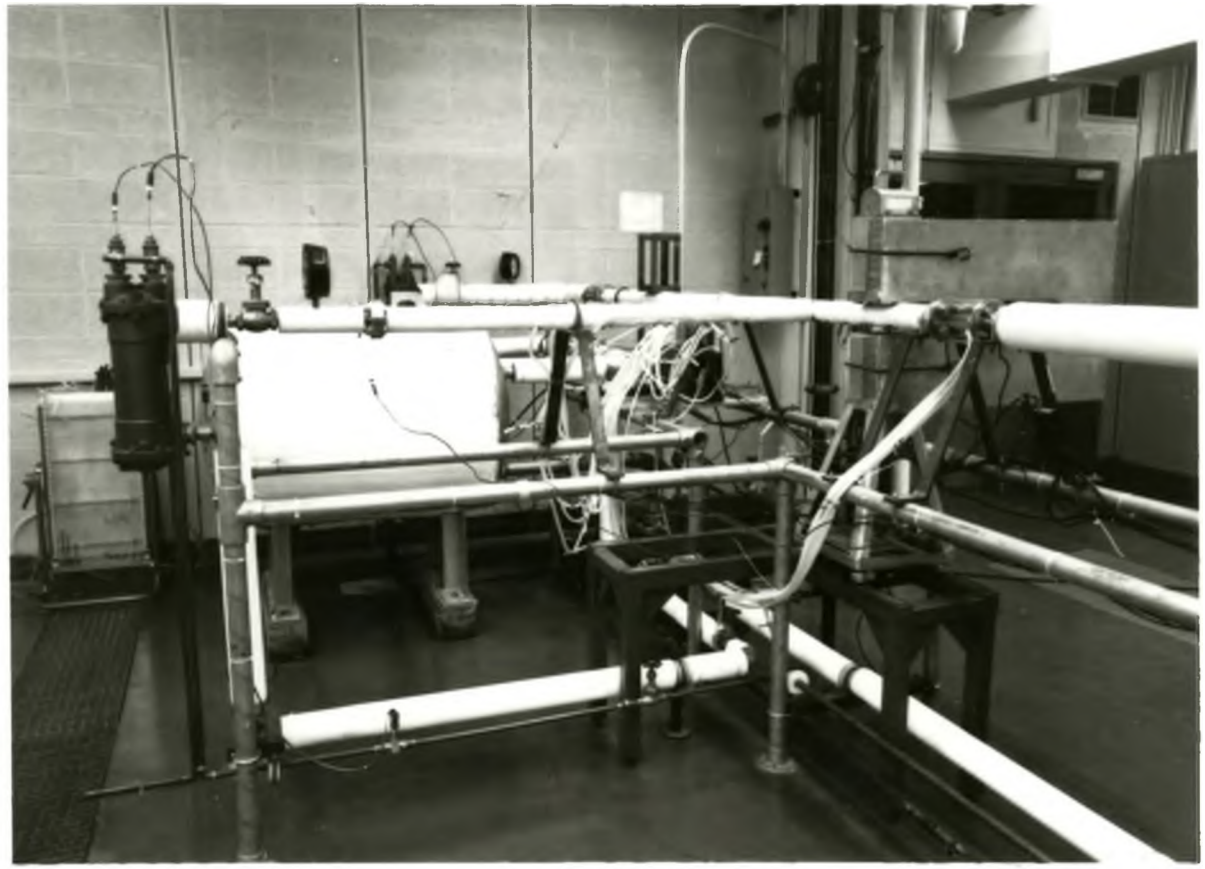

Figure 3.3 Measurement Systems at the Test Section

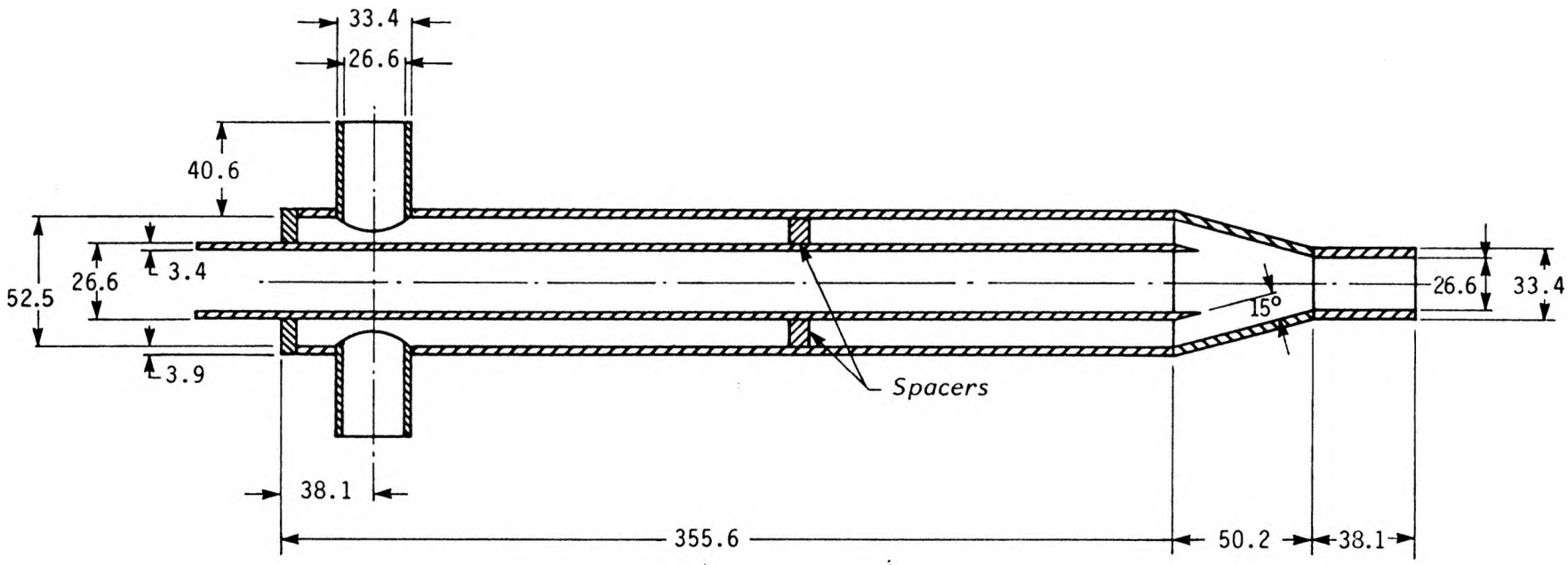

All Dimensions in mm

Figure 3.4 Two-Phase Mixer

reducing section is tapered at 15° to the axis and welded to the downstream end of the outer tube. The flow exits from the mixer through a 1 inch stainless steel nipple.

3.1.3 Test Section

The test section used for these experiments is detailed in Figure 3.5a. It consisted of a horizontal tube with one horizontal branch carefully machined and welded at 90° to ensure a sharp edged opening. The test section is constructed of 31.75 mm (1.25 inch) O.D. 25.65 mm (1.010 inch) I.D. stainless steel tubing. At the entrance to the test section a 0.15 m long section of transparent tubing (TPX) was used for indentification of the inlet flow regime.

The test section was originally constructed with all legs of equal length (610 mm) and with 5 pressure taps in each located symmetrically about the junction. At each tap location a 1/16 inch hole was drilled through the tube wall and countersunk to accept a 1/4 inch stainless steel tube. Short pieces of tubing were then bent and silver soldered into place for connecting the taps to the pressure measurement system (see Figure 3.5b). Special care was taken in drilling and polishing the taps to ensure no burrs protruded into the flow area. All taps were located at the bottom of the test section to inhibit steam from entering the pressure lines. The end of each leg was flanged so that subsequent test sections may easily be installed in the loop. The test section is shown in Figure 3.6.

Initial tests indicated that under some conditions the flow in the axial direction downstream of the junction (run) was not fully developed at the test section exit. For this reason the test section was extended in this direction to include an additional 10 pressure taps. The overall length of the run then became 2339 mm.

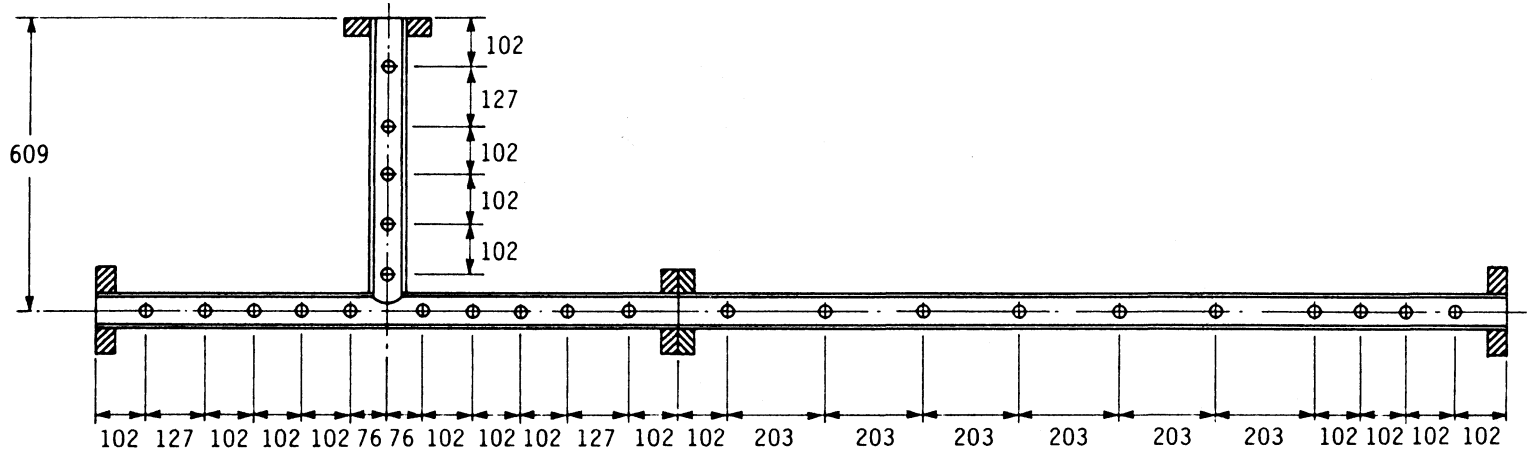

a) Tap Locations

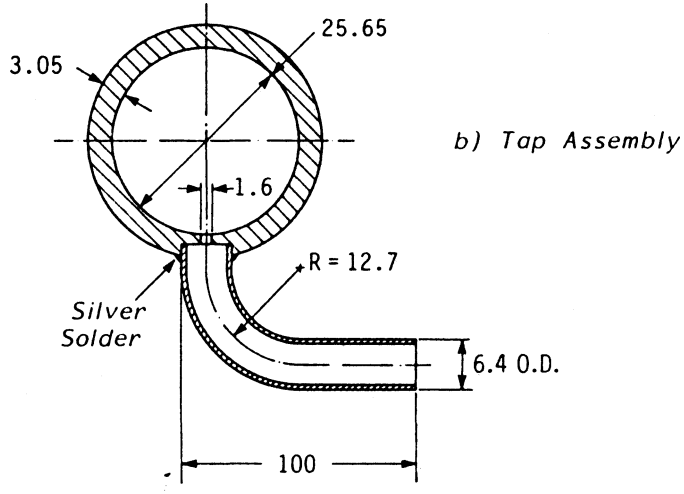

b) Tap Assembly

All Dimensions in mm

Figure 3.5 Schematic Diagram of the Test Section

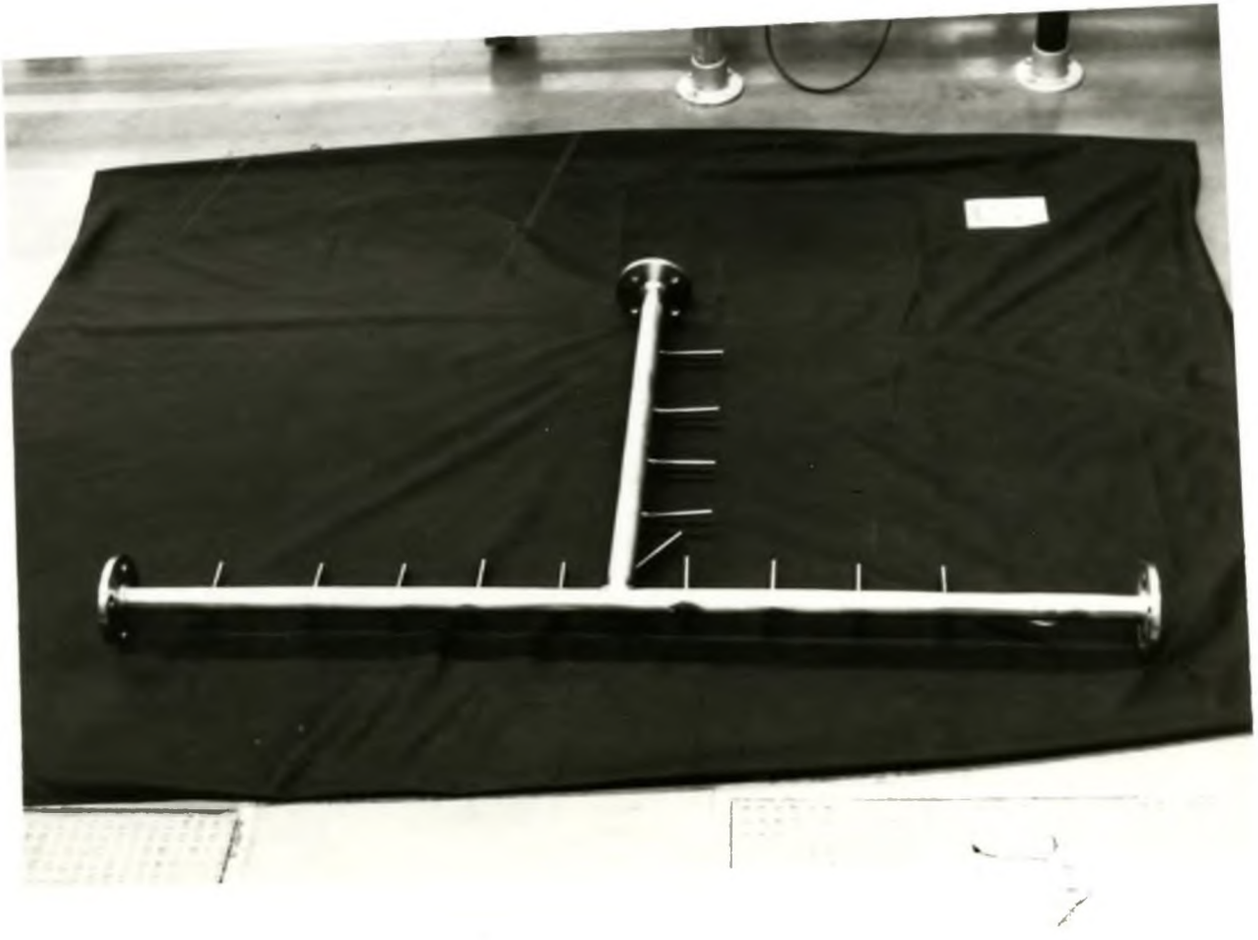

Figure 3.6 Test Section

3.2 Measurement and Calibration

3.2.1 Water Flow Rate Measurements

Water flow rates were measured with turbine flow meters at five locations throughout the loop as listed below (see Figure 3.1).

Location	Model	Range
Mixer Inlet	ITT Barton, No. 8086	0.15-1.8 l/s
Run Condenser Exit	ITT Barton, No. 8086	0.15-1.8 l/s
Branch Condenser Exit	Flow Technology, FT-8N10-LJC	0.06-0.6 l/s
Run Cooling Water	Flow Technology, FT-8N10-LJC	0.06-0.6 l/s
Branch Cooling Water	Flow Technology, FT-8N10-LJC	0.06-0.6 l/s

All meters used were calibrated by the manufacturers. The higher range meters (ITT Barton, No. 8086) operate accurately to within $\pm 1\%$ of reading over the entire flow range. The lower range meters are accurate to $\pm 0.5\%$ of reading over the measurement range. All meters are equipped with magnetic pickup coils and the output signals are directed to frequency channels in the data acquisition system.

3.2.2 Steam Flow Rate Measurements

Steam flow rates were measured using an orifice plate assembly. The system consists of an orifice plate (19 mm bore diameter) installed in the 1 inch nominal sch. 40 steam line downstream of the pressure regulator. The plate is held in place with a 300 lb orifice flange union. Both plate and union were supplied by Cantrols Equipment Ltd.

To ensure that the pressure lines to the transducer remain vapour free the assembly was equipped with two condensing chambers mounted above the orifice meter as

shown in Figure 3.7. The condensing chambers were fabricated in the departmental machine shop from 225 mm sections of 2 inch sch. 40 stainless steel pipe. Each was fitted with plain blanks on both ends and three 3/4 inch bosses around the centre of the pipe. The upper bosses were connected to ball valves allowing the chambers to be vented. Those located at 45° from vertical were fitted with 1/4 inch tubing connecting to the upstream or down stream flange taps. These tubes protruded through the wall to the centre of the chamber. The bosses located on the bottom were fitted with 1/4 inch tubing passing through the wall to approximately 1/4 of the chamber height. These tubes extended downward and were connected through an equalizing valve and the signals were delivered to the appropriate side of a differential pressure transducer (Validyne, Model DP15-36) of the range 0-35 kPa. The transducer is excited at 5 volts, 5 kHz by a carrier demodulator (Model CDC 101). This unit demodulates the transducer output providing a ± 10 volt DC signal which is delivered to the data acquisition system.

The orifice meter was calibrated on line for two upstream pressures (200 and 275 kPa) by direct weighing of condensate. Transducer and meter calibration details are contained in Appendix A.

3.2.3 Temperature Measurements

Temperature measurements were made using standard E type thermocouples at 15 locations throughout the loop as listed below (see Figure 3.1).

- steam inlet to the two phase mixer
- water inlet to the two phase mixer
- two phase mixer exit
- test section inlet
- test section exit (run)

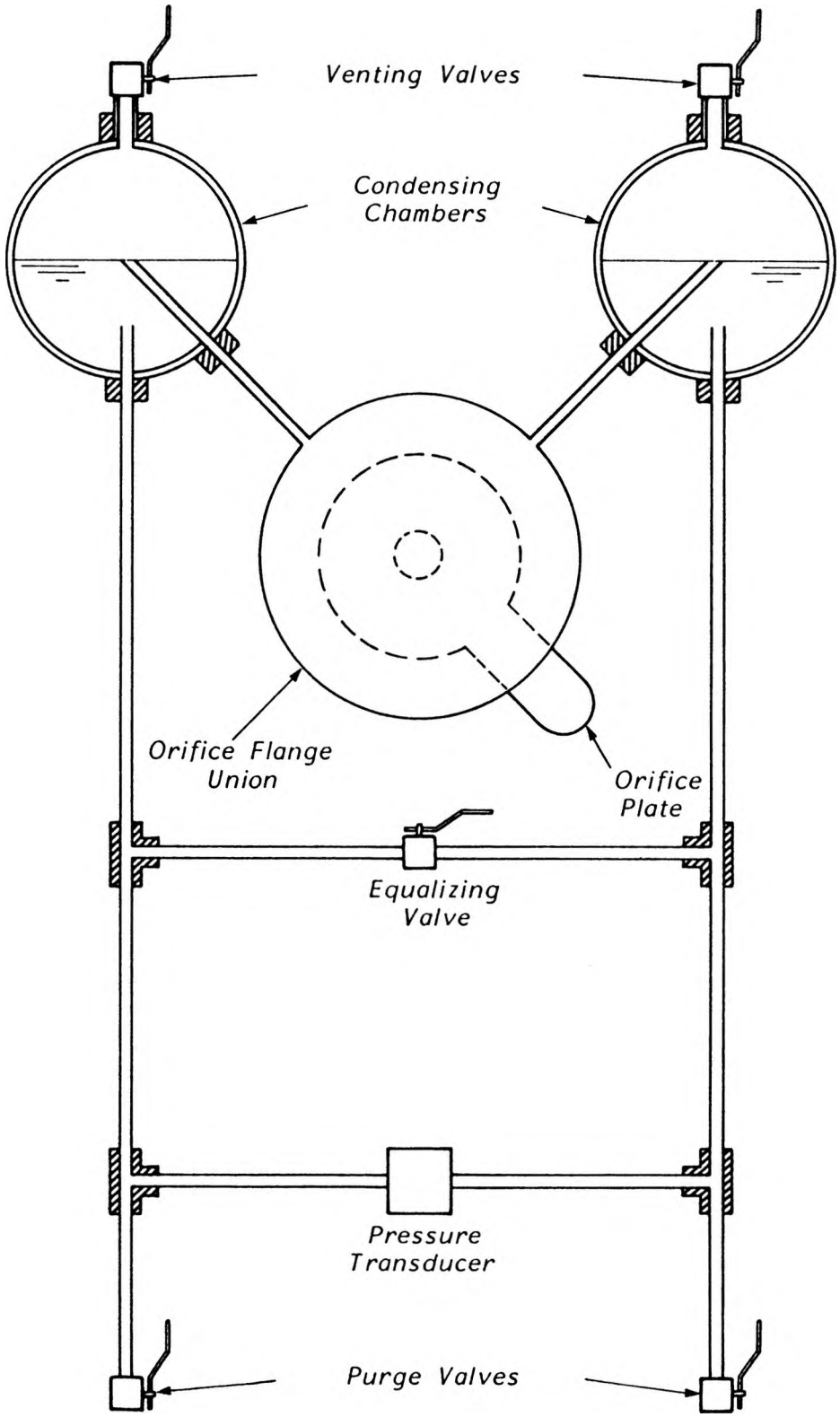

Figure 3.7 Orifice Meter Assembly

- run condenser inlet
- run condenser exit
- test section exit (branch)
- branch condenser inlet
- branch condenser exit
- cooling water inlet (run)
- cooling water exit (run)
- cooling water inlet (branch)
- cooling water exit (branch)
- steam line upstream of orifice

All measurements were referenced to 0°C through an ice/water bath. The analog signals from each thermocouple were delivered directly to the data acquisition system.

3.2.4 Pressure Distribution Measurements

A schematic diagram of the pressure measurement system is shown in Figure 3.8. The first upstream pressure tap in the inlet section (tap #1) was used as a reference. Its signal was split with one branch connected to the high side of a differential pressure transducer (Validyne, Model DP 15-46, 0-350 kPa) for measuring system pressure. The low side of this transducer was open to atmosphere. The other branch was connected to the high side of a bank of two differential pressure transducers, one high range and one low range, used for measuring the pressure differences between station #1 and subsequent stations. The signals from all other pressure taps may be delivered individually to the low side of the transducer bank through a 24 channel switching valve (Scanivalve Model WO2). These signals can be directed to the high or low range transducer through a series of valves as shown.

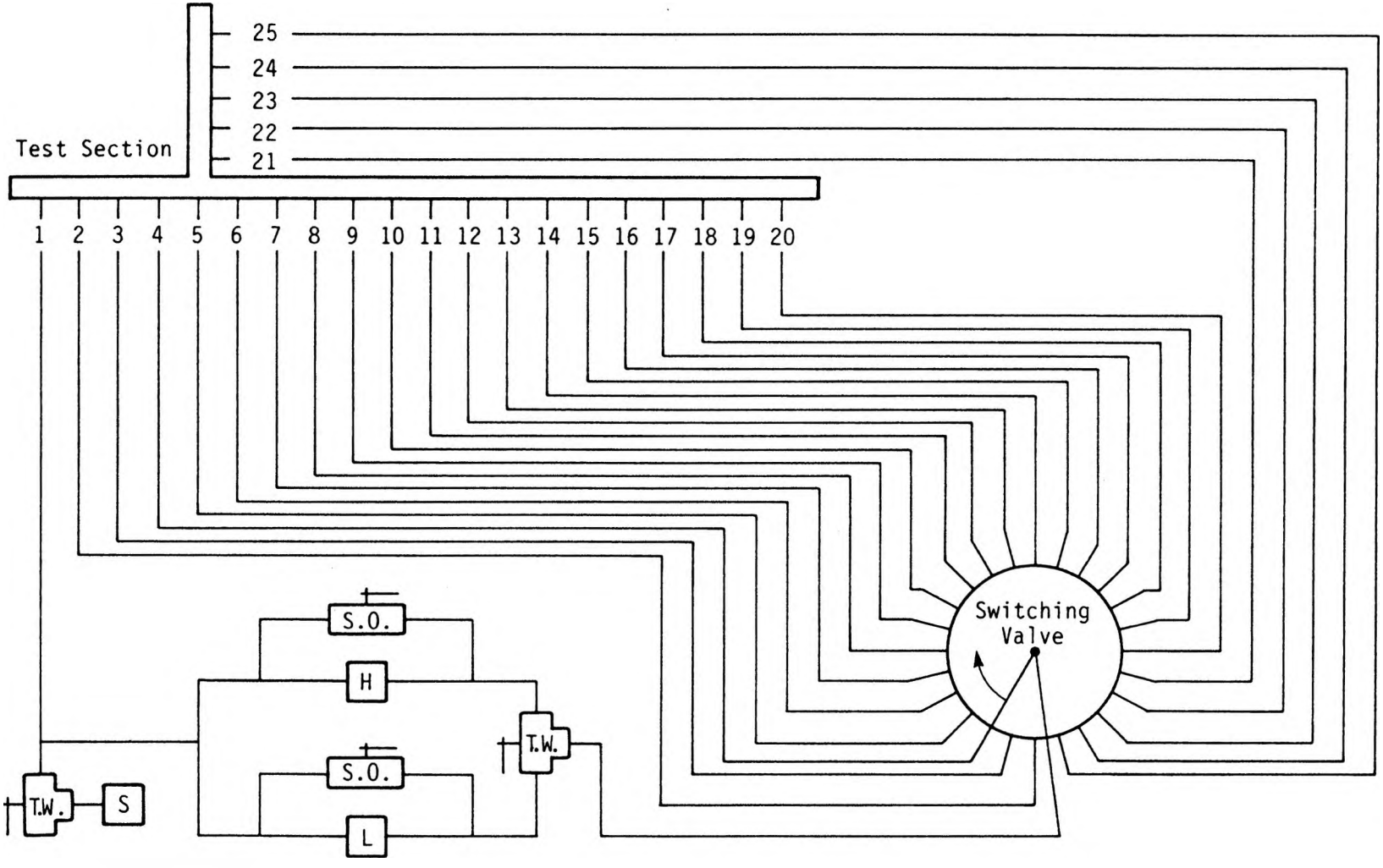

Figure 3.8 Schematic Diagram of Pressure Measurement System

Pressure lines from the taps to the transducer bank were made of transparent Tygon tubing. After installation all lines were thoroughly purged to ensure no air remained in the system. The transparent tubing allowed a visual check for air or steam that may have become trapped in the lines.

For all experimental runs the high range transducer used was a Validyne Model DP15-38 of the range 0-55 kPa. For single and two phase runs, the low range transducers used were Validyne Model DP103-20 (0 - 0.55 kPa) and Validyne Model DP103-28 (0 - 5.5 kPa) respectively. The transducers are excited at 5 volts, 5 kHz by carrier demodulators identical to that for the orifice meter transducer (see Section 3.2.2).

Calibration details for each transducer are contained in Appendix A.

3.2.5 Void Fraction Measurements

Void fraction measurements were made at various locations throughout the test section with a traversing single beam gamma densitometer. The system consisted of a 75 mCi cobalt 57 sealed source contained in a stainless steel casket and located above the test section. The gamma beam was defined by two sets of 12 collimating plates ($127 \times 127 \times 19.1$ mm plates, 50.3×12.7 mm aperture) one above and one below the test section. The signal was received by a 76.2 mm cubic NaI(Tl) scintillator and standard signal processing equipment (see Figure 3.9). The processed signal was delivered to two cascaded counters within the data acquisition system. The source, collimating plates and scintillator were housed in a carriage capable of scanning the test section on a traversing table as shown in Figure 3.10.

Void fraction measurements were made at 17 stations throughout the test section as shown in Figure 3.11. Measurements at stations 1 through 11 and 13 through 17 were made with the traversing system. It was experimentally observed that certain flow

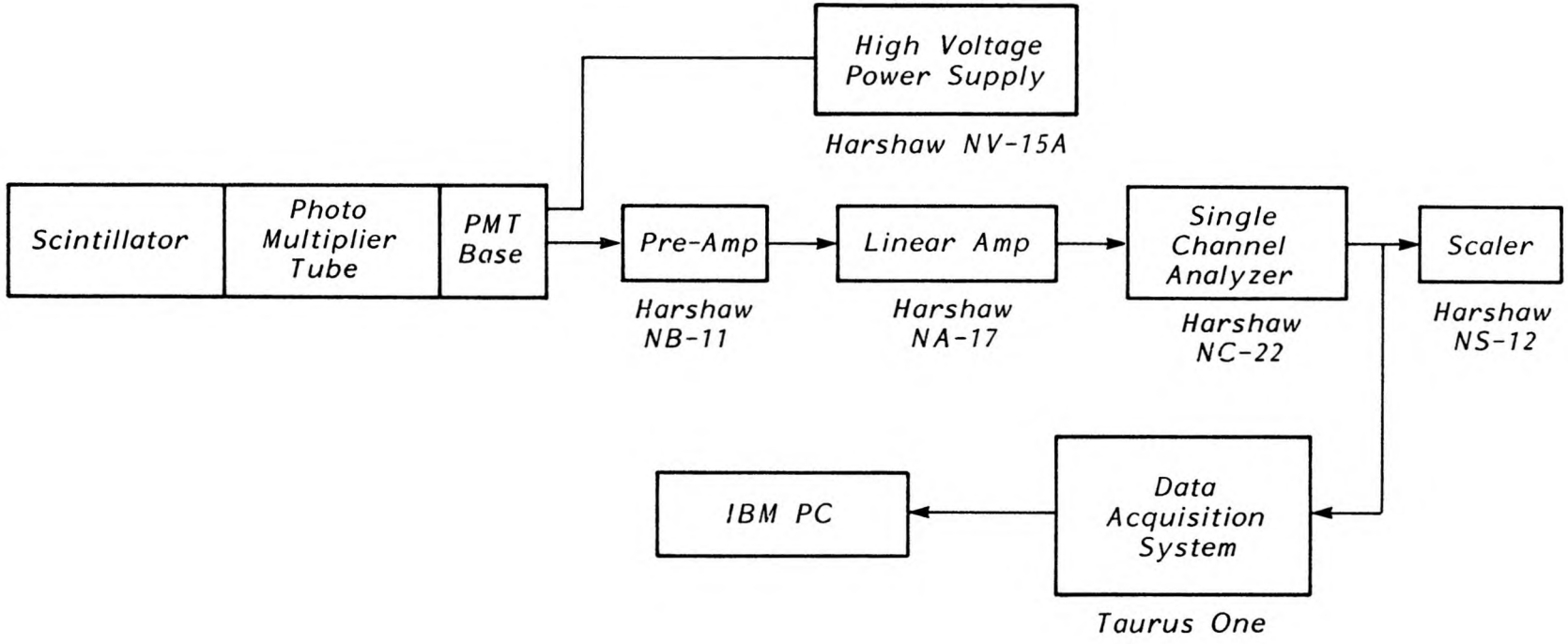

Figure 3.9 Signal Processing System for Void Fraction Measurements

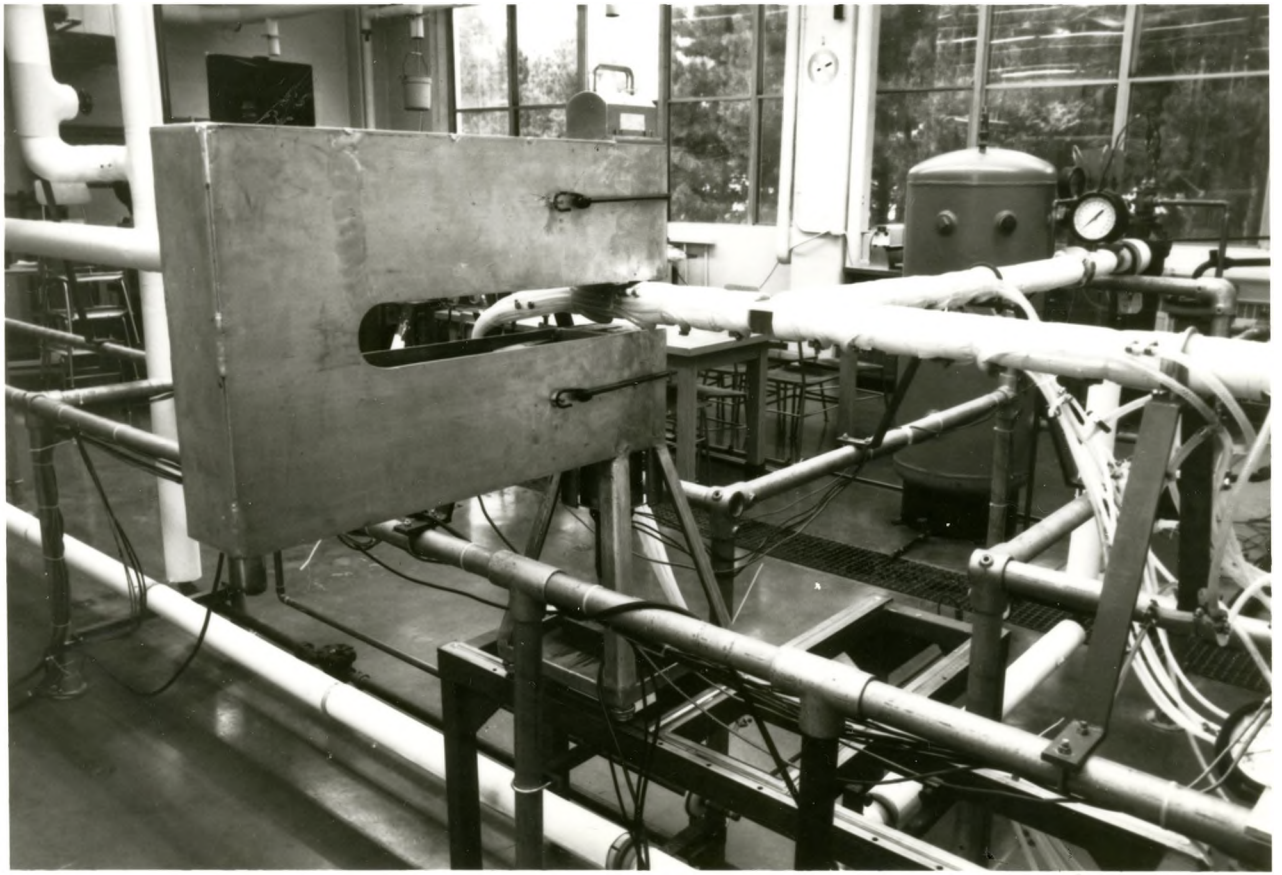

Figure 3.10 Void Fraction Measurement System

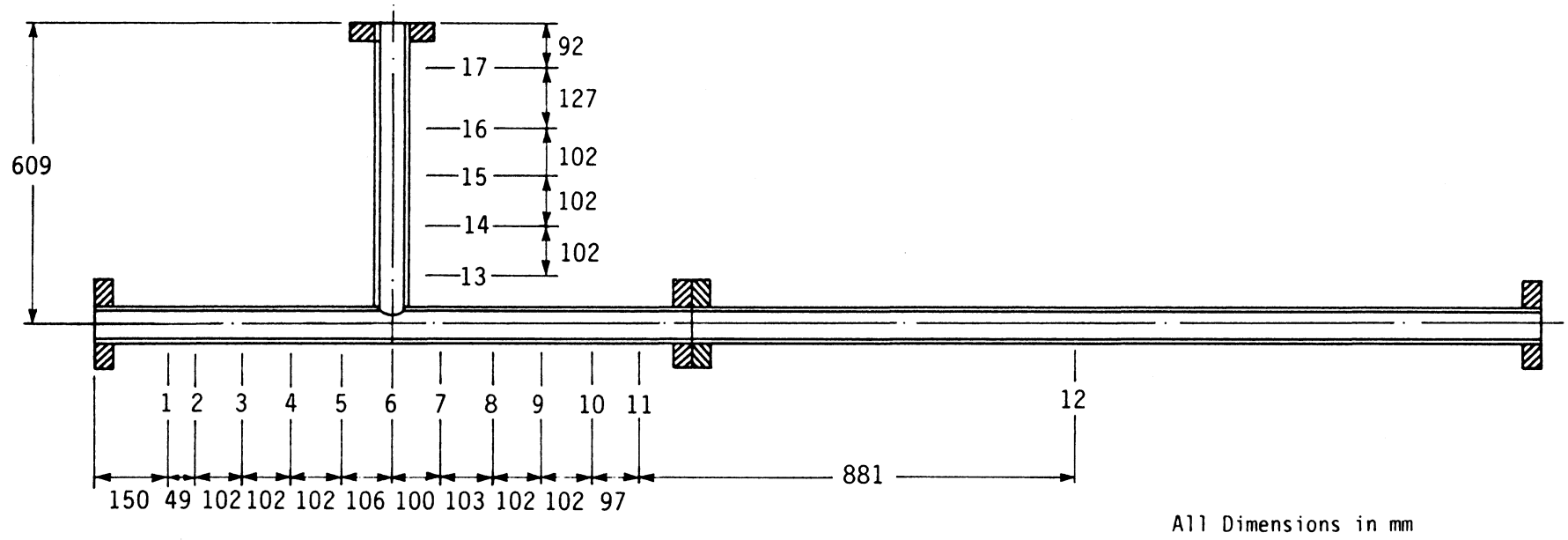

Figure 3.11 Void Fraction Measurement Stations

conditions did not yield fully developed void fraction profiles at the run exit. For this reason a single fixed densitometer stand was added at station 12 far downstream from the junction.

The system was calibrated daily by taking full and zero void counts at each station ($N_{(\alpha=1)i}$ and $N_{(\alpha=0)i}$ respectively, $i = 1-17$). The test void fraction (α_i) was determined from the test count ($N_{\alpha i}$) using the linear interpolation equation derived in Appendix B.

$$\alpha_i = \frac{N_{\alpha i} - N_{(\alpha=0)i}}{N_{(\alpha=1)i} - N_{(\alpha=0)i}} \tag{3.1}$$

Further design and calibration details are contained in Appendix B.

3.2.6 Data Acquisition System

All signals from the flow meters, thermocouples, pressure transducers and the gamma densitometer were directed to the Taurus One data acquisition system manufactured by Taurus Computer Products Inc. The Taurus One is a Z80A based microcomputer with its own firmware based operating system and an input/output bus for plugging in various I/O modules. The present system is equipped with two input/output modules (T-10470 and T-3732T) giving it 4 frequency channels, 3 event counters and 32 analog input channels. Since the number of frequency channels was one less than the number of flow meters, the two cooling water meters were connected to a single channel through a switch.

The system was hosted by an IBM PC equipped with 2 floppy disk drives and a 10 megabyte hard disk. The data acquisition system in shown in Figure 3.12.

3.2.7 Computational Procedure for Data Reduction

The data from all experimental runs was reduced to determine a total of 11 parameters. These are:

- the mass flow rate in each leg ($\dot{m}_1$, $\dot{m}_2$, and $\dot{m}_3$)

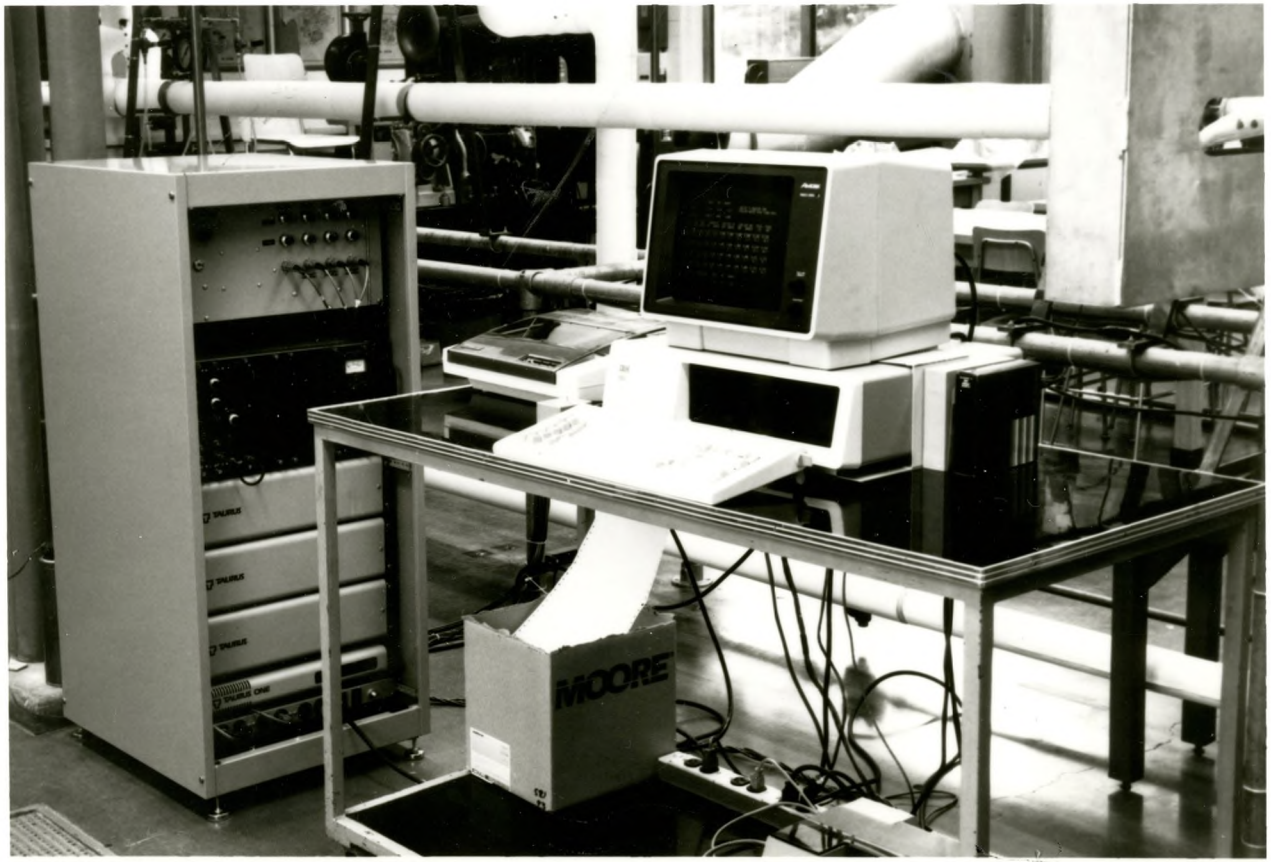

Figure 3.12 Data Acquisition System

- the flow quality in each leg (x_1, x_2, and x_3)
- the fully developed void fraction in each leg (α_1, α_2 and α_3)
- the run and branch junction pressure differentials ($\Delta P_{1\text{-}2}$ and $\Delta P_{1\text{-}3}$ respectively)

The mass flow rate at the test section inlet ($\dot{m}_1$) is the sum of the mixer flows of steam and water.

$$\dot{m}_1 = \dot{m}_{gm} + \dot{m}_{\ell m} \tag{3.2}$$

The mass flow rates in the run and branch ($\dot{m}_2$ amd $\dot{m}_3$) were determined directly from the appropriate turbine flow meter.

The inlet quality is the thermodynamic equilibrium quality based on the mixer conditions and the average test section temperature in the three legs

$$x_1 = \frac{\dot{m}_{gm} h_{gm} + \dot{m}_{\ell m} h_{\ell m} - \dot{m}_1 h_{\ell t}}{\dot{m}_1 (h_{gt} - h_{\ell t})} \tag{3.3}$$

In the run and branch of the tee, the flow qualities were determined from an energy balance at the appropriate condenser.

$$x_j = \frac{\dot{m}_j h_{cj} + [\dot{m}_{cw} (h_{cwo} - h_{cwi})]_j - \dot{m}_j h_{\ell t}}{\dot{m}_j (h_{gt} - h_{\ell t})} \qquad j=2,3 \tag{3.4}$$

The fully developed void fraction in each leg of the test section was determined directly from measurements. In general, these values were the furthest upstream measurement in the inlet section and the furthest downstream measurements in the run and branch of the tee.

The junction pressure differentials were determined by extrapolating the fully developed pressure profiles in each leg forward or back to the junction. The required differential was then the difference between the two extrapolated values as shown schematically in Figure 3.13.

Saturation values based on the measured temperature were used for all compressed liquid properties required for computation. The correlations used for these and the test

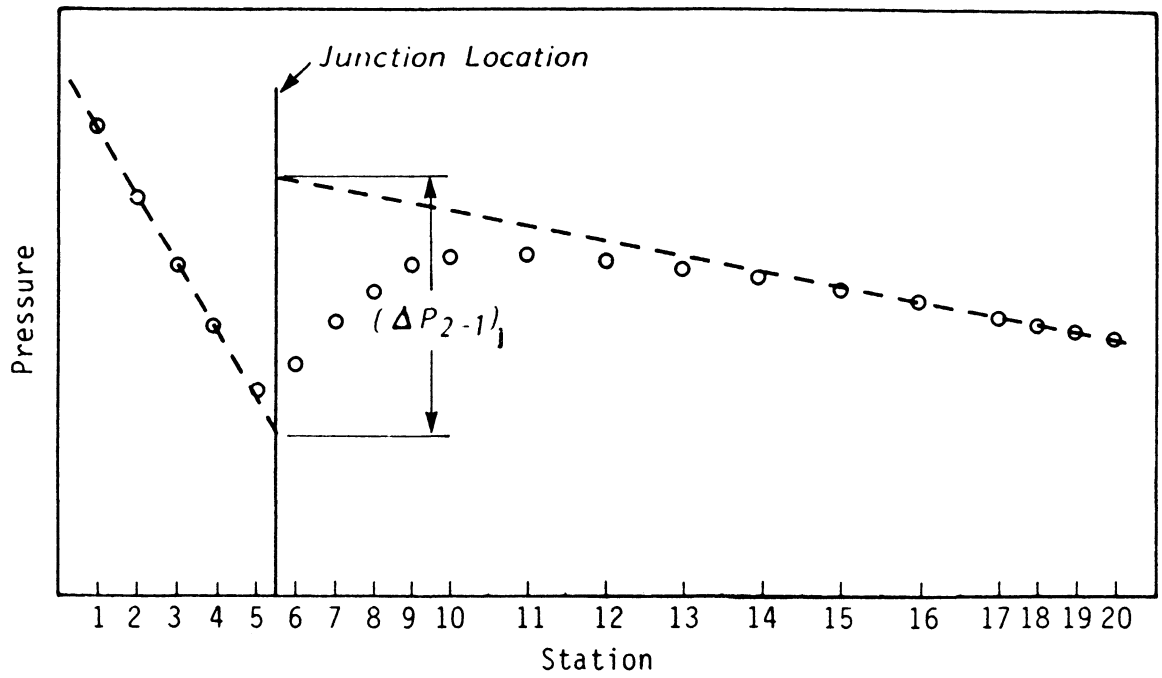

a) Run Pressure Differential $(\Delta P_{2-1})_j$

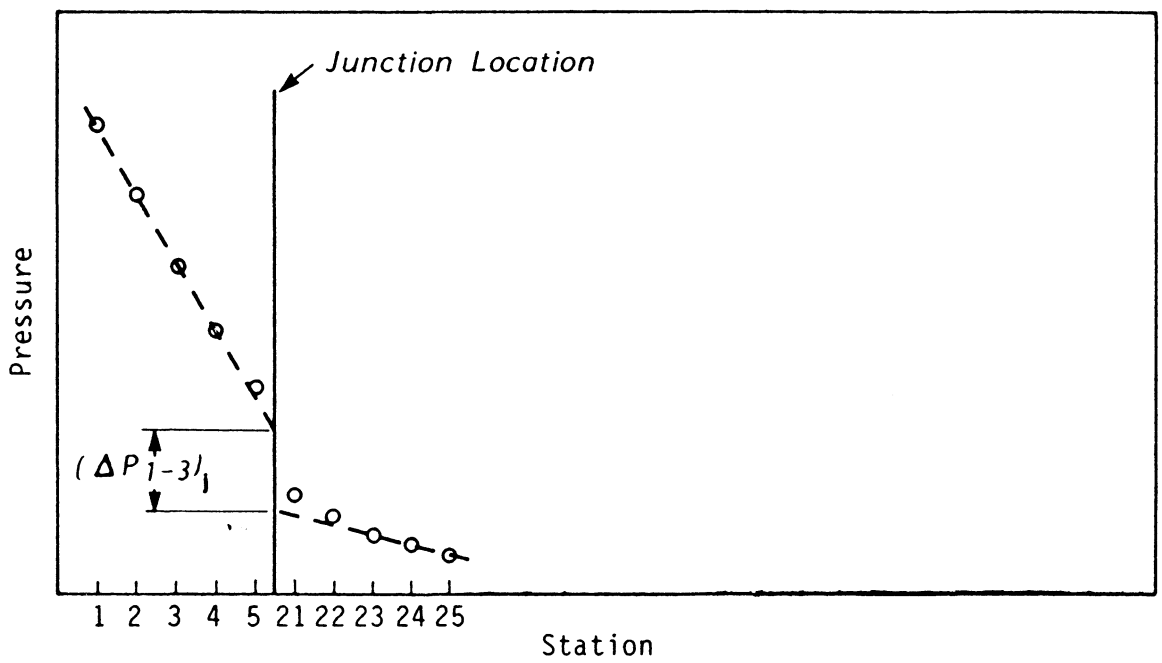

b) Branch Pressure Differential $(\Delta P_{1-3})_j$

Figure 3.13 Schematic Diagram of a Typical Pressure Distribution in Dividing Flow

section saturation conditions (from [17]) are shown in Appendix C. At the mixer inlet the steam was slightly superheated and the enthalpy was determined from steam tables.

3.3 System Operation

3.3.1 Start-up Procedure

Following is a description of the step by step procedure used to calibrate the gamma densitometer and prepare the loop for experimental measurements. This procedure was carried out at the beginning of each day.

1. Open all transducer equalizing valves and the condensing chamber exhaust valves. Check and correct for any transducer zero shift. Close the condensing chamber exhaust and orifice meter equalizing valves.
2. Open the loop bypass and main water line valves. Start the pump and open both flow control valves in each leg. Close the bypass valve and turn on the preheater.
3. Open both cooling water valves to about 50% full flow. Open the main steam supply valve, then slowly open the steam flow control valve to 100% full flow.
4. Monitor the loop temperature distribution and adjust the cooling water flow rates to maintain condensate temperatures of approximately 75°C.
5. When the inlet water temperature reaches 70°C, close the steam flow control valve and cooling water supplies.
6. At this point only water is flowing in the loop. Put the gamma source in place and unclamp the densitometer carriage from the traversing table. Take zero void counts at each void fraction measuring station for 30 seconds.

7. Open both cooling water valves to approximately 50% full flow and slowly open the steam flow control valve to 100% full flow.
8. Turn off the preheater, slowly open the loop bypass valve and close the main water supply valve removing the water from the loop.
9. Adjust cooling water flow rates to maintain condensate temperatures below 80°C. Allow the steam to flow through the test section for approximately 10 minutes to ensure no water remains.
10. Take full void counts at each void fraction measuring station for 30 seconds.
11. Open the main water line valve and slowly close the loop bypass valve to re-establish a two phase flow within the system.

3.3.2 Test Procedure

The independent flow parameters for each experimental run were the nominal values of inlet mass flux, inlet quality and flow split. These were set by adjusting the flowrates of water and steam to the mixer and the flow control valves in the run and branch of the tee. The flow conditions throughout the loop were monitored at the computer terminal while adjusting the flow valves. At this point all the conditions on the screen were those based on a single data sweep of the temperature and flow measurement systems. The process of attaining the desired flow conditions was iterative as small changes in any control valve had an effect on all flow parameters. Once the desired conditions were obtained, the system was allowed to run for approximately 30 minutes to ensure that a steady state was reached.

At steady state, data sweeps of the flow condition were taken and the average values were updated after each sweep. Once the fluctuations have been averaged out (15-20 sweeps) the final test conditions were determined. If these were acceptable, the inlet

flow regime was recorded and the pressure and void fraction distributions were obtained. If not, the flow was adjusted and the process was repeated.

Pressure measurements began by directing the pressure signal from station 1 to the high side of the system pressure transducer (S in Figure 3.8). The demodulator output signal was sampled for 30 seconds at a rate of 100 samples per second. These values were averaged to determine the gauge pressure at tap 1. The transducer bank valves were set such that the signal from the switching valve was directed to the high range transducer (H in Figure 3.8). The switching valve was then set to measure the pressure differential between taps 1 and 2. The signal from the high range transducer was sampled for 2 seconds at a rate of 100 samples per second. If the average reading was less than 4.5 kPa the operator was prompted to set the valves to deliver the signal to the low range transducer. The appropriate channel was now sampled for 30 seconds at a rate of 100 samples per second to measure the desired pressure drop.

Once the pressure drop was determined a sweep of the flow conditions was made and averaged with the preceding readings. The updated conditions were sent to the printer and displayed on the screen along with the previous 3 updates. If no significant or monotonic variation in conditions was noted that would nullify the test run, the operator proceeded to measure the pressure drop between taps 1 and 3. A similar procedure was followed for the rest of the pressure taps. At the end of the pressure measurements all transducer equalizing valves were set open.

Void fraction measurements were taken by locating the gamma densitometer traversing carriage at each measurement station in turn and recording a 30 second count. The void fraction at each station was computed as measured. Between each measurement, a sweep of the loop flow conditions was made as for the pressure measurements.

At the end of the void fraction measurements the data acquisition for the test run was complete.

3.3.3 Shut-down Procedure

Following is a step by step description of the procedure used to shut-down the loop at the end of each day.

1. Slowly close the steam flow control valve and main steam supply valve.
2. Turn off the preheater. Close both cooling water supply valves
3. Fully open the loop bypass valve and close the run and branch control valves on the condensate side. Turn off the pump.
4. Clamp the densitometer carriage in place. Return the source to the storage locker.

3.3.4 Test Conditions

Experiments were carried out with both single phase water and two-phase steam-water conditions. Single phase water tests were carried out at room temperature with 4 values of inlet mass flux. The flow split through the branch ($\dot{m}_3/\dot{m}_1$) was varied and the pressure distribution for each condition was measured. The single phase test conditions are shown in Table 3.1.

Two phase flow tests were carried out with the same nominal values of inlet mass flux. The inlet quality was varied from 2% to 15% and the inlet flow conditions were always annular. The flow splits for each run were case dependent to yield adequate distributions of phase separation and pressure data. The two phase flow test conditions (inlet mass flux and quality) are shown in Table 3.2. The experimental results for both single and two-phase experiments are shown in Appendix D.

TABLE 3.1: SINGLE PHASE TEST CONDITIONS

Flow Split (G_3/G_1)	Inlet Mass Flux (G_1) [kg/m^{2}s]			
	450	600	900	1200
.1	X	X	X	X
.3	X	X	X	X
.5	X	X	X	X
.7	X	X	X	X
.9	X	X	X	
1.0	X	X	X	

TABLE 3.2: TWO-PHASE TEST CONDITIONS

Inlet Quality (x_1) [%]	Inlet Mass Flux (G_1) [kg/m^{2}s]			
	450	600	900	1200
2		X	X	X
4.5	X	X	X	
8.0		X		
15	X			

CHAPTER 4

RESULTS AND DISCUSSION

4.1 Phase and Energy Balances

Of the 64 two-phase experimental runs presented herein, 44 had condensate flow rates that were within the linear range of both flow meters. For these runs, comparing the total condensate flows with the total mixer flows of steam and water showed that 95% of the data satisfied mass continuity to within ± 1.5%. For the remaining 20 runs, experimental conditions required one of the condensate flows to fall below the linear range of the meter. Based on the results of the continuity check it was considered reasonable to use a mass balance in these cases to determine the appropriate flow rate.

The rate at which energy is convected into the test section is determined from the mixer flows as

$$\dot{E}_{in} = \dot{m}_{gm} h_{gm} + \dot{m}_{\ell m} h_{\ell m} \tag{4.1}$$

The total flow rate of energy exiting the test section can be determined from the condensate and cooling water flows as

$$\dot{E}_{out} = \dot{m}_2 h_{c2} + [\dot{m}_{cw} (h_{cwo} - h_{cwi})]_2 + \dot{m}_3 h_{c3} + [\dot{m}_{cw} (h_{cwo} - h_{cwi})]_3 \tag{4.2}$$

Comparing these two values for all experimental runs showed that 95% of the data satisfied the energy balance within ± 1.5%.

The flow of each phase at the test section inlet was determined from the assumption of thermodynamic equilibrium (eqn. 3.3). The exiting flow of each phase was calculated from energy balances at the condensers (eqn. 3.4). When these values were compared for all runs, 95% of the data satisfied continuity to within ± 11.0% and ± 1.5% for steam and water flow respectively.

4.2 Phase Separation

The measured branch quality was corrected for deviations of the inlet quality from the nominal value by assuming that the same percentage of gas would be removed through the branch at that nominal value. The corrected branch quality (x_3') is then given by

$$x_3' = x_3 \frac{x_{1\,nom}}{x_1} \tag{4.3}$$

Throughout the thesis x_3 and x_1 will be used to refer to the corrected branch quality and the nominal inlet quality respectively. The complete as measured data for all experimental runs is tabulated in Appendix D.

Figures 4.1 through 4.8 show the corrected branch quality (x_3) plotted against the branch flow split ($\dot{m}_3/\dot{m}_1$) for fixed nominal values of inlet mass flux and quality. These figures show the severe maldistribution of phase which can occur in the downstream legs of the tee. The assumption of equal phase separation would have all points falling on the horizontal line at $x_3 = x_1$. Clearly, this assumption does not approximate the measured data in any region. At low branch flow splits, the branch quality increases very rapidly with increasing flow split crossing the equal phase separation line ($x_3 = x_1$)at close to 90°. If the data in this region were extrapolated back to the axis it appears that some limiting value of water flow could be established in the branch when the branch quality was reduced to zero. This supports the findings of Azzopardi et al. [7] and Henry [8] and suggests that the liquid is first removed from the low velocity film flowing at the tube walls near the branching port.

When the flow split is further increased, the branch quality peaks or levels off at splits in the range of 20 to 30%. As expected, the branch quality eventually decreases to the inlet quality when $\dot{m}_3 = \dot{m}_1$. In all cases, when the flow split reaches 30 to 40% the branch quality is closely approximated by the complete separation curve generated from the

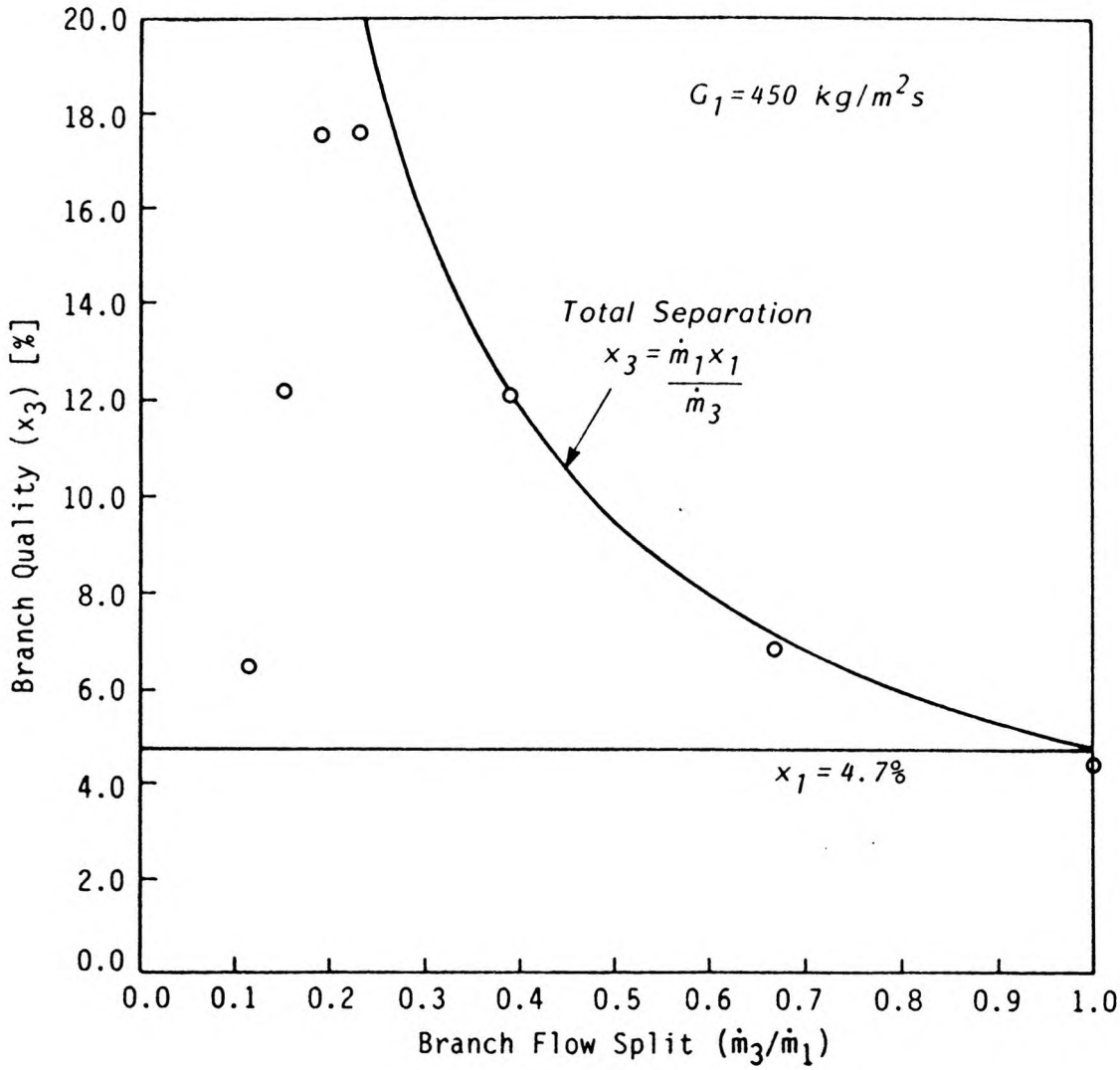

Figure 4.1 Branch Quality vs. Flow Split (G_1 = 450 kg/m^{2}s, x_1 = 4.7%)

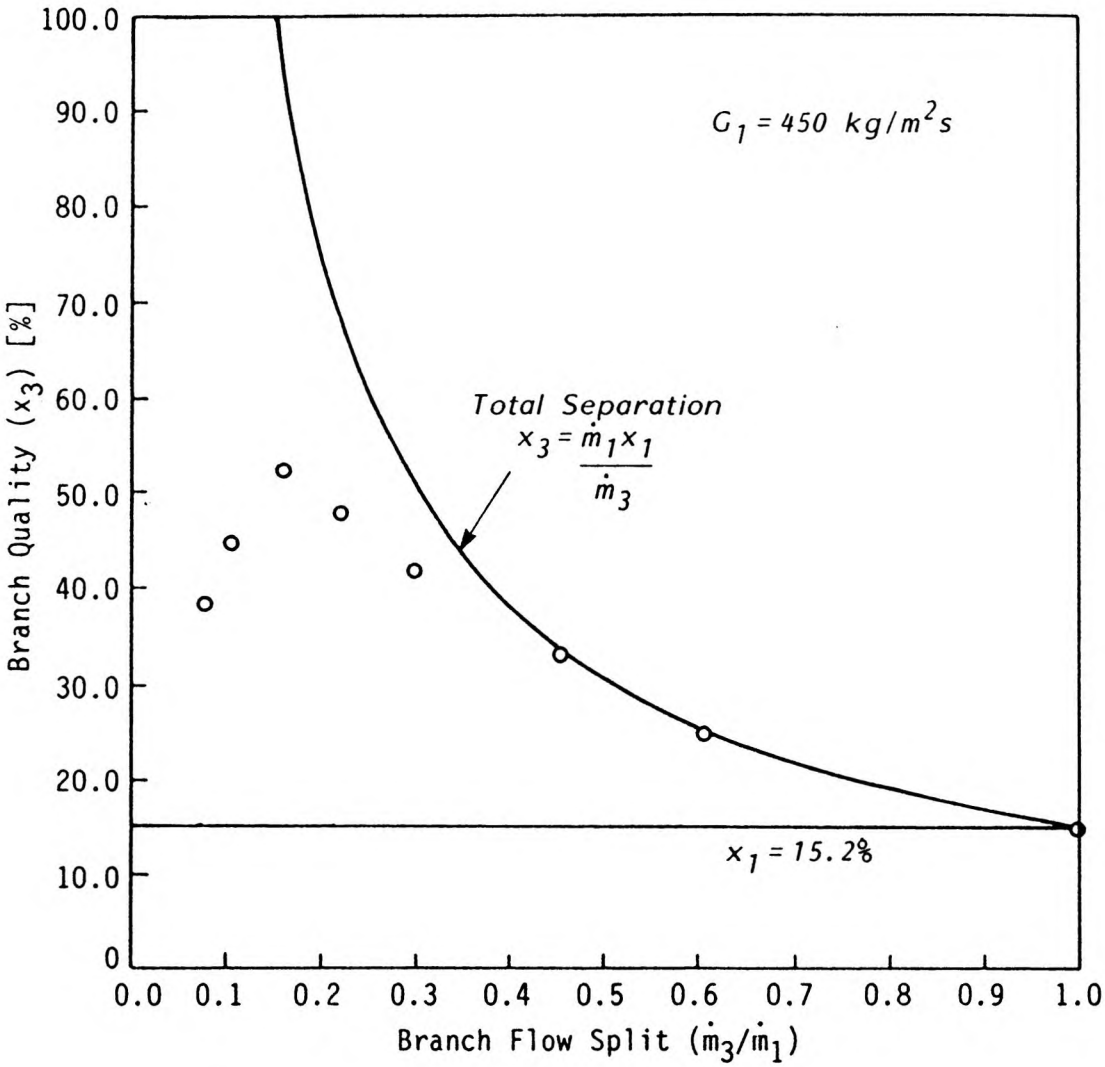

Figure 4.2 Branch Quality vs. Flow Split (G_1 = 450 kg/m²s, x_1 = 15.2%)

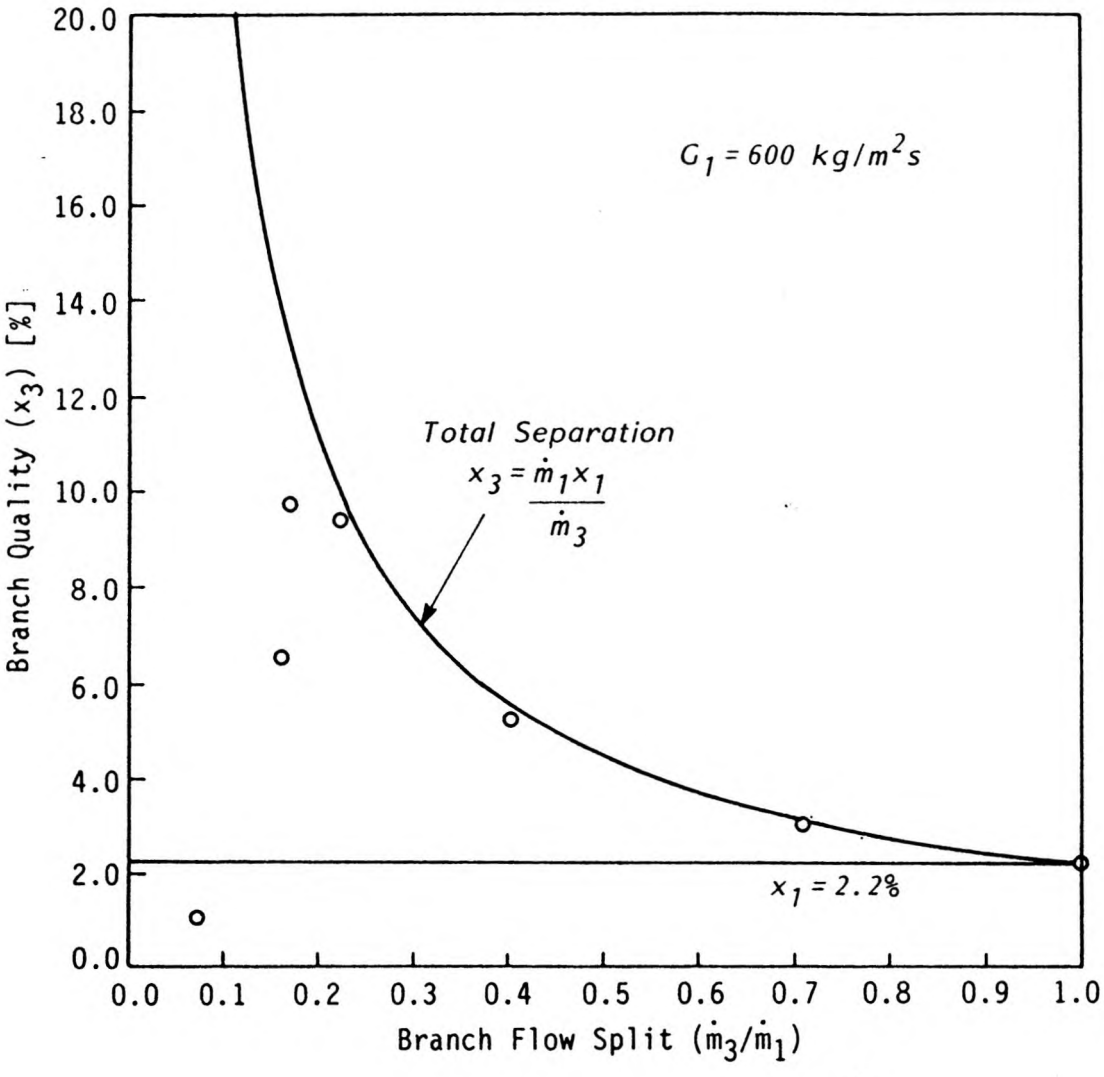

Figure 4.3 Branch Quality vs. Flow Split (G_1 = 600 kg/m²/s, x_1 = 2.2%)

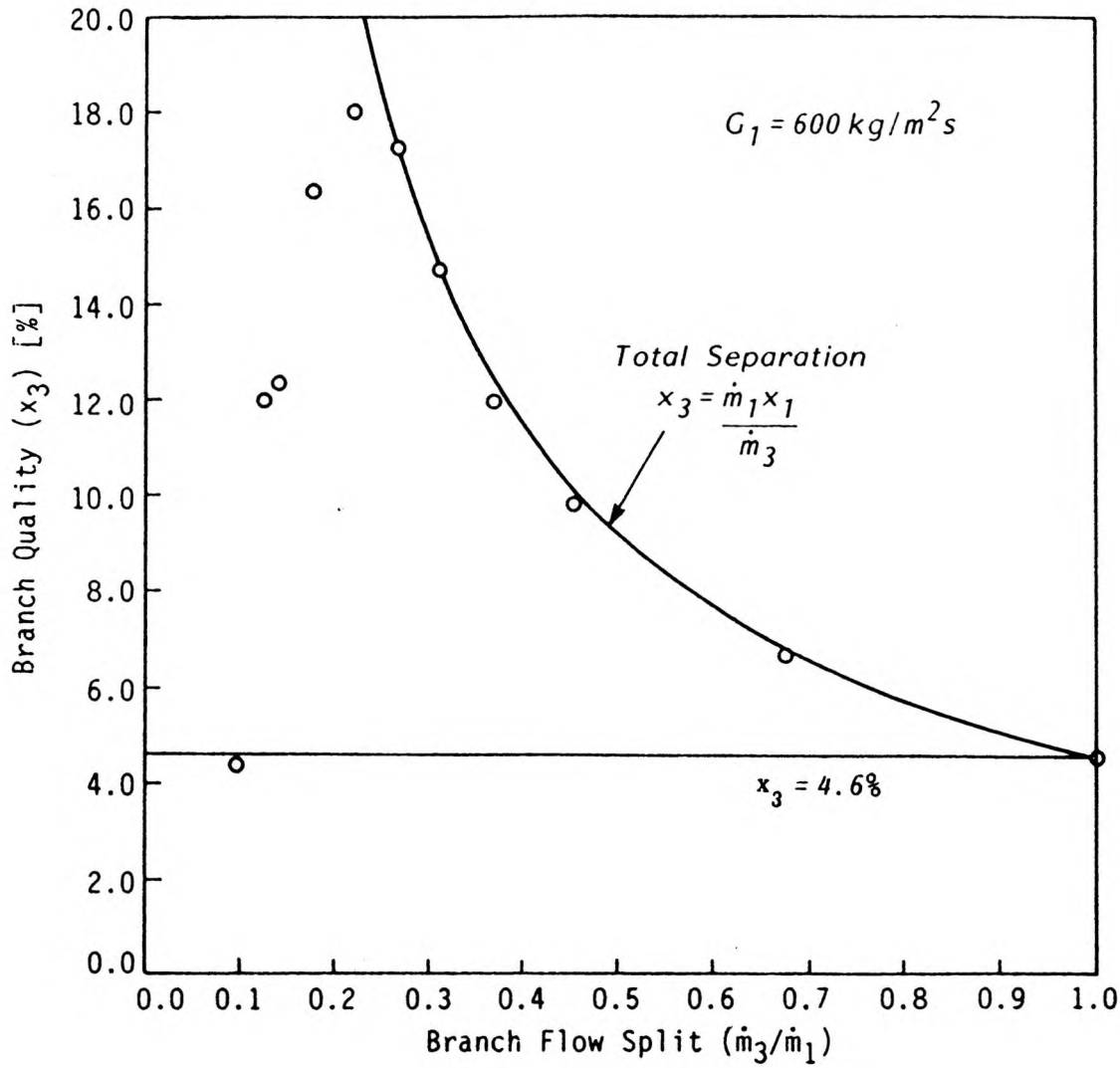

Figure 4.4 Branch Quality vs. Flow Split (G_1 = 600 kg/m²s, x_1 = 4.6%)

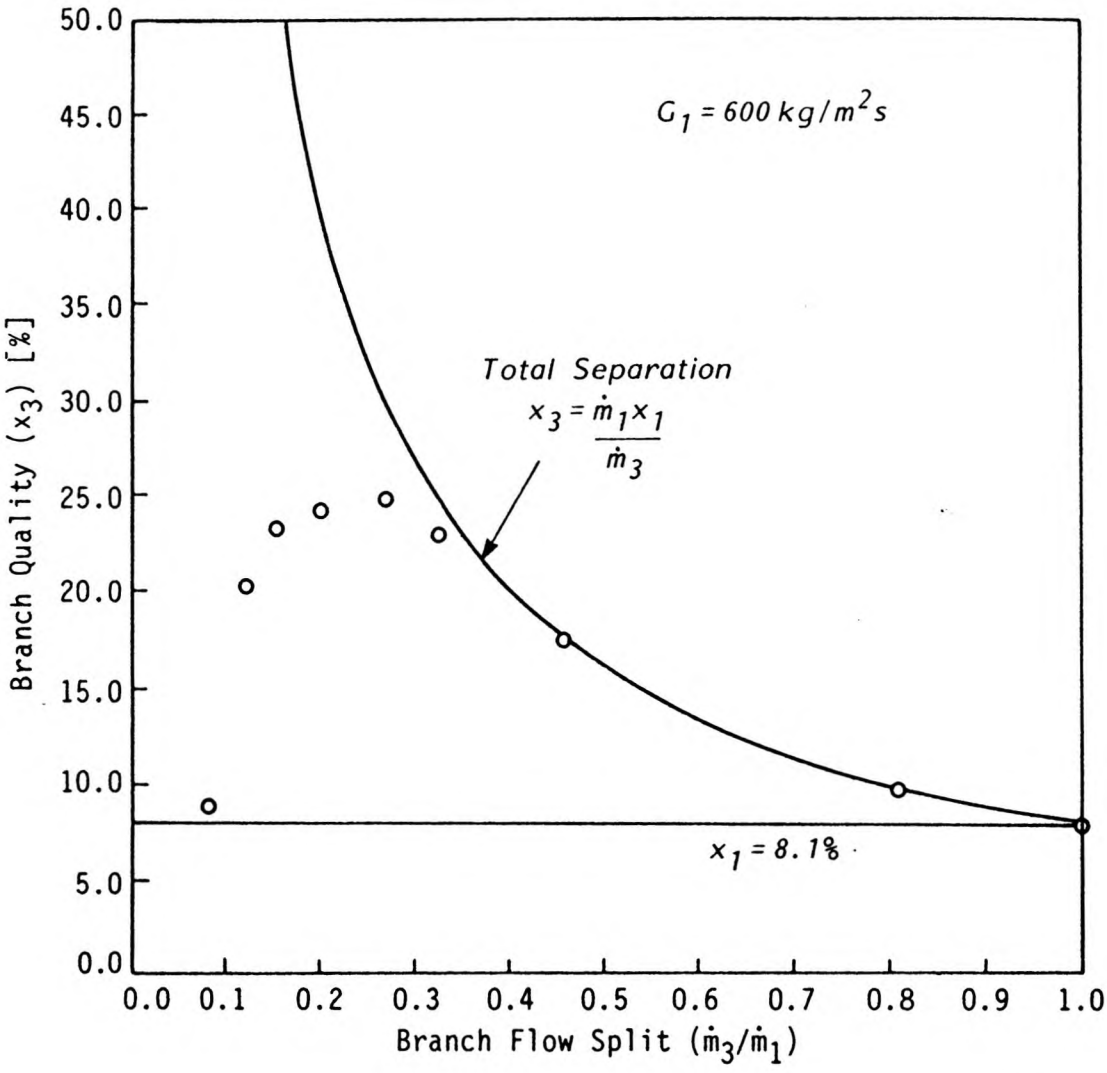

Figure 4.5 Branch Quality vs. Flow Split (G_1 = 600 kg/m^{2}s, x_1 = 8.0%)

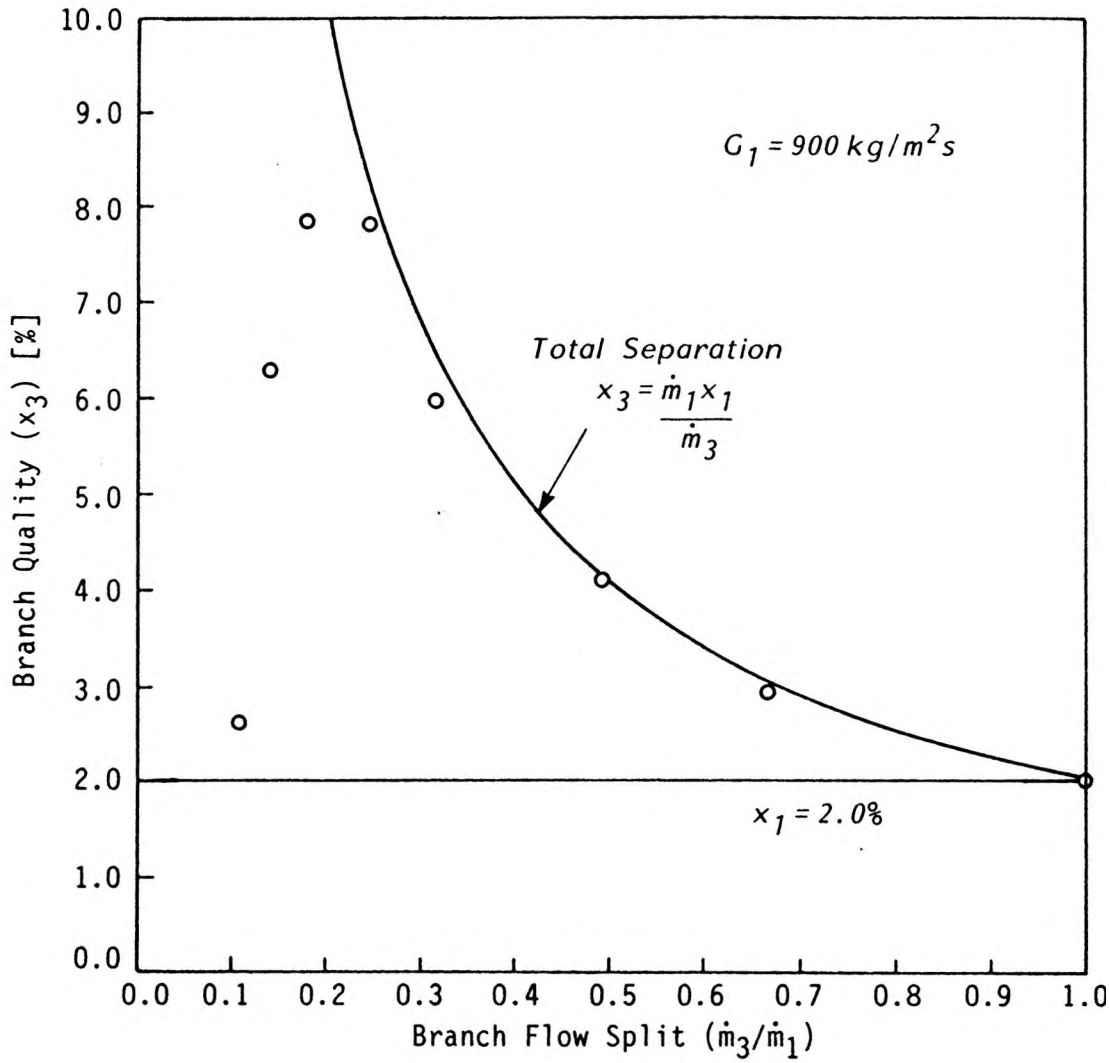

Figure 4.6 Branch Quality vs. Flow Split (G_1 = 900 kg/m²s, x_1 = 2.0%)

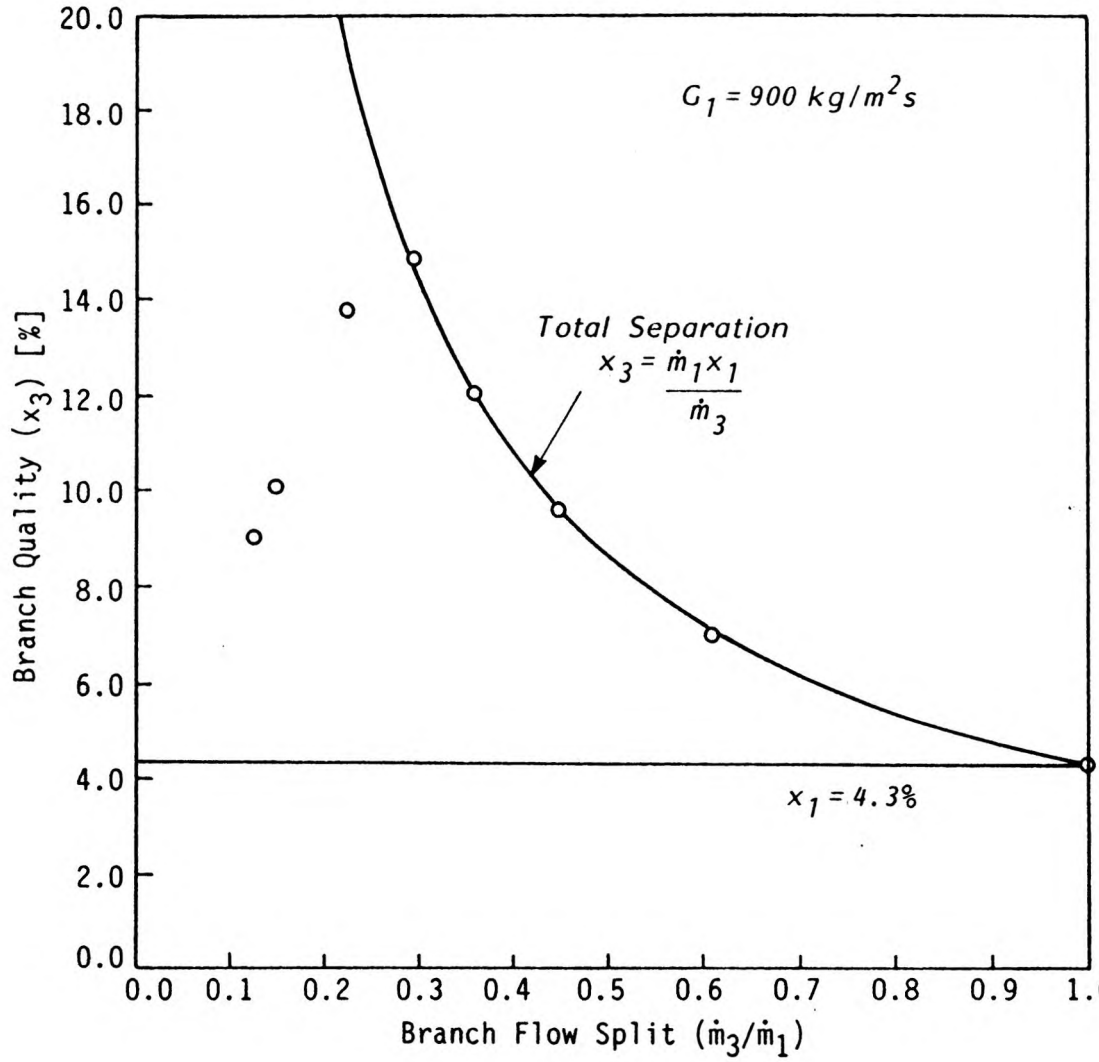

Figure 4.7 Branch Quality vs. Flow Split (G_1 = 900 kg/m²s, x_1 = 4.3%)

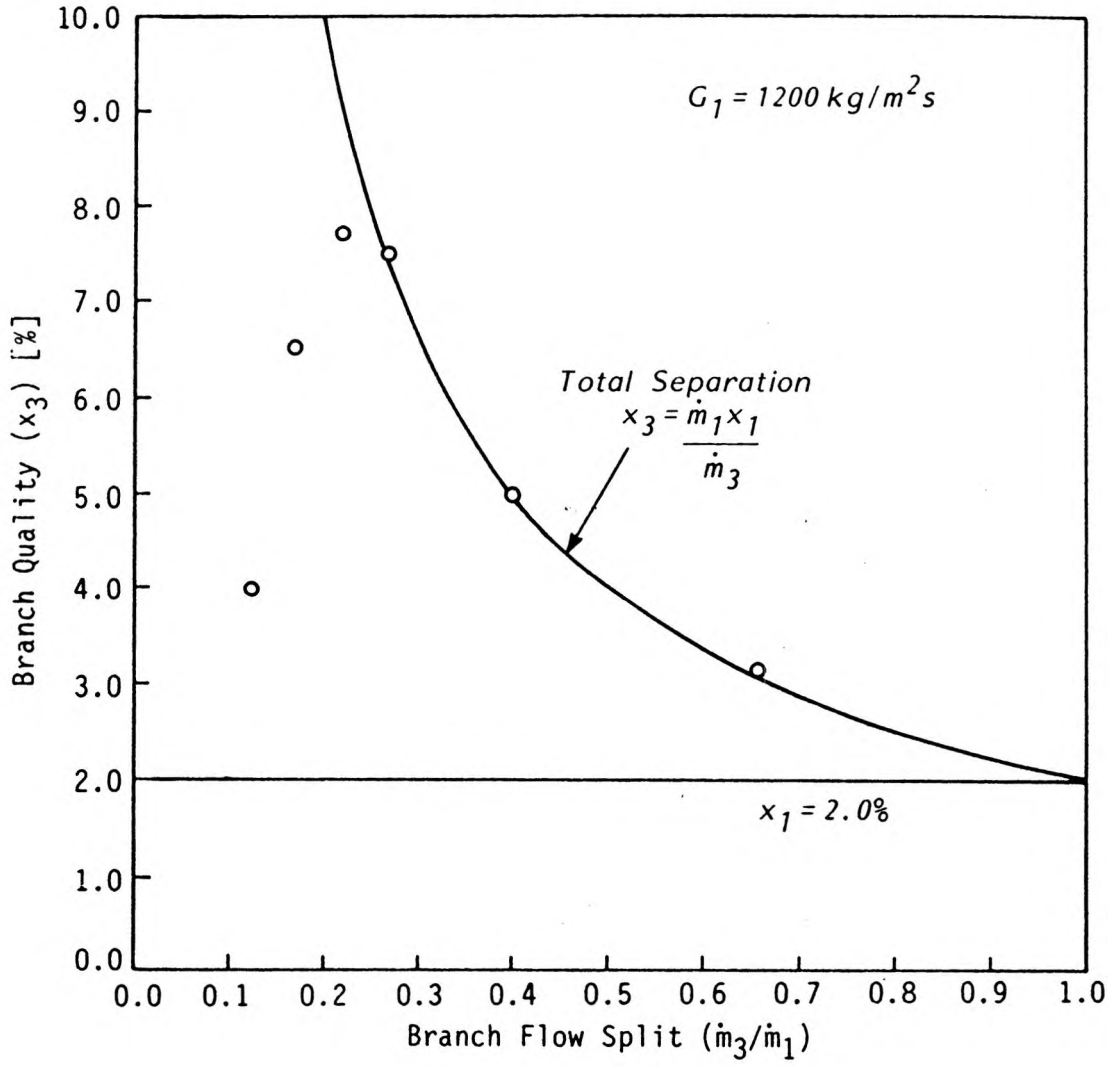

Figure 4.8 Branch Quality vs. Flow Split (G_1 = 1200 kg/m²s, x_1 = 2.0%)

assumption that all of the inlet steam flow is carried out through the branch, i.e.

$$x_3 = \frac{\dot{m}_1 x_1}{\dot{m}_3} \qquad \left(\frac{\dot{m}_3}{\dot{m}_1} \geq x_1\right) \tag{4.4}$$

This trend was observed by Saba and Lahey [10, 12] for air water flow in a horizontal tee section. For experiments in which no less than 30% of the total flow was removed through the branch, they reported branch qualities, in the range of total separation, that decreased with increasing flow split. Since these experiments were carried out with lower inlet qualities than the present work ($\leq$ 1.0%) and in all cases the inlet flow regimes were slug or stratified no direct comparison of the results can be made.

4.2.1 Effect of Inlet Quality

Normalizing the branch quality to the inlet quality yields the branch phase separation ratio (x_3/x_1). The total separation line is then represented by the inverse of the branch flow split, i.e.

$$\frac{x_3}{x_1} = \frac{\dot{m}_1}{\dot{m}_3} \qquad \left(\frac{\dot{m}_3}{\dot{m}_1} \geq x_1\right) \tag{4.5}$$

Figures 4.9 through 4.11 show the branch phase separation ratio plotted against flow split for a constant inlet mass flux and varying inlet quality. In all cases, an increase in inlet quality reduces the peak phase separation ratio and increases the flow split at which complete separation takes place. The data reported by St. Pierre et. al. [6] for annular flows of air and water in a horizontal tee section showed both these trends when replotted in this manner. This investigation was carried out with test sections having branch to inlet diameter ratios of 0.67 and 0.33. As a result, direct comparison between these results and the present work is not justified.

It has been suggested [6, 7, 10] that these observations may be explained in terms of the effect of quality variations on the distribution of the phases within the tube cross

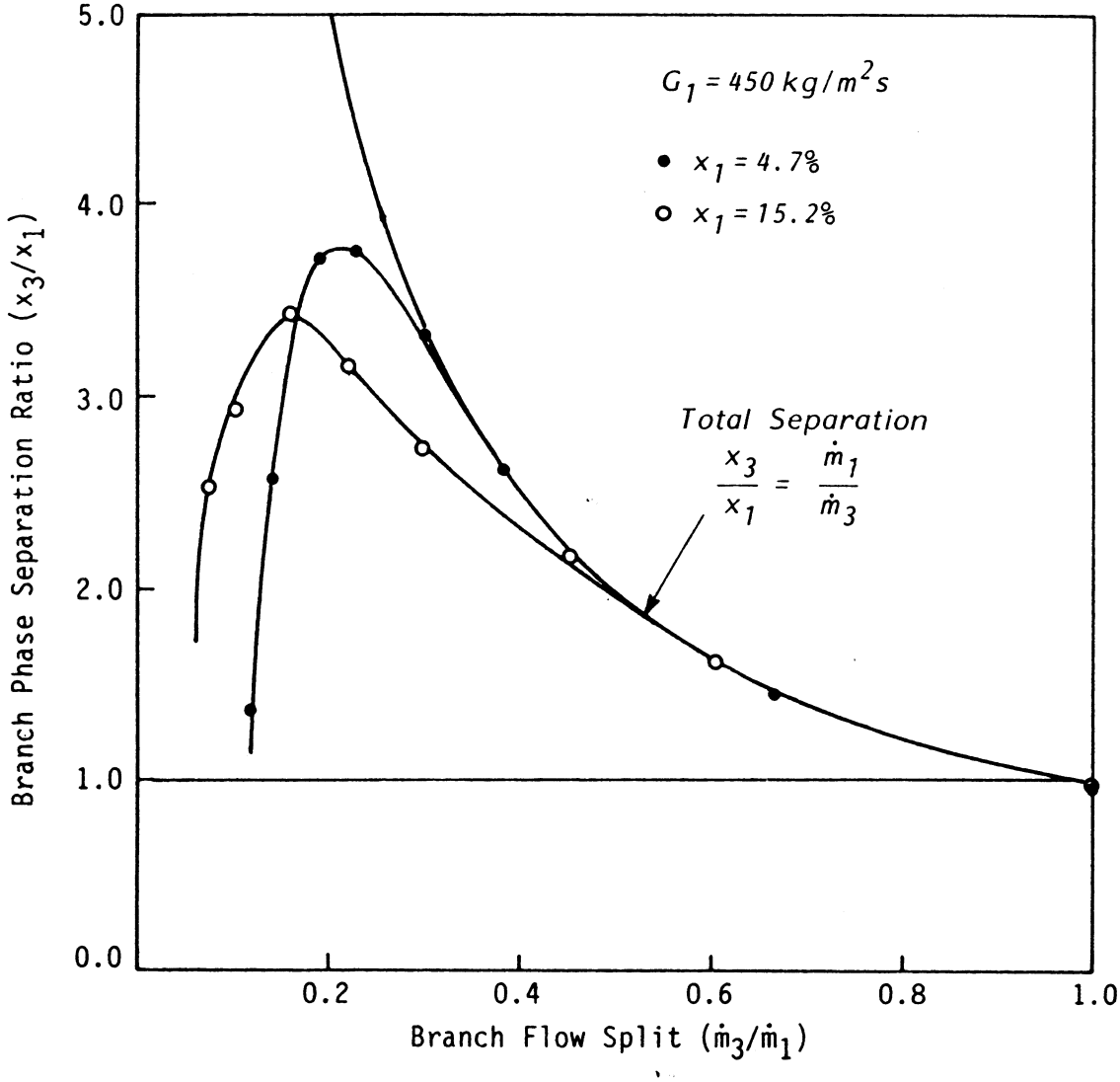

Figure 4.9 Branch Phase Separation Ratio vs. Flow Split, Effect of Inlet Quality (G_1 = 450 kg/m²s)

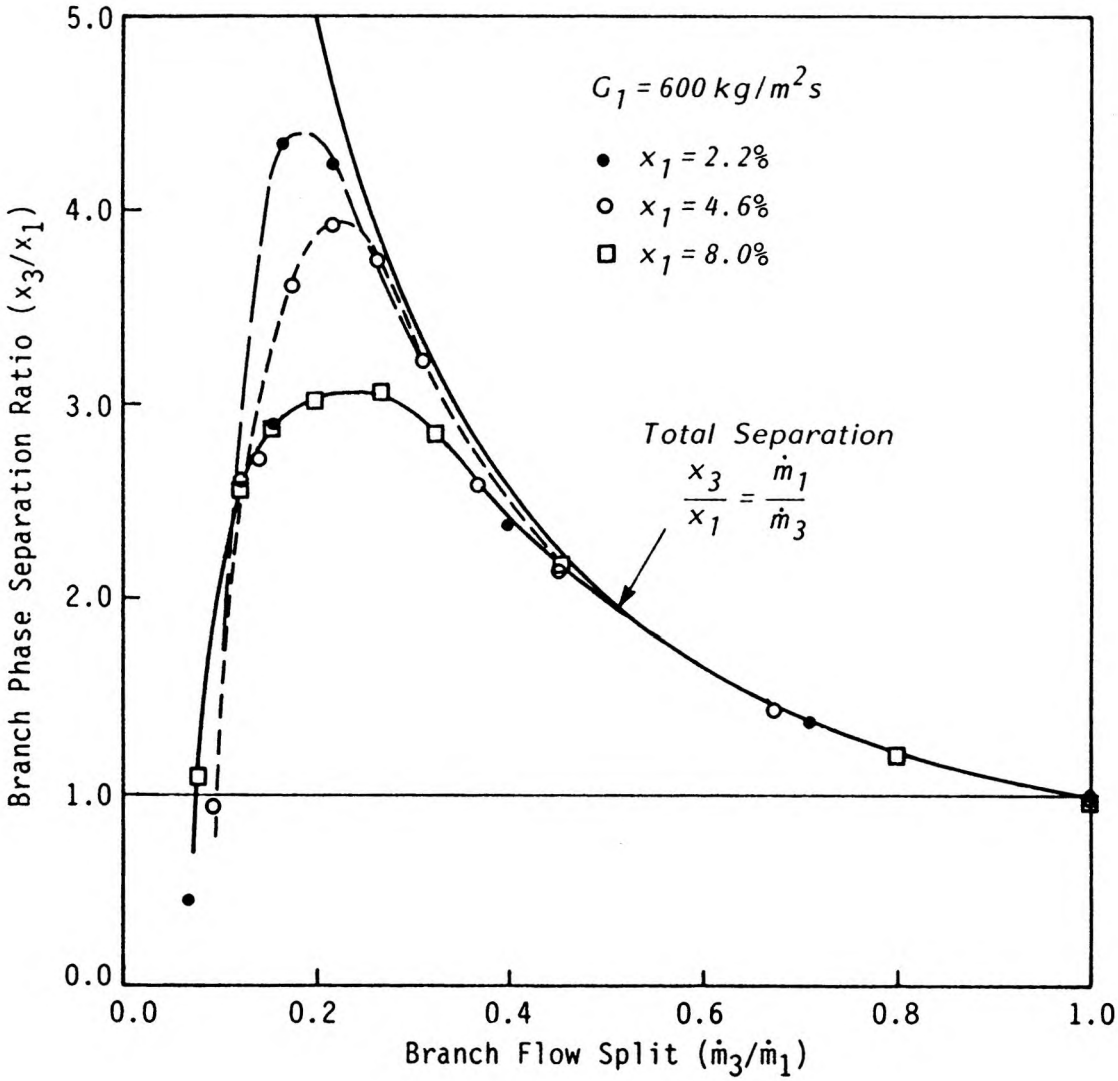

Figure 4.10 Branch Phase Separation Ratio vs. Flow Split, Effect of Inlet Quality ($G_1 = 600\ kg/m^2s$)

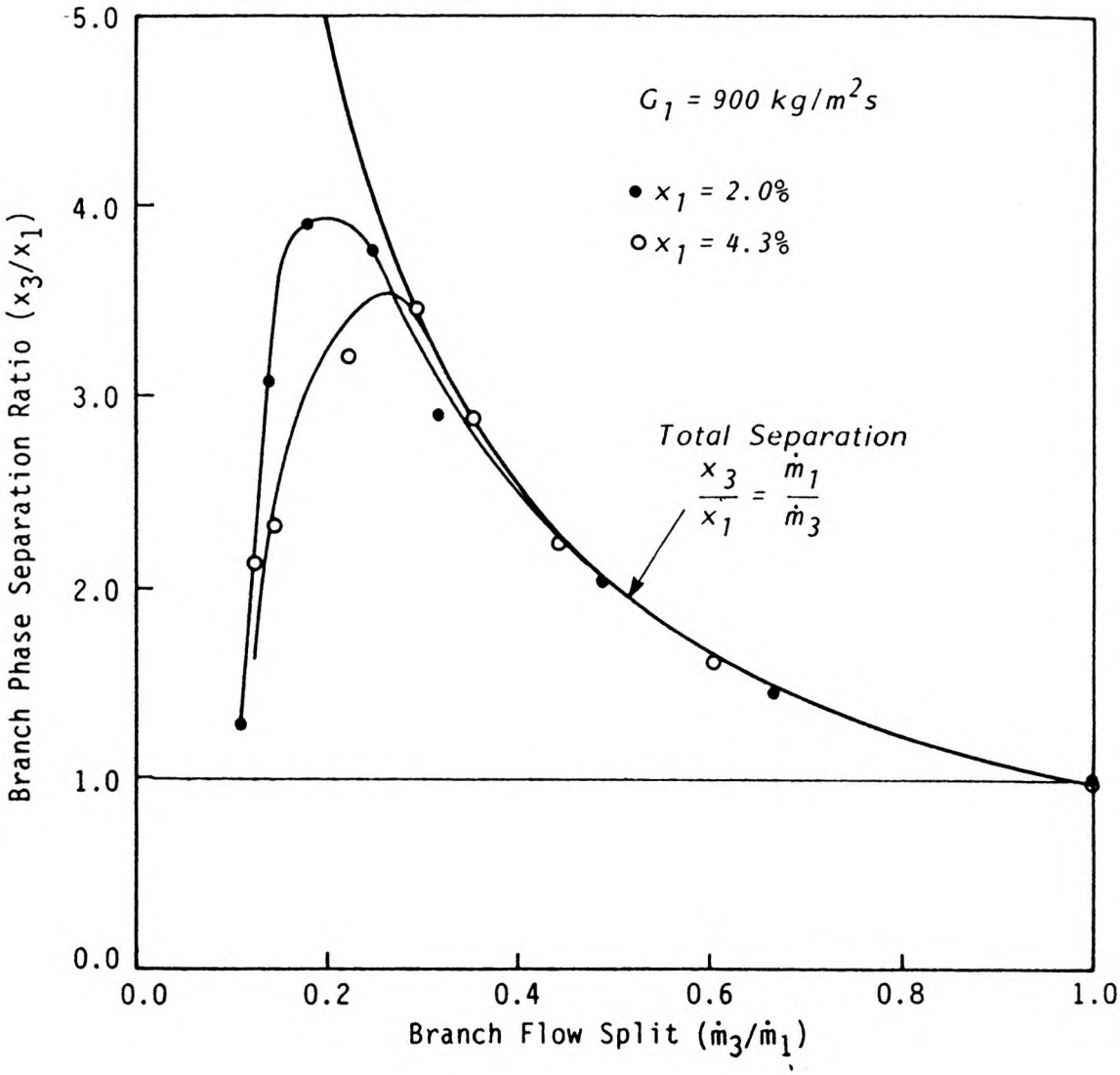

Figure 4.11 Branch Phase Separation Ratio vs. Flow Split, Effect of Inlet Quality (G_1 = 900 kg/m²s)

section and the relative distribution of momentum between the two phases. Increasing quality at constant mass flux in annular flow causes more of the liquid film to be swept up the sides of the tube from the thick layer of liquid on the bottom. As a result, more of the liquid film is readily available for extraction. This may be verified with data collected from test sections having smaller branch to inlet diameter ratios and with measurements of the angular distribution of film thickness in the inlet cross section.

4.2.2 Effect of Inlet Mass Flux

Figures 4.12 and 4.13 show the branch phase separation ratio plotted against branch flow split for fixed inlet quality at varying inlet mass flux. For the range of data tested the effects of inlet mass flux variations are less significant than those of inlet quality. The point of total separation is somewhat independent of inlet mass flux. The peak separation ratio appears to be slightly lower for the higher values of inlet mass flux (900 and 1200 kg/m^2s). The effect of mass flux on the annular flow data reported by St. Pierre et. al. [6] was also less significant than those of quality. As outlined above, no direct comparison can be made between these results and the present work due to the difference in branch to inlet diameter ratios.

As with the inlet quality, more information concerning the effects of mass flux on the inlet distribution of phase and momentum is required to explain these observations in terms of physical phenomena.

4.3 Single Phase Pressure Distribution

Single phase experiments were carried out with room temperature water at the conditions outlined in section 3.3.4. Once the desired inlet flow rate and branch flow split were established, pressure measurements were taken at stations 1 through 10 and 21 through

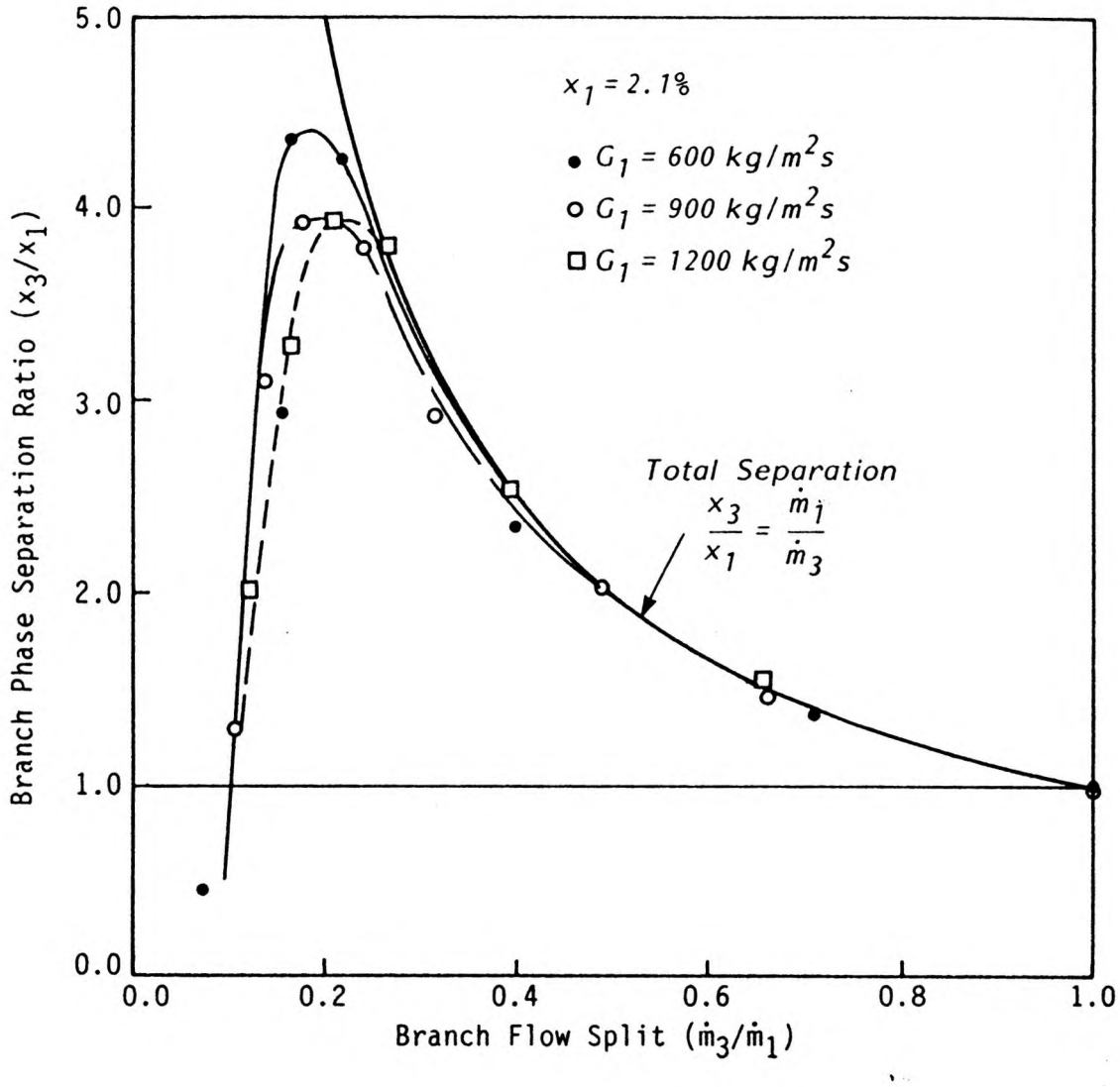

Figure 4.12 Branch Phase Separation Ratio vs. Flow Split, Effect of Inlet Mass Flux ($x_1 = 2.1\%$)

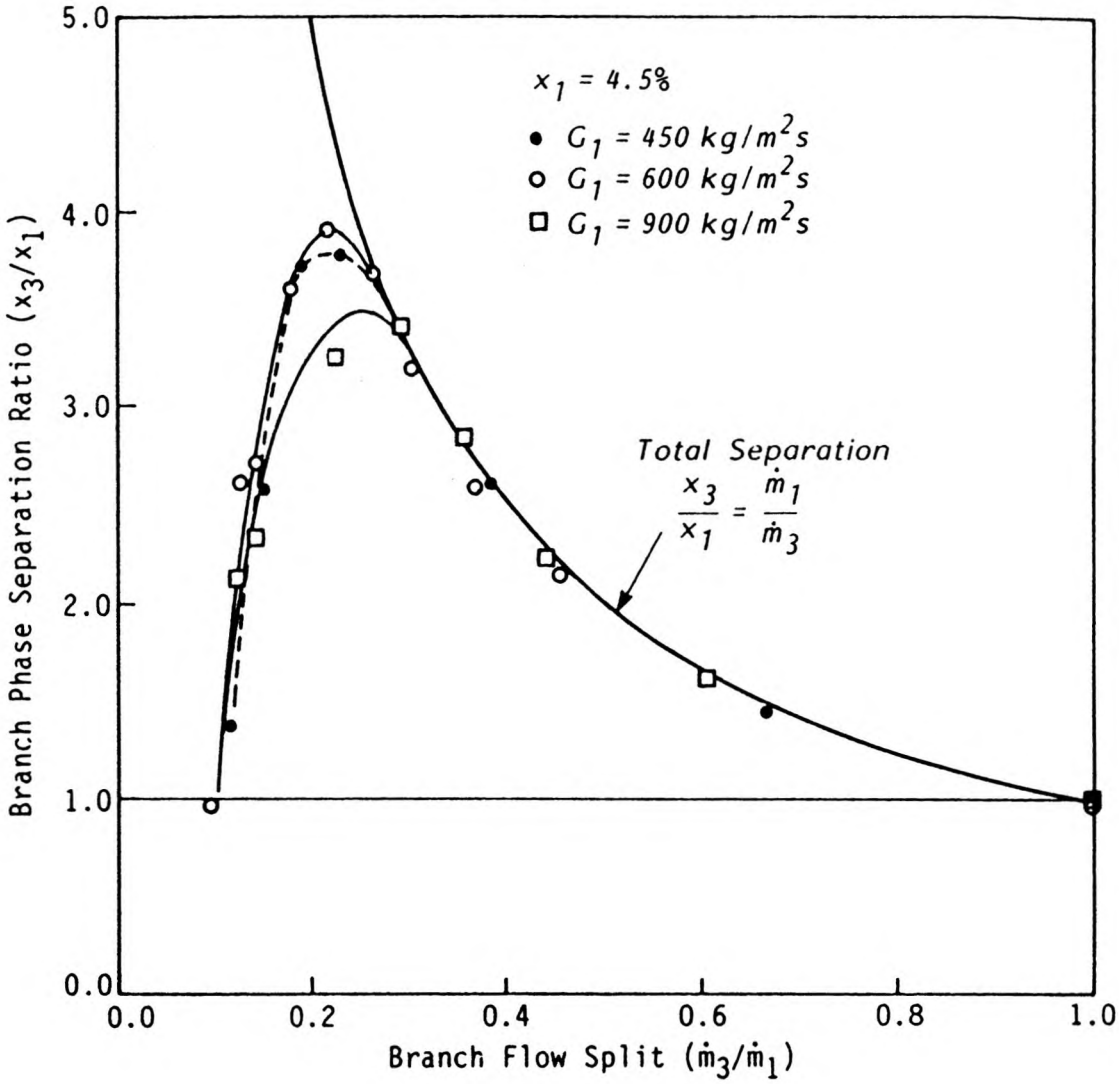

Figure 4.13 Branch Phase Separation Ratio vs. Flot Split, Effect of Inlet Mass Flux (x_1 = 4.5%)

25. For each run, the results were plotted and a linear least squares curve was fit through the fully developed regions of each leg. These were extrapolated to the junction to determine the junction pressure differentials [$(\Delta P_{2-1})_j$, $(\Delta P_{1-3})_j$]. Figure 4.14 shows some typical results for a nominal inlet mass flux of 900 kg/m^{2}s and a branch flow split ($\dot{m}_3/\dot{m}_1$) of 0.7. The remaining single phase data is tabulated in Appendix D.

4.3.1 Axial Pressure Recovery

Both the energy and the momentum equation may be written for the flow in the axial direction through the run of the tee. In the energy equation, a term must appear to account for irreversible losses at the junction. In the momentum equation, a term must be included to account for either the axial component of momentum carried out by the branching flow or the axial component of force at the branch which reduces this momentum to zero. If it is assumed that the average velocity in the inlet and run of the tee (u_1 and u_2 respectively) is representative of the flow field, the energy equation may be written as

$$\frac{(\Delta P_{2-1})_j}{\frac{\rho u_1^2}{2}} = 1 - \left(\frac{u_2}{u_1}\right)^2 - \frac{h_{f\,1-2}}{\frac{u_1^2}{2g}} \tag{4.6}$$

where h_{f1-2} represents the irreversible head loss at the junction. Under the same assumption, the momentum equation yields

$$(\Delta P_{2-1})_j = k_{1-2}(\rho u_1^2 - \rho u_2^2) \tag{4.7}$$

where k_{1-2} accounts for the indeterminant axial momentum lost to the branching flow.

Figure 4.15 shows both the axial momentum correction factor (k_{1-2}) and the axial pressure rise normalized to the inlet dynamic pressure plotted against flow split for all single phase runs. Shown also are the axial pressure rise predicted from the energy equation (eqn. 4.6) with no friction losses ($h_{f1-2} = 0$) and with friction losses equal to that for an

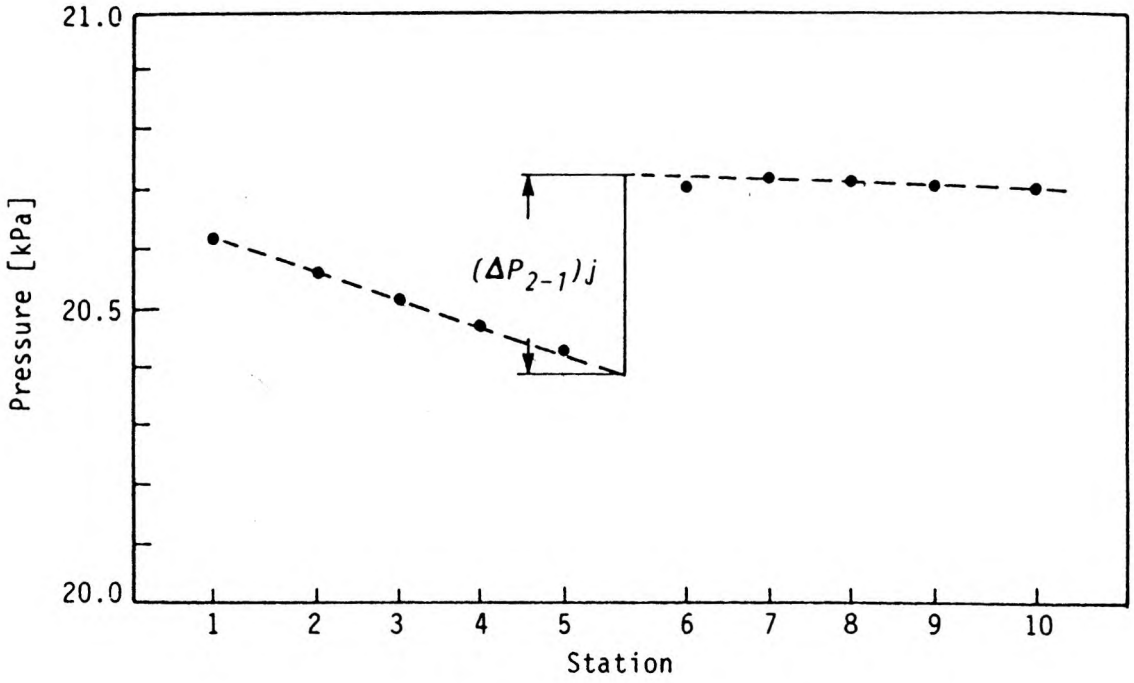

(a) Run Pressure Distribution

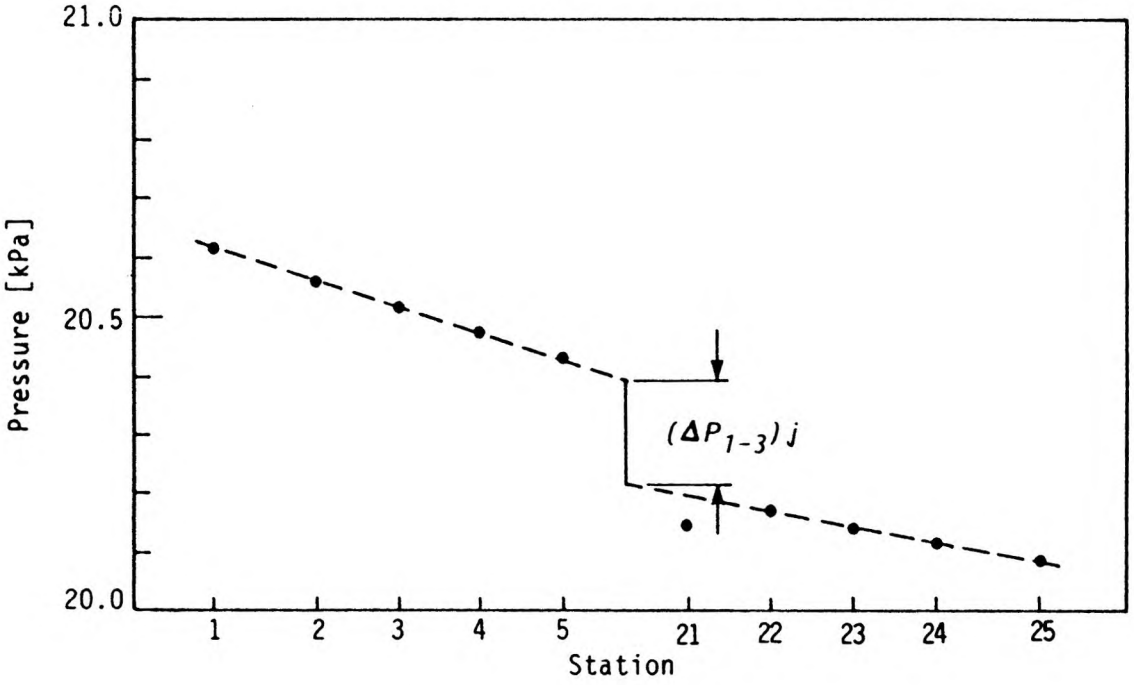

(b) Branch Pressure Distribution

Figure 4.14 Single Phase Pressure Distribution (G_1 = 900 kg/m²s, $\dot{m}_3/\dot{m}_1$ = 0.7)

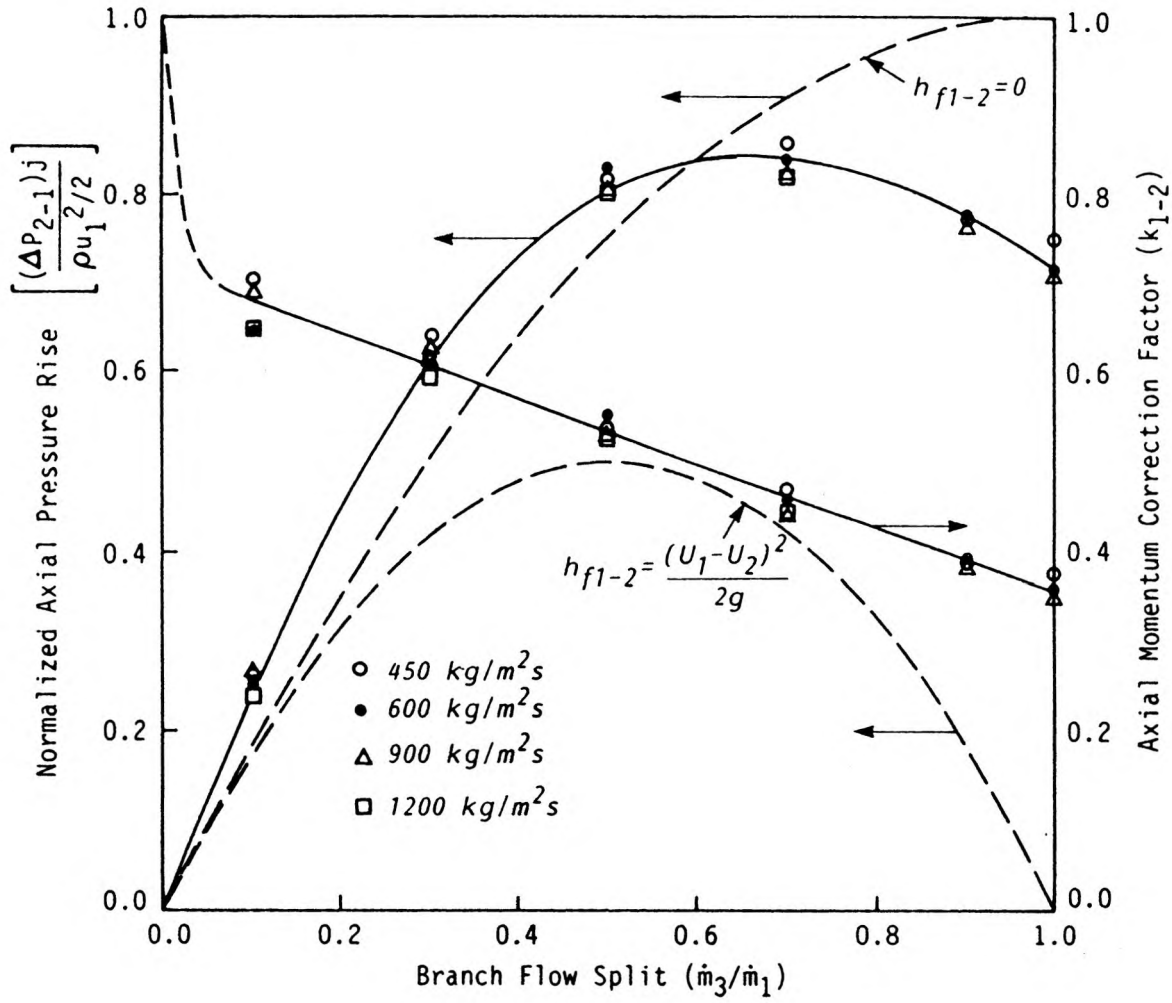

Figure 4.15 Single Phase Axial Pressure Rise and Momentum Correction Factor vs. Flow Split

abrupt expansion yielding the same down stream to up stream velocity ratio ($h_{f1-2} = (u_1 - u_2)^2/2g$). It is clear that the data are correlated based on the momentum equation. A unique relationship exists between k_{1-2} and the flow split independent of the inlet mass flux. For the range of data tested this relationship may be approximated by

$$k_{1-2} = .704 - .320\,(\dot{m}_3/\dot{m}_1) - .028\,(\dot{m}_3/\dot{m}_1)^2 \qquad (\dot{m}_3/\dot{m}_1 > 0.1) \qquad (4.8)$$

As the branch flow split approaches zero the momentum correction factor would be expected to approach a value of unity [6]. This portion of the curve is shown dashed, indicating no supporting data. These results agree well with those compiled by McNown [18] shown in Figure 4.16.

4.3.2 Radial Pressure Drop

The energy equation may also be written for the branching flow with a term included to account for irreversible losses at the junction. If the average velocity in the inlet and branch (u_1 and u_3 respectively) is assumed to be representative of the flow field the energy equation becomes,

$$\frac{(\Delta P_{1-3})_j}{\frac{\rho u_1^2}{2}} = \frac{u_3^2}{u_1^2} - 1 + k_{1-3} \qquad (4.9)$$

The branch loss coefficient k_{1-3} represents the irreversible head loss normalized to the inlet dynamic head. Figure 4.17 shows k_{1-3} as a function of flow split ($\dot{m}_3/\dot{m}_1$). Again, a unique relationship exists, independent of mass flux, which is best represented by

$$k_{1-3} = 1.081 - .914\,(\dot{m}_3/\dot{m}_1) + 1.050\,(\dot{m}_3/\dot{m}_1)^2 \qquad (4.10)$$

These results also agree well with those presented by McNown [18] shown in Figure 4.18.

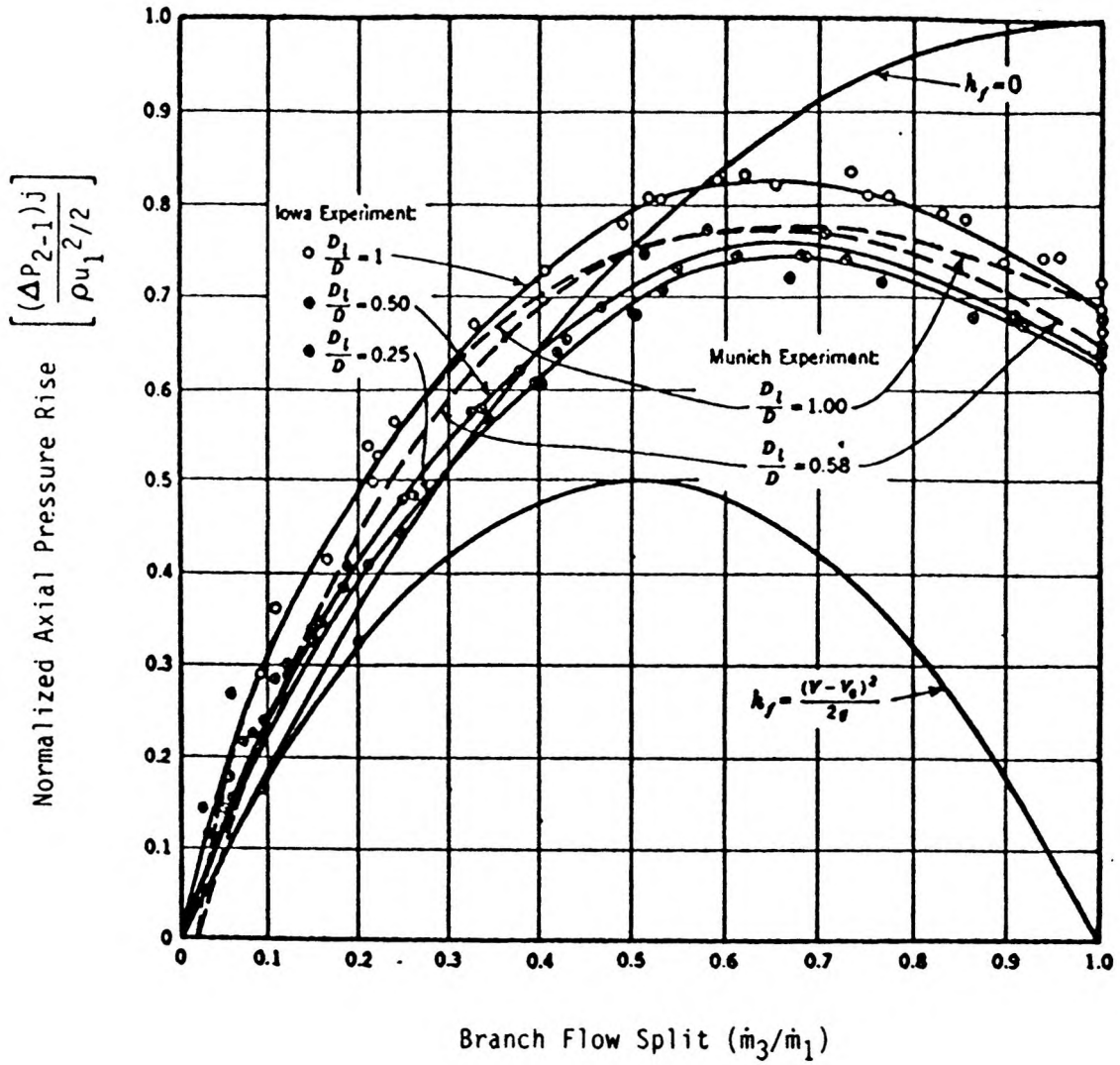

Figure 4.16 Single Phase Axial Pressure Rise vs. Flow Split (after [18])

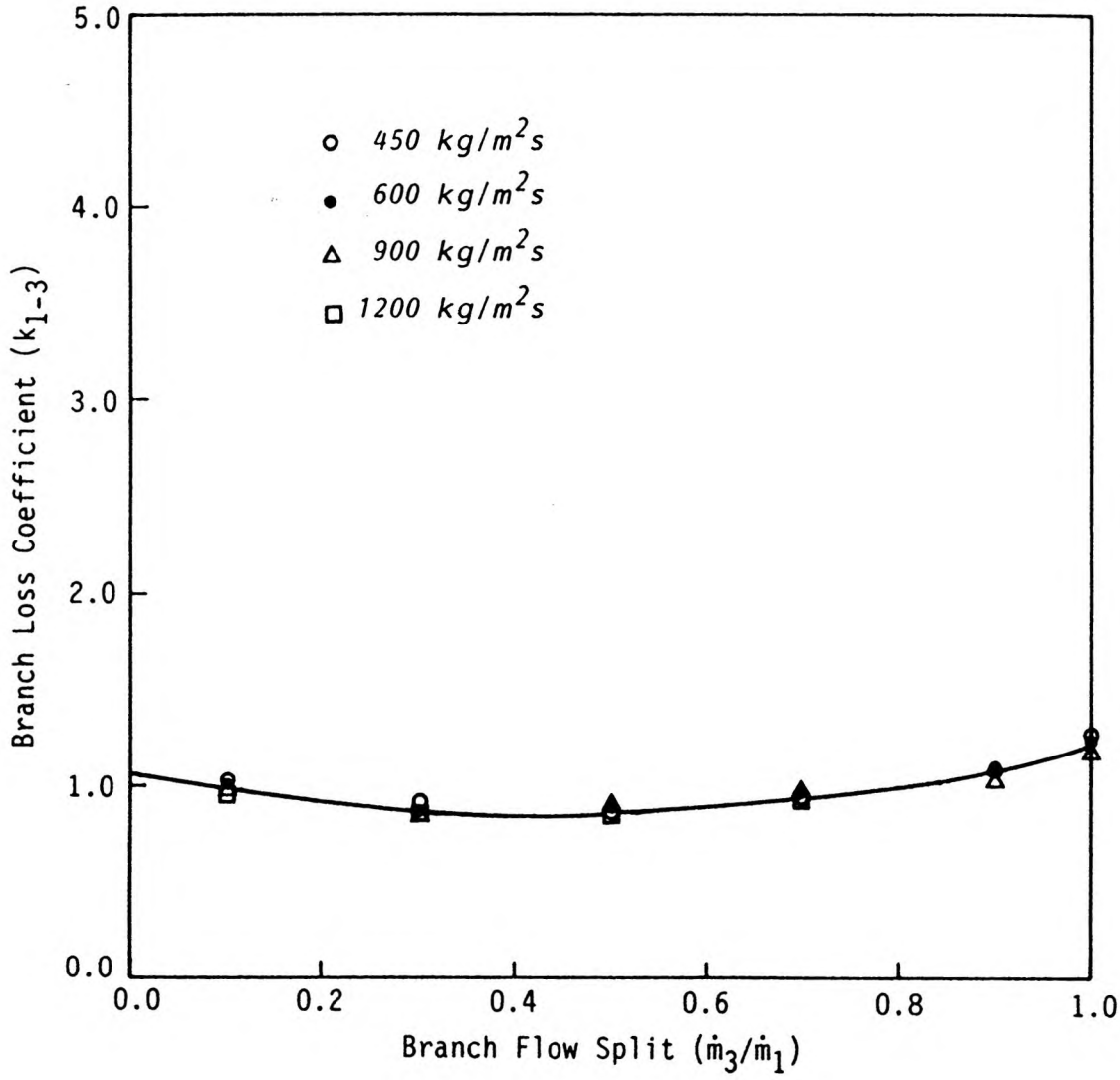

Figure 4.17 Single Phase Branch Loss Coefficient vs. Flow Split

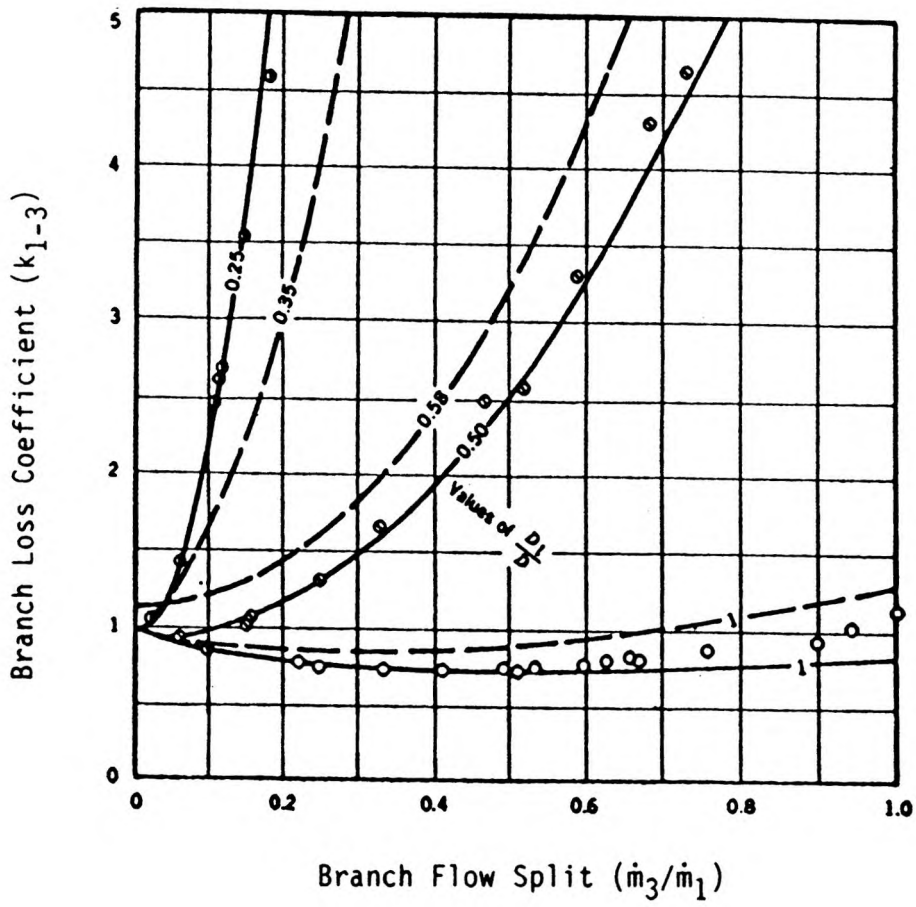

Figure 4.18 Single Phase Branch Loss Coefficient vs. Flow Split (after [18])

4.4 Two-Phase Pressure Distribution

The inlet and branching sections were sufficiently long to ensure that fully developed flow was established within the test section. For these two legs, five pressure taps over 610 mm (L/D ≃ 25) were sufficient to obtain the fully developed pressure profiles. In the run, which carried most of the low quality flows, the development length was significantly longer, often exceeding 50 pipe diameters. This leg was extended to include 15 pressure taps over 2339 mm to ensure that a fully developed profile was measured.

Typical pressure distributions for two phase dividing flows are shown in Figures 4.19 and 4.20. In Figure 4.19, the flow split is below that required for total separation ($\dot{m}_3/\dot{m}_1 = 0.18$) and in Figure 4.20 it is greater ($\dot{m}_3/\dot{m}_1 = 0.31$). The corresponding measured void fraction profiles are shown in Figures 4.21 and 4.22. In general, it appears that total separation is associated with a significant increase in the run pressure differential $(\Delta P_{2-1})_j$ and a decrease in the run void fraction, quality and fully developed frictional pressure gradient. These observations are consistent with a flow regime transition occuring in the run at or near complete separation.

Further evidence of this may be seen by plotting the run flow conditions on a flow regime map such as Baker's map shown in Figure 4.23. Transition from annular flow in the run appears to take place at a flow split greater than 0.18.

4.4.1 Two-Phase Axial Pressure Recovery

The pressure recovery through the run of the tee was modelled from a momentum balance at the junction based on both homogeneous and separated flow assumptions. The two-phase homogeneous equation corresponding to equation 4.7 may be written

$$(\Delta P_{2-1})_j = k_{(1-2)h}[(\rho_h u_h^2)_1 - (\rho_h u_h^2)_2] \tag{4.11}$$

where ρ_h and u_h are respectively the homogeneous density and velocity given by

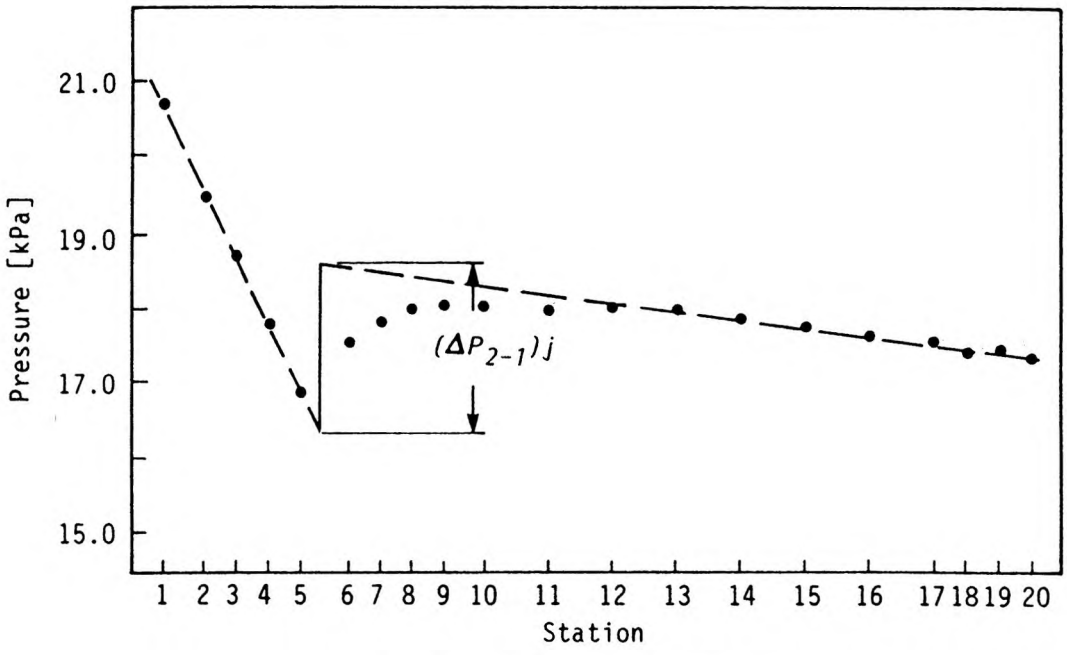

(a) Run Pressure Distribution

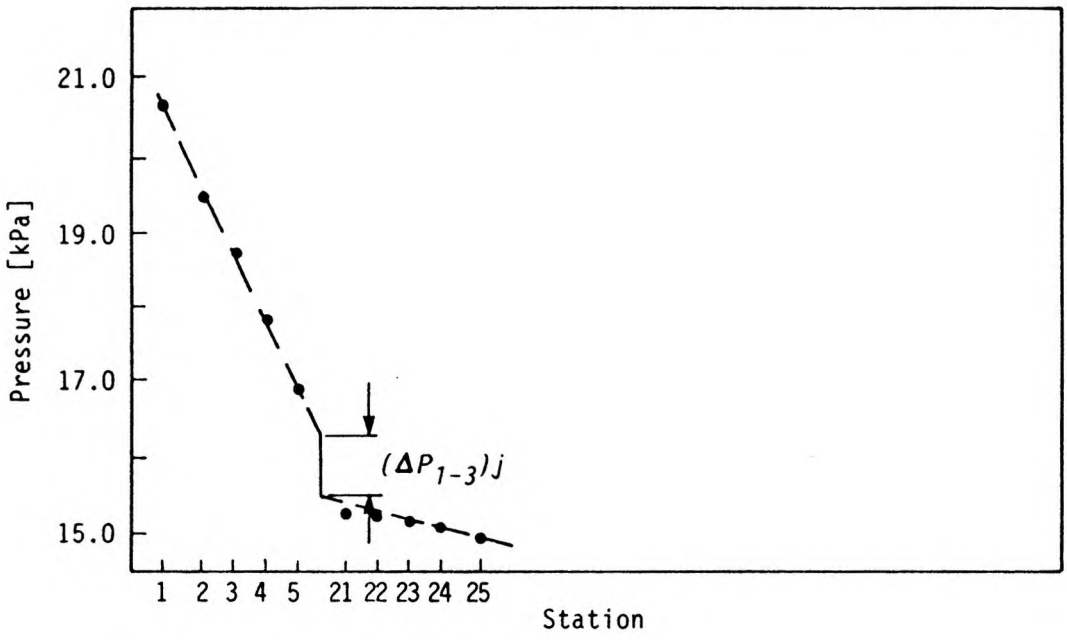

(b) Branch Pressure Distribution

Figure 4.19 Two-Phase Pressure Distribution (G_1 = 600 kg/m²s, x_1 = 4.5%, $\dot{m}_3/\dot{m}_1$ = 0.18)

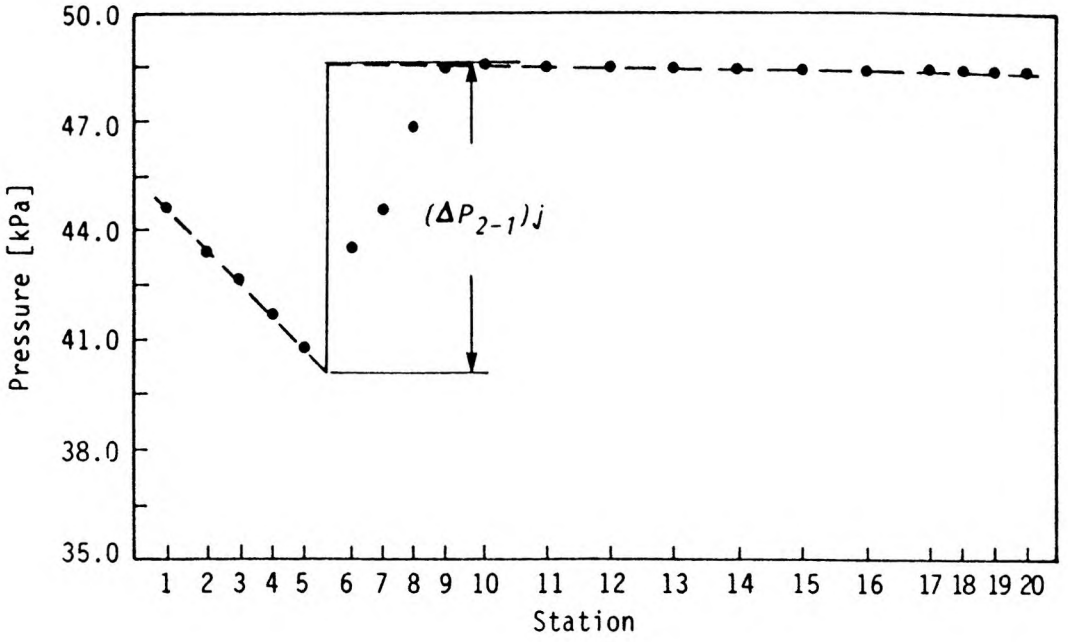

(a) Run Pressure Distribution

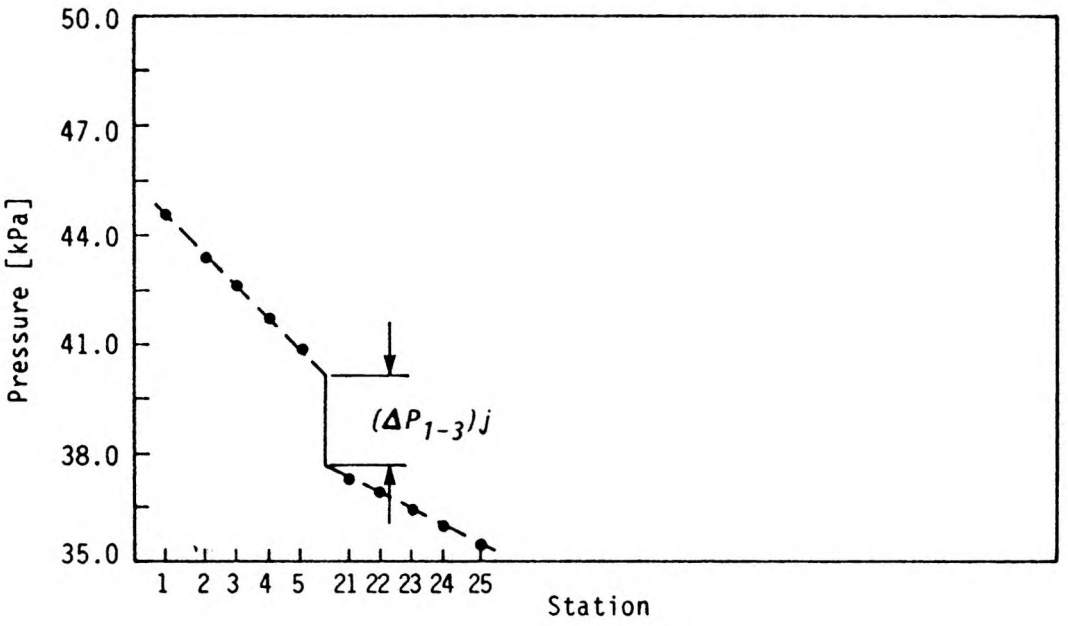

(b) Branch Pressure Distribution

Figure 4.20 Two-Phase Pressure Distribution (G_1 = 600 kg/m²s, x_1 = 4.9%, $\dot{m}_3/\dot{m}_1$ = 0.31)

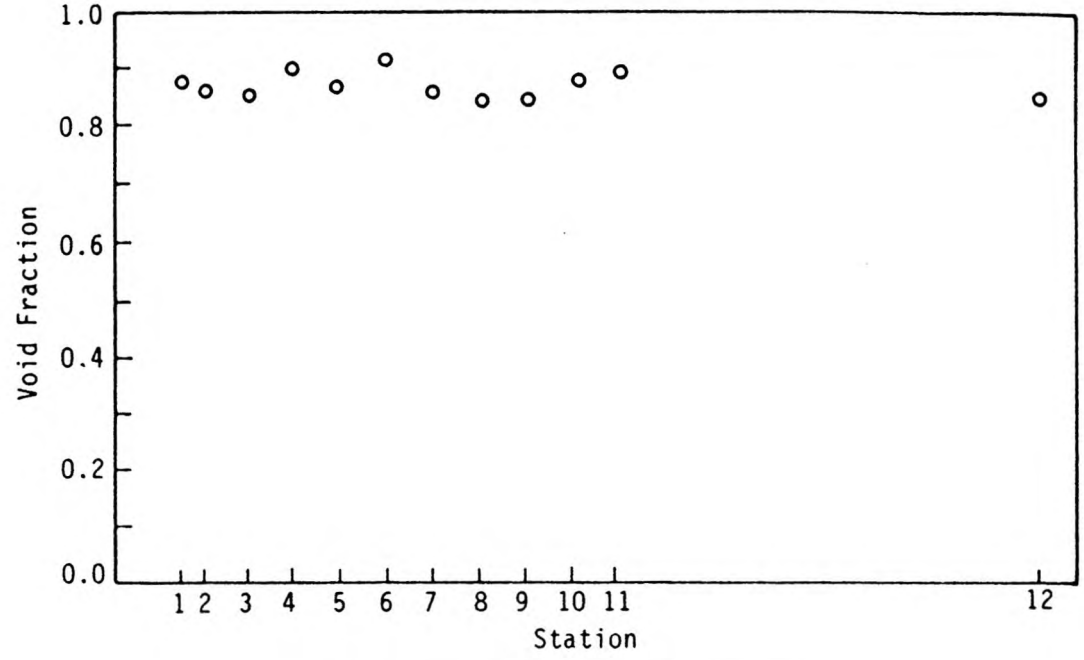

(a) Run Void Fraction Distribution

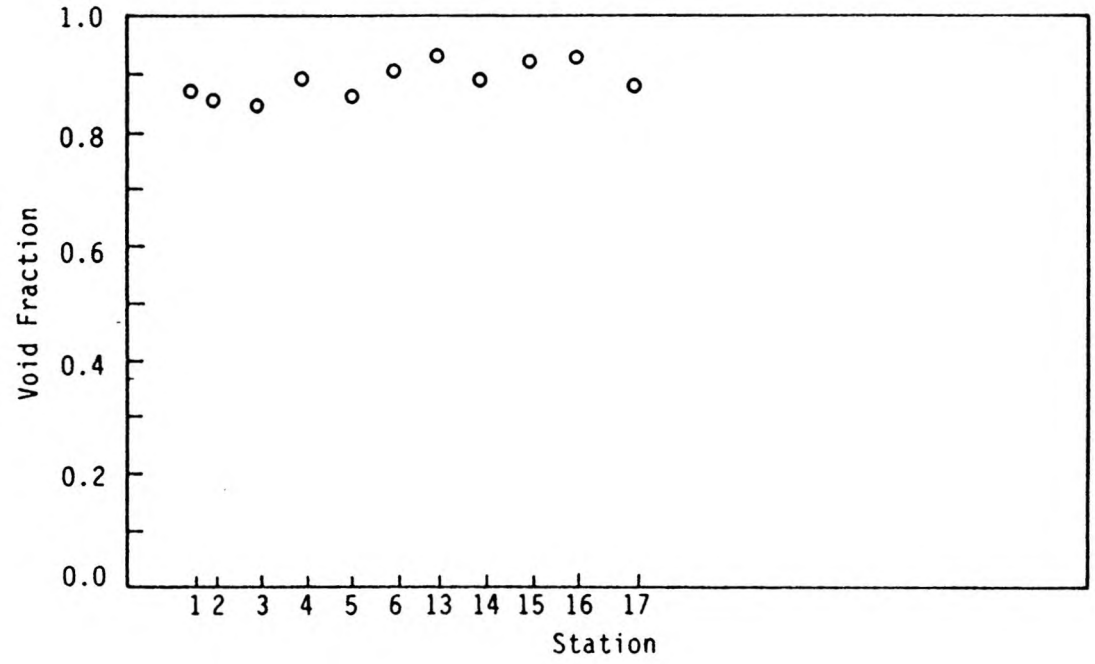

(b) Branch Void Fraction Distribution

Figure 4.21 Void Fraction Distribution ($G_1 = 600$ kg/m^{2}s, $x_1 = 4.5\%$, $\dot{m}_3/\dot{m}_1 = 0.18$)

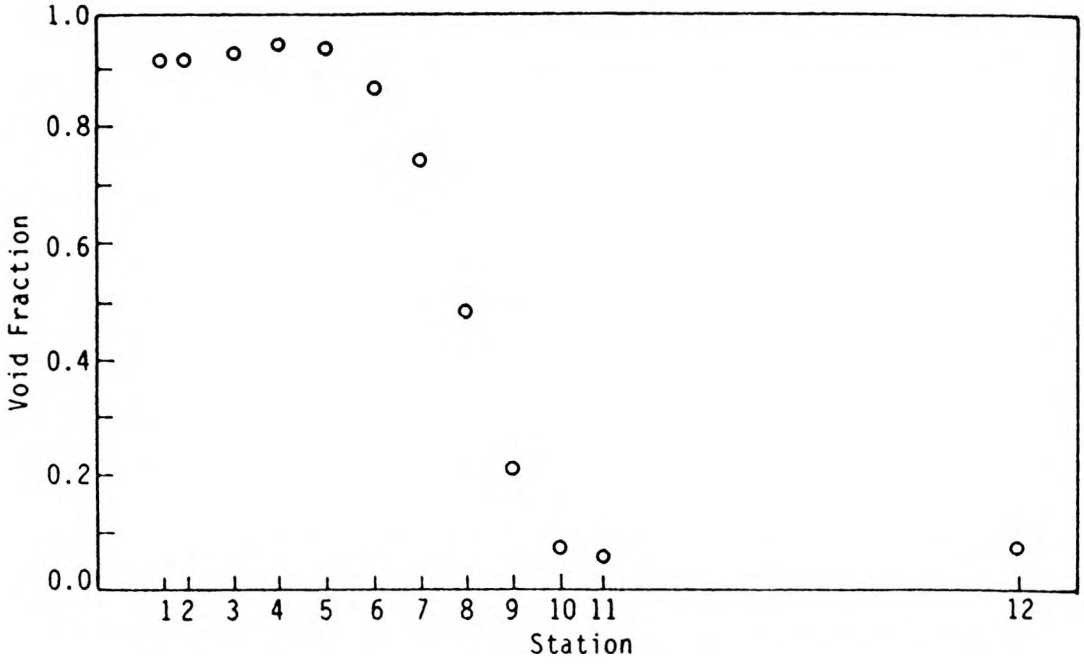

(a) Run Void Fraction Distribution

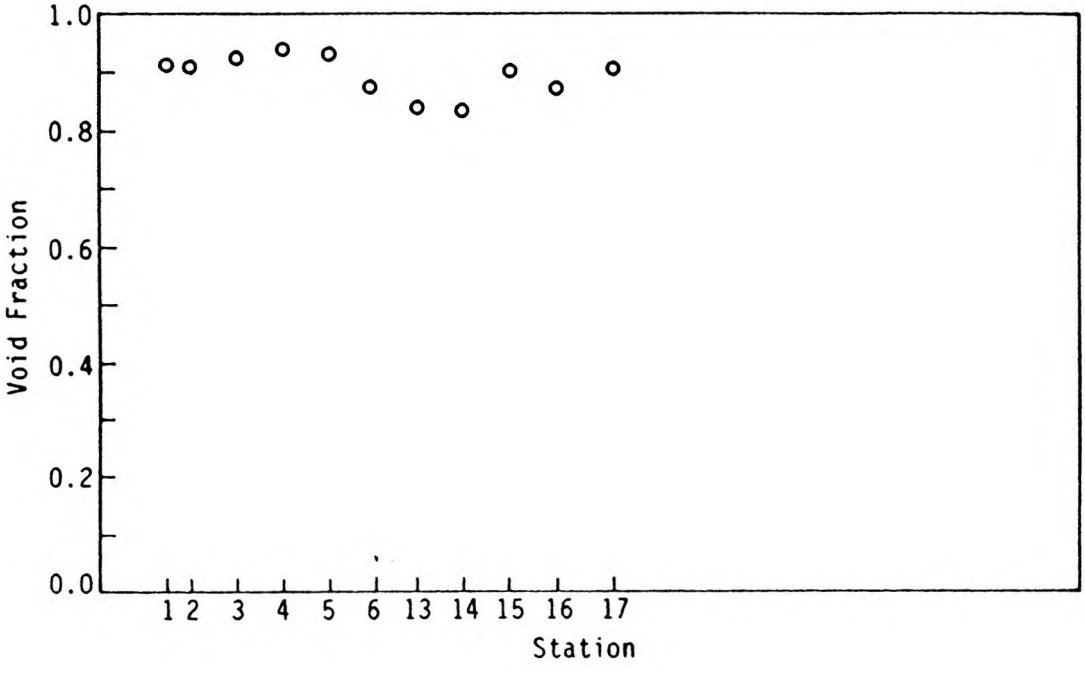

(b) Branch Void Fraction Distribution

Figure 4.22 Void Fraction Distribution (G_1 = 600 kg/m^{2}s, x_1 = 4.9%, $\dot{m}_3/\dot{m}_1$ = 0.31)

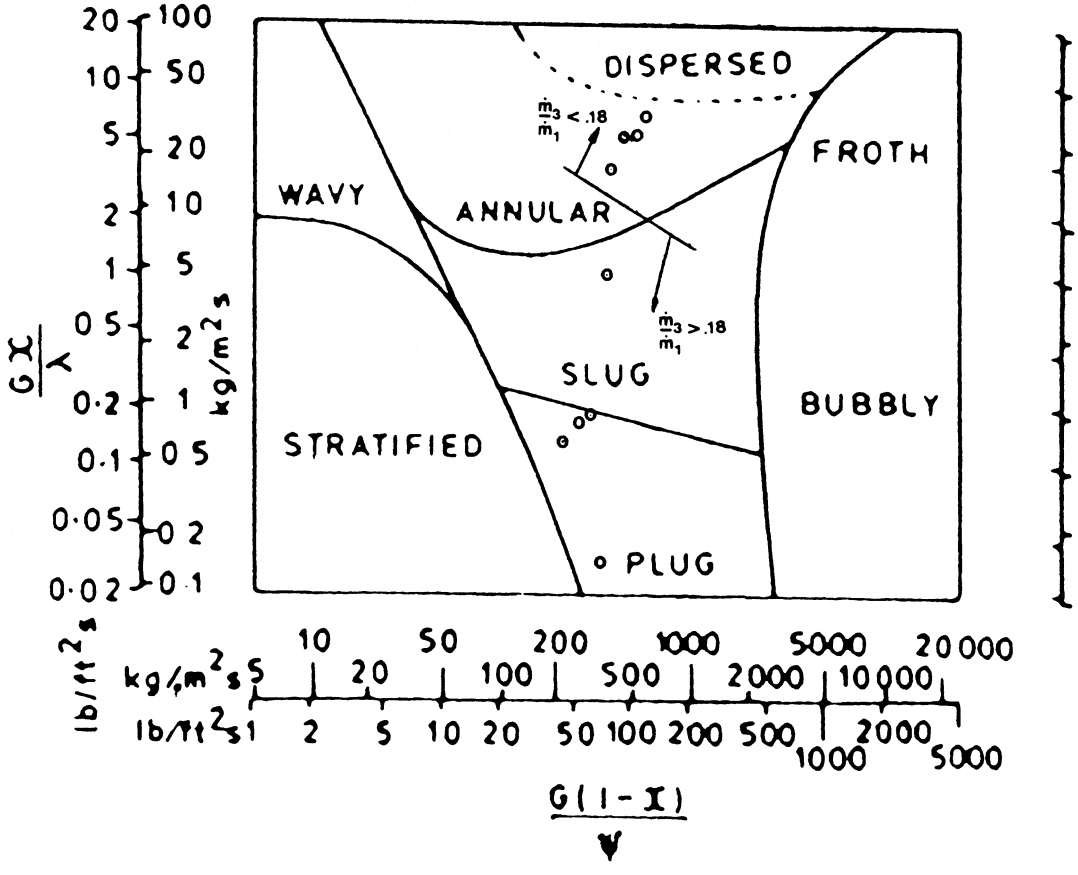

Figure 4.23 Run Flow Conditions Plotted on Baker's Map (G_1 = 600 kg/m²s, x_1 = 4.6%)

$$\rho_h = \frac{\rho_g \rho_\ell}{x\ \rho_\ell + (1 - x)\rho_g} \tag{4.12}$$

and

$$u_h = \frac{G}{\rho_h} \tag{4.13}$$

The homogeneous momentum correction factor is represetned by $k_{(1-2)h}$.

If the momentum carried by each phase is considered separately, the two phase separated flow equation corresponding to equation 4.7 is given by

$$(\Delta P_{2-1})_j = k_{(1-2)s}\left[\left(\frac{G_1^2 x_1^2}{\rho_g a_1} + \frac{G_1^2(1 - x_1)^2}{\rho_\ell(1 - a_1)}\right) - \left(\frac{G_2^2 x_2^2}{\rho_g a_2} + \frac{G_2^2(1 - x_2)^2}{\rho_\ell(1 - a_2)}\right)\right] \tag{4.14}$$

where $k_{(1-2)s}$ is the separated flow momentum correction factor.

Figure 4.24 shows the homogenous momentum correction factor ($k_{(1-2)h}$) plotted against the branch flow split for an inlet quality of 2.1% at 3 values of inlet mass flux. Most notable is the sudden increase in the correction factor in the range of flow split associated with the onset of complete phase separation. This is a result of drastic changes occurring in the run flow conditions due to flow regime transition from annular to slug flow (see Section 4.4). The void fraction assumed in the homogeneous formulation is a smooth function of quality and cannot account for this sudden change.

Figure 4.25 shows a similar plot of $k_{(1-2)h}$ vs. flow split for a constant inlet mass flux and 3 values of inlet quality. The same general trends are present although the scatter of the data is more severe.

Saba and Lahey [10] suggested that the single phase momentum correction factor (k_{1-2}) be used to predict two-phase pressure changes with the homogeneous model. For the data presented herein, the single phase correction factor was always higher than the corresponding two phase value. Agreement is approached for higher quality and high flow split conditions (see Figure 4.25). Fouda and Rhodes [15] suggested that a constant value of

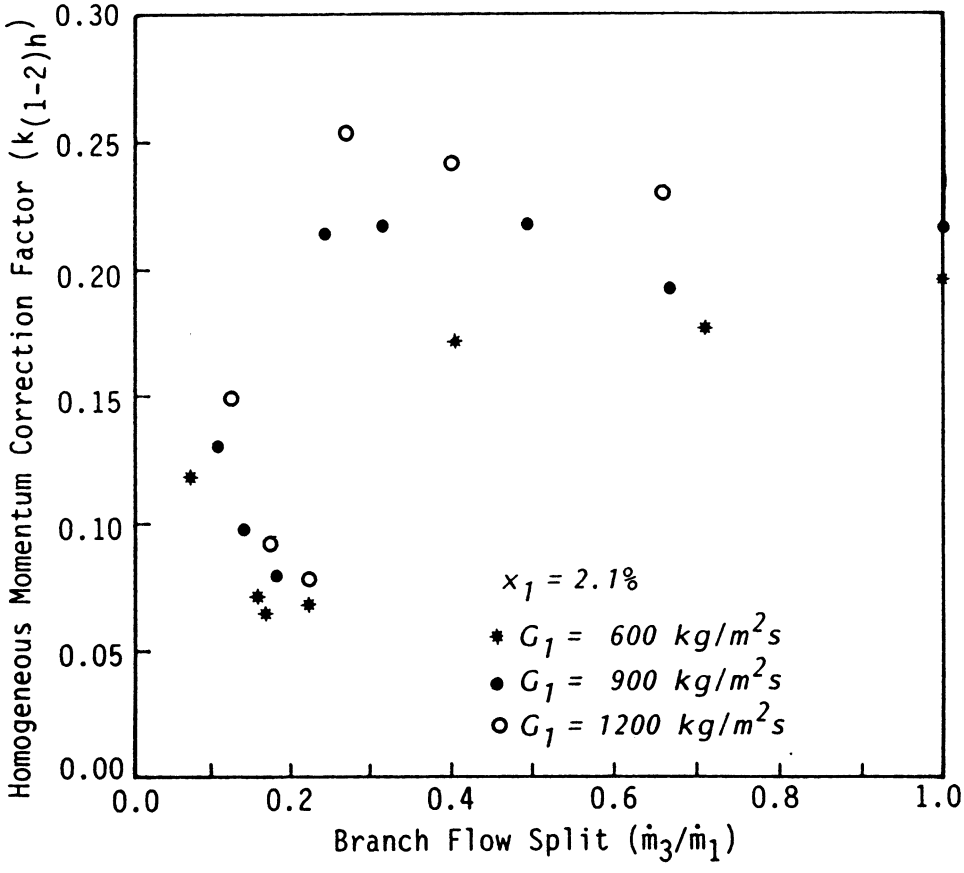

Figure 4.24 Homogeneous Momentum Correction Factor vs. Flow Split, Effect of Inlet Mass Flux (x_1 = 2.1%)

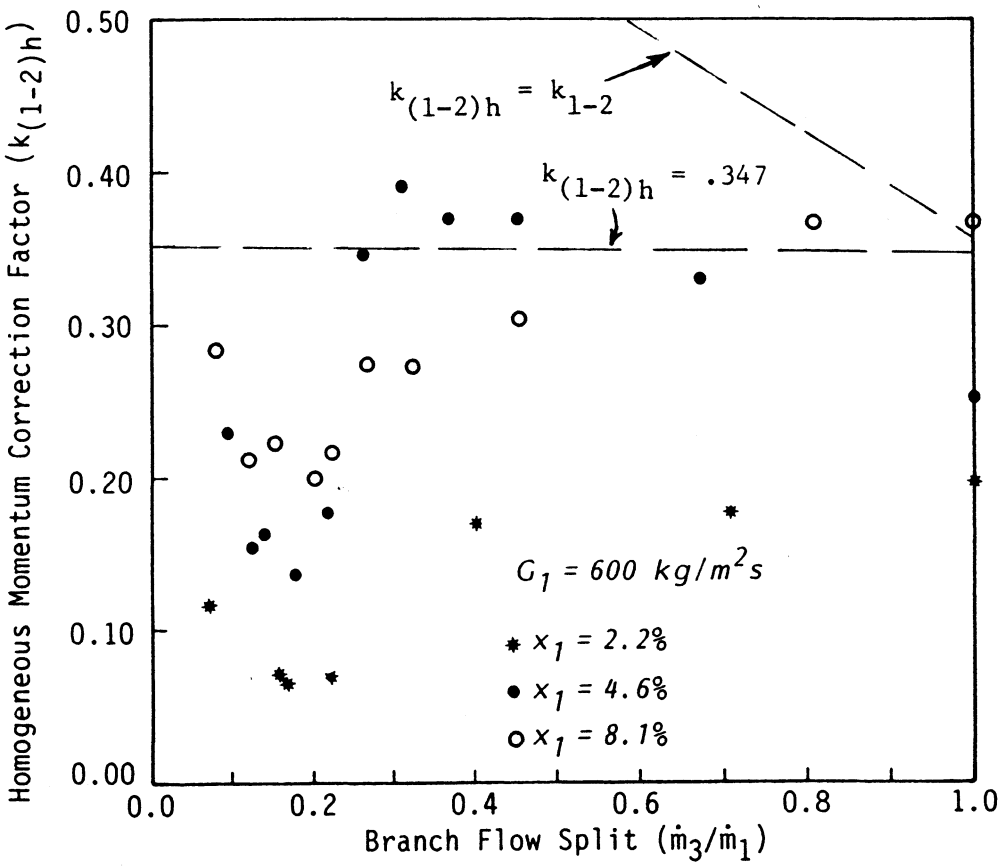

Figure 4.25 Homogeneous Momentum Correction Factor vs. Flow Split, Effect of Inlet Quality (G_1 = 600 kg/m²s)

0.347 be used for $k_{(1-2)h}$. Figure 4.25 shows good agreement for higher quality inlet flows and flow splits above that associated with total separation.

When the constant inlet quality data from figure 4.24 is used to determine the separated flow momentum correction factor ($k_{(1-2)s}$) the results are as shown in Figure 4.26. The momentum change associated with the flow regime transition at total separation can be accounted for through the measured void fraction in equation 4.14. As a result, the sudden change in the momentum correction factor in this range of flow split is not observed. The value of $k_{(1-2)s}$ appears to be distributed around 1.0 indicating that the branching flow carries little or no component of axial momentum.

Figure 4.27 shows the effect of inlet quality on the separated flow momentum correction factor. These results show similar trends to those presented in the previous figure although the scatter is more severe. Since this data was collected for higher quality flows, the corresponding void fraction measurements are also higher. The error associated with the liquid volume fraction $(1-\alpha)$ becomes large as α increases. It is expected that this contributes significantly to data scatter particularly at low flow splits.

St. Pierre et al. [6] reported that the separated flow momentum correction factor for annular inlet flows could be approximated by the correction factor determined from single phase air experiments. These are similar to the single phase water results presented in section 4.3.1. Fouda and Rhodes [15] suggested a constant value of 0.533 be used for $k_{(1-2)s}$. These results are generally lower than those from the present work. Both these investigations were carried out with branch to inlet diameter ratios less than 1.0 and the void fractions used were determined from correlations rather than experimental measurements. These factors may account for the discrepancies in the results.

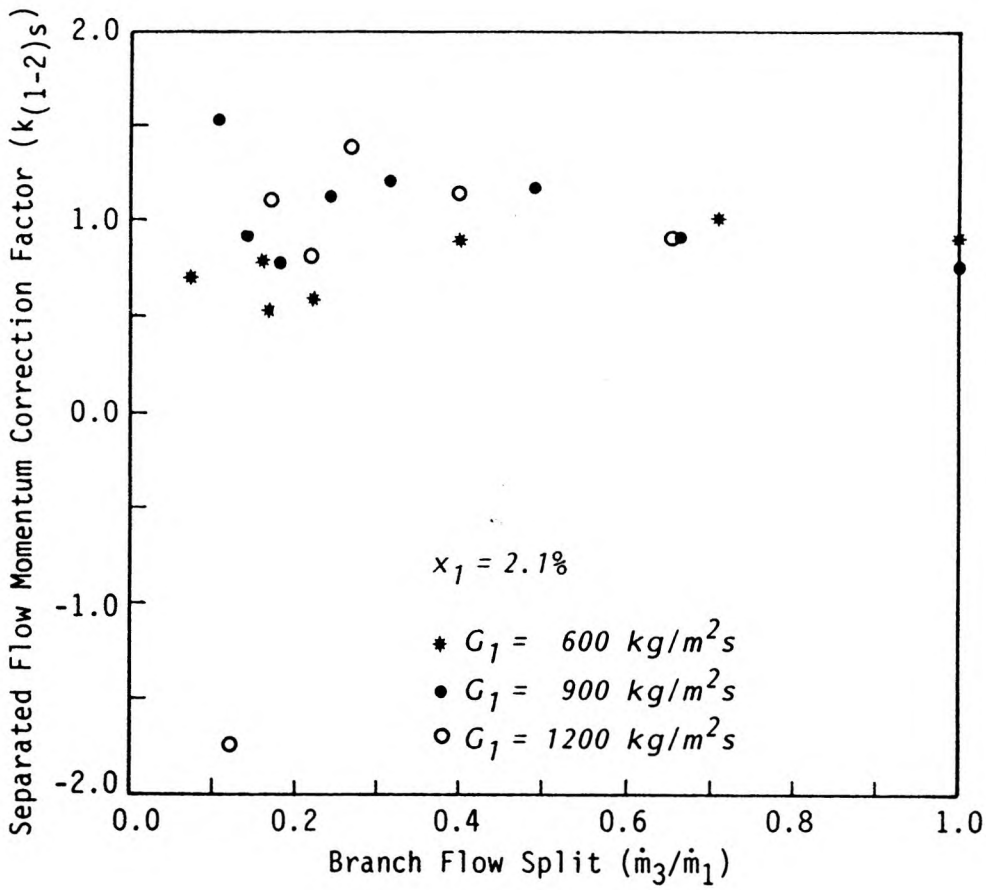

Figure 4.26 Separated Flow Momentum Correction Factor vs. Flow Split, Effect of Inlet Mass Flux (x_1 = 2.1%)

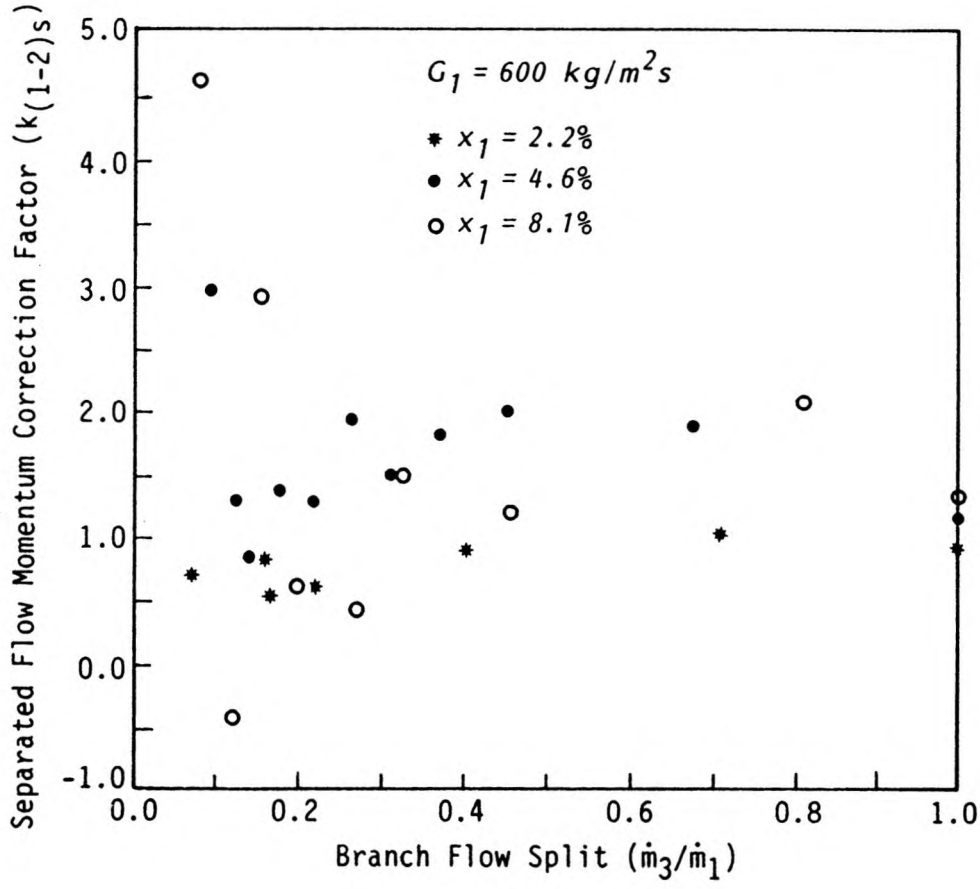

Figure 4.27 Separated Flow Momentum Correction Factor vs. Flow Split, Effect of Inlet Quality (G_1 = 600 kg/m^{2}s)

4.4.2 Two-Phase Radial Pressure Drop

The radial pressure drop through the branch of the tee was modelled as proposed by Saba and Lahey [10]. The pressure change is considered in terms of its reversible and irreversible components. Saba et al. [12] have shown that the reversible pressure change may be written from the two-phase Bernoulli equation as

$$(\Delta P_{1-3})_{j(rev)} = \frac{\rho_{h3}}{2}\left[\frac{G_3^2}{\rho_3'''^2} - \frac{G_1^2}{\rho_1'''^2}\right] \tag{4.15}$$

where the energy weighted density (ρ''') is given by

$$\frac{1}{\rho'''^2} = \left[\frac{x^3}{\alpha^2\rho_g^2} + \frac{(1-x)^3}{(1-\alpha)^2\rho_\ell^2}\right] \tag{4.16}$$

For a homogeneous flow assumption, the energy weighted density (ρ''') reduces to the homogeneous density (ρ_h) and equation 4.15 becomes

$$(\Delta P_{1-3})_{j(rev)} = \frac{\rho_{h3}}{2}\left[\left(\frac{G_3}{\rho_{h3}}\right)^2 - \left(\frac{G_1}{\rho_{h1}}\right)^2\right] \tag{4.17}$$

The irreversible pressure change is modelled in terms of the single phase pressure drop in the form

$$(\Delta P_{1-3})_{j(irrev)} = k_{1-3}\frac{G_1^2}{2\rho_\ell}\Phi_{h,s} \tag{4.18}$$

where k_{1-3} is the single phase loss coefficient and Φ represents a two-phase multiplier. Subscripts s and h refer to the separated and homogeneous multipliers. Combining equations 4.15 and 4.18 or 4.17 and 4.18 yields the separated flow and homogeneous models respectively.

Figure 4.28 shows the homogeneous multiplier plotted against the flow split for an inlet mass flux of 600 kg/m^{2}s and varying inlet quality. All plots show similar trends with ϕ_h having a very steep negative slope at low flow splits. Beyond total separation ($\dot{m}_3/\dot{m}_1 > 0.3$) the irreversible losses are seen to increase, ultimately leveling off for higher flow splits. In

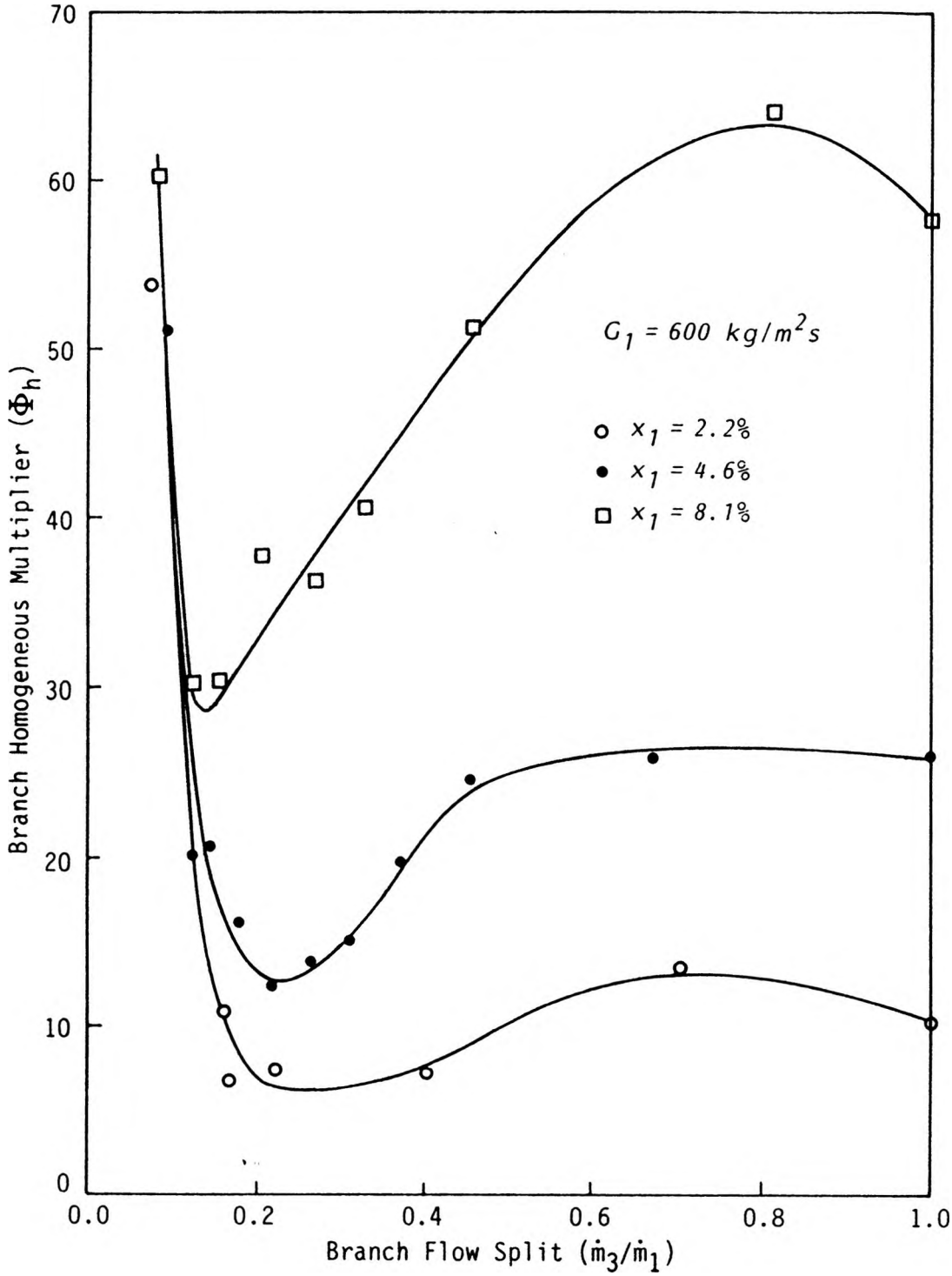

Figure 4.28 Homogeneous Two-Phase Multiplier vs. Flow Split,

Effect of Inlet Quality (G_1 = 600 kg/m^{2}s)

this range, the model indicates higher irreversible losses for increased inlet quality. This is expected since the multiplier (Φ_h) does not act on the true inlet dynamic pressure, but that associated with single phase water flow at the same mass flux. The actual inlet dynamic pressure will depend on the flow quality.

Figure 4.29 shows the branch homogeneous multiplier plotted against branch flow split for an inlet quality of 2.1% and varying inlet mass flux. The data trends are similar to those presented in the previous figure. For the range of data tested, the effects of varying the inlet mass flux are less significant than those associated with inlet quality variations.

Saba and Lahey [10,12] suggested that a two phase multiplier be used in the form

$$\Phi = \frac{\rho_\ell}{\rho'} \tag{4.19}$$

where ρ' is the momentum weighted density given by

$$\frac{1}{\rho'} = \left[\frac{x^2}{\alpha \rho_g} + \frac{(1-x)^2}{(1-\alpha)\rho_\ell} \right] \tag{4.20}$$

For a homogeneous assumption the momentum weighted density reduces to the homogeneous density (ρ_h) and eqn. 4.18 becomes

$$\Phi_h = \frac{\rho_\ell}{\rho_h} \tag{4.21}$$

where ρ_h is given by eqn. 4.12. This formulation yields a multiplier that is independent of flow split and is generally higher than that determined in the present work (see Figure 4.29).

When the constant inlet mass flux data of Figure 4.28 is replotted based on the separated flow model, the results are as shown in Figure 4.30. The separated flow multiplier is significantly lower than the corresponding homogeneous multiplier at low flow splits. This is a result of the separated flow model determining the reversible pressure change more precisely through the measured void fraction in equations 4.15 and 4.16. At higher flow splits the two models indicate similar multipliers since the reversible pressure changes from

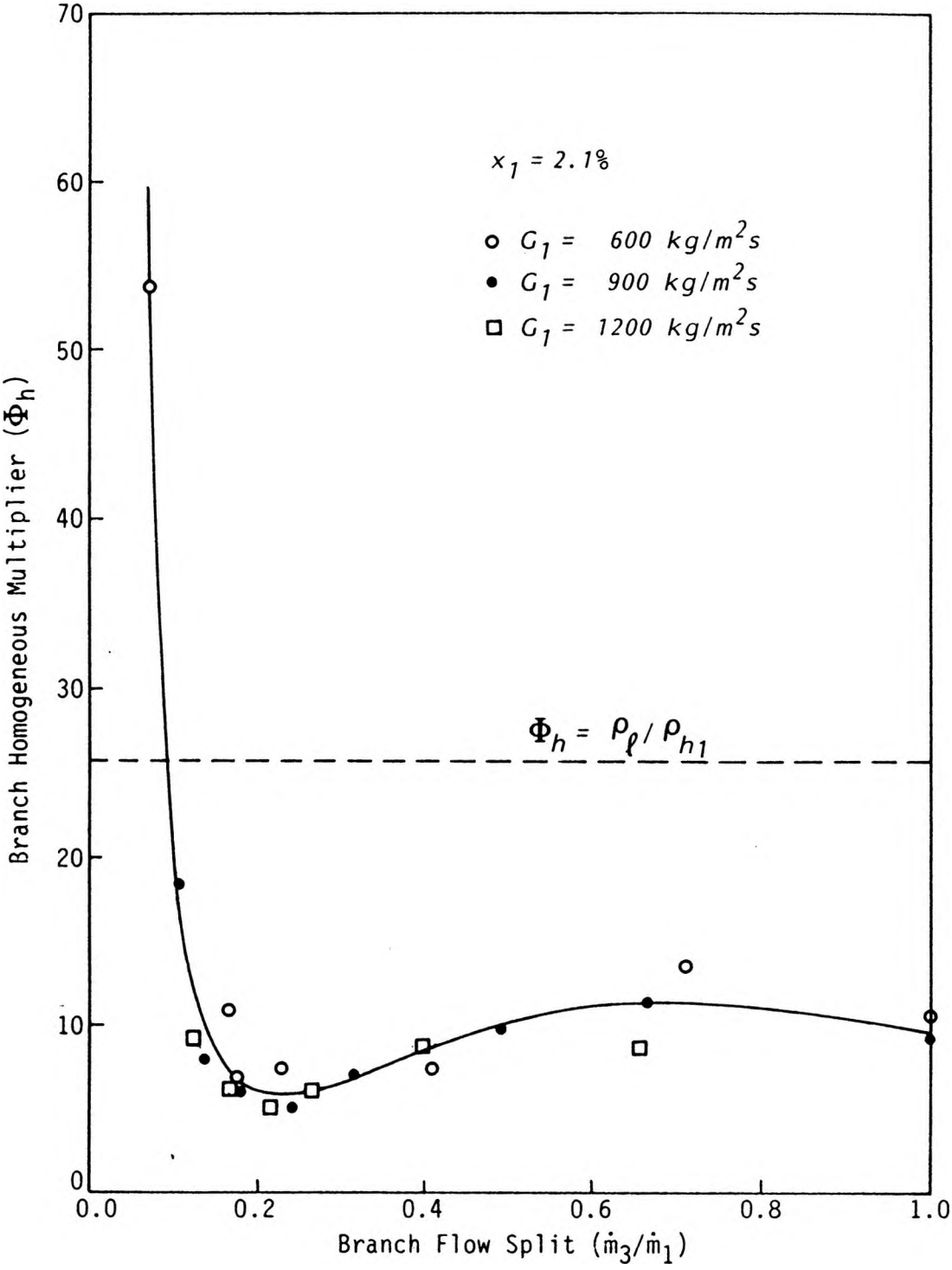

Figure 4.29 Homogeneous Two-Phase Multiplier vs. Flow Split,

Effect of Inlet Mass Flux (x_1 = 2.1%)

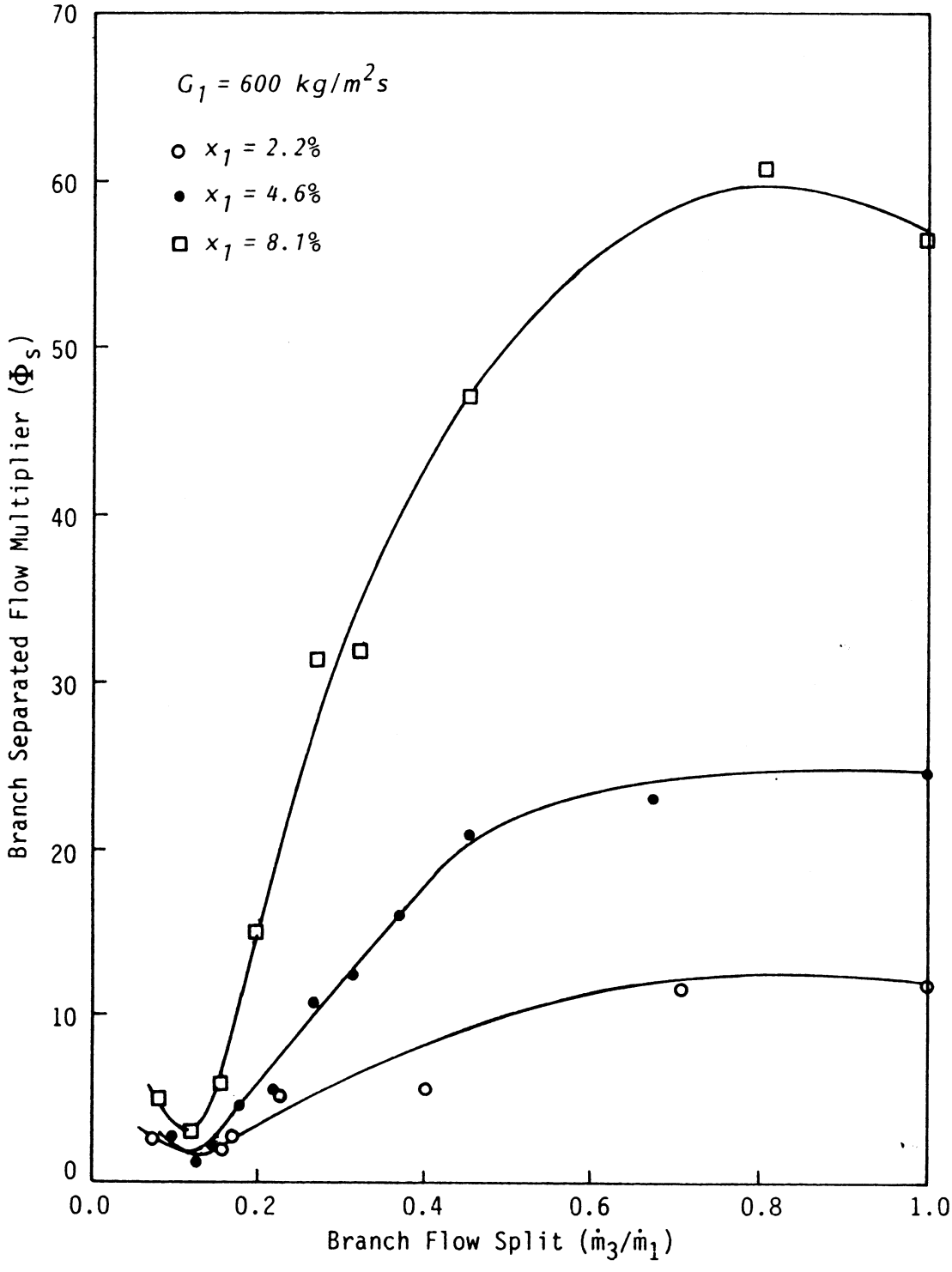

Figure 4.30 Separated Flow Two-Phase Multiplier vs. Flow Split,

Effect of Inlet Quality (G_1 = 600 kg/m^{2}s)

both equations 4.15 and 4.17 tend to zero as the flow split approaches unity and the irreversible component is identical for both models.

Figure 4.31 shows Φ_s plotted against flow split for a constant inlet quality of 2.1% and 3 values of inlet mass flux. Again, the data trends are similar to those in the previous figure. The effects of inlet mass flux variations are seen to be less significant than those due to inlet quality variations when modelled in this manner.

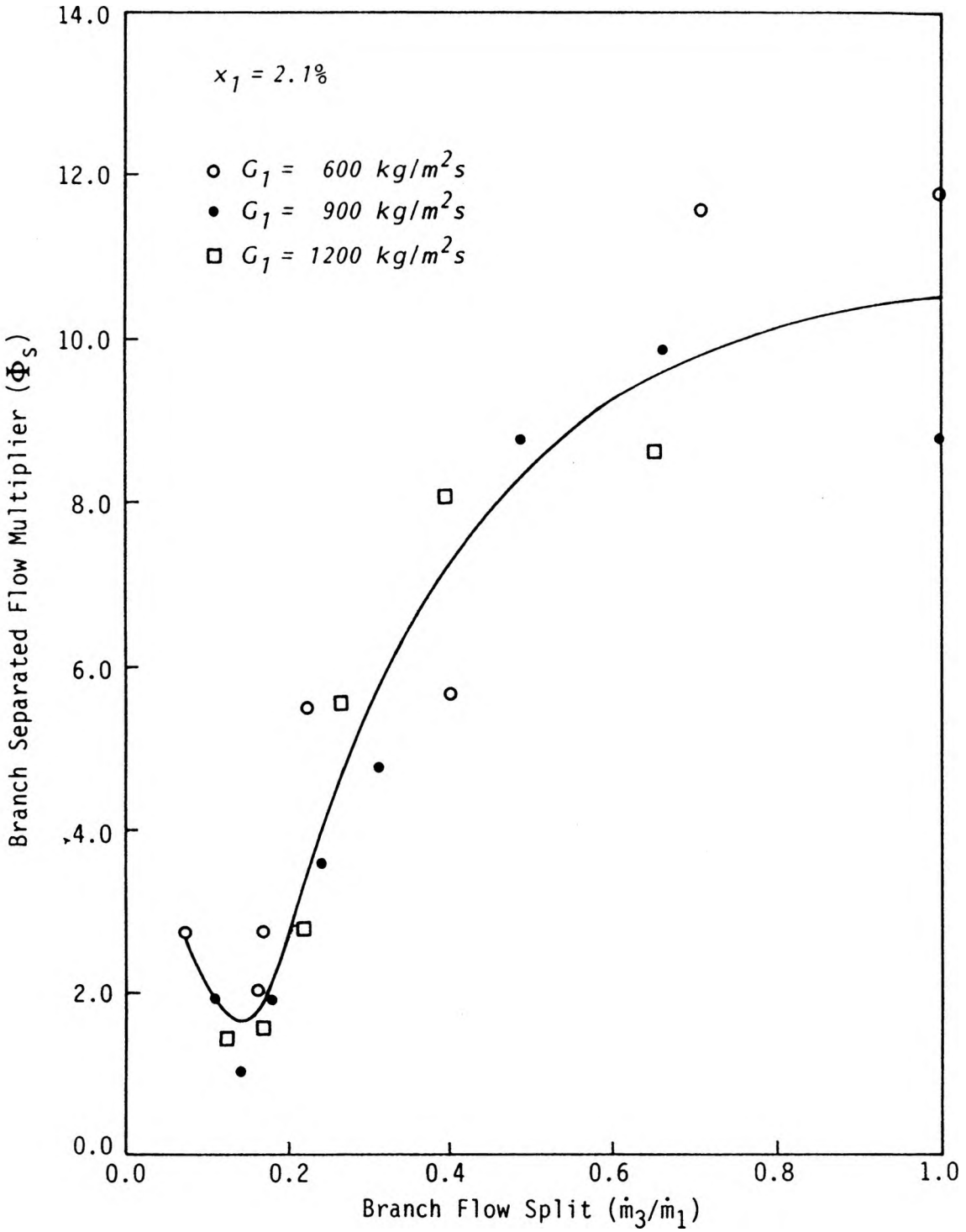

Figure 4.31 Separated Flow Two-Phase Multiplier vs. Flow Split, Effect of Inlet Mass Flux (x_1 = 2.1%)

CHAPTER 5

CONCLUSIONS AND RECOMMENDATIONS

The characteristics of dividing two-phase flow in a horizontal tee junction have been investigated. The results obtained form a significant portion of the data base associated with the separation phenomena, particularly for steam water systems. This experimental program is the first to include measurements of the associated void fraction distributions.

For the annular flow conditions considered herein, separation effects were seen to be severe with the gas phase preferentially entering the branch. An assumption of complete separation closely approximated the measured data when more than 40% of the inlet flow was removed through the branch. The flow split at which complete separation can be assumed was associated with a flow regime transition occurring in the run of the tee. Below 40% removal, the degree of separation is strongly dependent on the flow split, inlet quality and, to a lesser extent, the inlet mass flux.

The flow through the run of the tee experiences a pressure rise as predicted by an axial momentum balance at the junction. When reduced in terms of the separated flow momentum equation (4.14), the data suggests that the branching flow carries little or no axial component of momentum. The pressure change through the branch was modelled in terms of a reversible and an irreversible component. Both separated and homogeneous flow assumptions yield irreversible loss coefficients dependent on the branch flow split and the inlet quality.

There is considerable scope for future work related to the separation phenomena in dividing two-phase flow. Immediate extensions of the present work should include additional experiments using smaller branch to inlet diameter ratios. Previous investigations have

shown that a reduction in branch diameter results in more severe phase separation [6,11]. The effects of inlet flow regime can be investigated using test sections with larger inlet diameters. This would allow measurable flow rates of steam and water to be delivered to the mixer yielding stratified and intermittent flows in the inlet section. To complement the data obtained for annular flow, measurements of the angular distribution of liquid film thickness in the inlet section may also be made by ultrasonic or resistance probe techniques. This information will aid the development of a comprehensive generalized model for two-phase flow in branching conduits.

REFERENCES

1. Alves, G.E., (1954), "Cocurrent liquid-gas flow in a pipeline contactor", Chem. Eng. Prog., 50(9), 449-456.

2. Taitel, Y. and Dukler, A.E., (1976), "A model for predicting flow regime transitions in horizontal and near horizontal gas liquid flow", AIChEJ, 22(1), 47-55.

3. Baker, O., (1954), Oil and Gas J., 53, 185.

4. Collier, J.G., (1972), "Convective boiling and condensation", McGraw-Hill.

5. Mandhane, J.M., Gregory, G.A. and Aziz, K., (1974), "A flow pattern map for gas-liquid flow in horizontal pipes", Int. J. Multiphase Flow, 1, 537-553.

6. St. Pierre, C.C. and Glastonbury, A., (1972), "Two-phase flow distribution and pressure changes for horizontal tee junctions", AERE-R7131.

7. Azzopardi, B.J. and Whalley, P.B., (1982), "The effect of flow patterns on two-phase flow in a tee junction", Int. J. Multiphase Flow, 8, 3, 491-507.

8. Henry, J.A.R., (1981), "Dividing annular flow in a horizontal tee", Int. J. Multiphase Flow, 7, 343-355.

9. Honan, T.J. and Lahey, R.T., Jr., (1981), "The measurement of phase separation in wyes and tees", Nuclear Engineering and Design, 64, 93-102.

10. Saba, N. and Lahey, R.T., Jr., (1984), "The analysis of phase separation phenomena in branching conduits", Int. J. Multiphase Flow, 10, 1-20.

11. Azzopardi, B.J. and Freeman-Bell, G., (1983), "The effect of side arm diameter on the two phase flow split at a 'T' junction", AERE-M3290.

12. Whalley, P.B. and Azzopardi, B.J., (1980), "Two-phase flow in a 'T' junction", Basic Mechanisms in Two-Phase Flow, ASME Winter Annual Meeting, Chicago.

13. Saba, N. and Lahey, R.T., Jr. (1982), "Phase separation phenomena in branching conduits", NUREG/CR-2590.

14. Fouda, A.E., (1975), "Two-phase flow behaviour in manifolds and networks", Ph.D. Thesis, University of Waterloo, Dept. of Chem. Eng.

15. Fouda, A.E. and Rhodes, E., (1974), "Two-phase annular flow stream division in a simple tee", Trans. Inst. Chem. Engrs., 52, 354-360.

16. Hasan, A.T.M.R., (1979), "Low pressure boiling in straight tubes and a bend", Ph.D. Thesis, University of Waterloo, Dept. of Chem. Eng.

17. Shoukri, M., (1980), "The effect of heat addition on the pressure drop in two-phase flow systems", Report for CEA project 000G104.

18. McNown, J.S., (1954), "Mechanics of manifold flow", Trans. ASCE, 2714, 119, 1103-1142.

19. Chan, A.M.C. and Banerjee, S., (1981), "Design aspects of gamma densitometers for void fraction measurements in small scale two-phase flows", Nuclear Instruments and Methods, 190, 135-148.

APPENDIX A

CALIBRATION DATA

A.1 Orifice Plate Calibration

The orifice meter calibration was based on the orifice equation:

$$\dot{m} = \frac{A_2 F_a C Y}{\sqrt{1-\beta^4}} [2 \rho_1 (P_1 - P_2)]^{1/2} \qquad \text{(A-1)}$$

where

A_2	=	orifice cross sectional area	[m^2]
F_a	=	plate thermal expansion factor	[ratio]
C	=	discharge coefficient	[ratio]
β	=	ratio of bore to pipe diameters	[ratio]
Y	=	gas expansion factor	[ratio]
ρ_1	=	upstream steam density	[kg/m^3]
P_1	=	upstream flange pressure	[N/m^2]
P_2	=	downstream flange pressure	[N/m^2]

The gas expansion factor is determined from the empirical equation

$$Y = 1 - [0.41 + 0.35 \beta^4] \frac{(P_1 - P_2)}{\gamma P_1} \qquad \text{(A-2)}$$

where

γ = specific heat ratio for steam

It was experimentally observed that for any regulated upstream pressure the upstream temperature remained constant and was reproducible. The orifice meter was calibrated on line for regulated upstream pressures of 200 and 275 kPa by direct weighing of

condensate. The discharge coefficients (C), calculated using the calibration data with the aid of equations (A.1) and (A.2), are shown in Figure A.1. The resulting least squares equations for discharge coefficient as a function of Reynolds number are:

For $P_1 = 200$ kPa

$$C = .6575 + 2.18\times10^{-7}\,Re - 1.73 \times 10^{-12}\,Re^2 \qquad (A.3)$$

and for $P_1 = 275$ kPa

$$C = .7372 - 4.0\times10^{-7}\,Re + 6.73\times10^{-13}\,Re^2 \qquad (A.4)$$

A.2 Transducer Calibration

All DP 15 series transducers were calibrated off line by applying pressure with an air over mercury manometer. The applied pressure was measured using a calibrated Barocel Pressure Sensor (Type 590D-10000T- 2Q1-VIX-40) and Electronic Manometer (Type 1400-9AX) manufactured by Datametrix. The sensor has a range of 10,000 Torr (1.3 MPa) and is accurate to $\pm$(0.05% of reading +0.001% of full scale). The calibration data for transducers DP15-36, DP15-38 and DP15-46 are shown in Figures A.2, A.3 and A.4 respectively.

The calibration pressures for the DP103-20 transducer were applied and measured with an air over oil inclined manometer. Those for transducer DP103-28 were applied and measured with a water over CCl_4 manometer. Calibration results are shown in Figures A.5 and A.6.

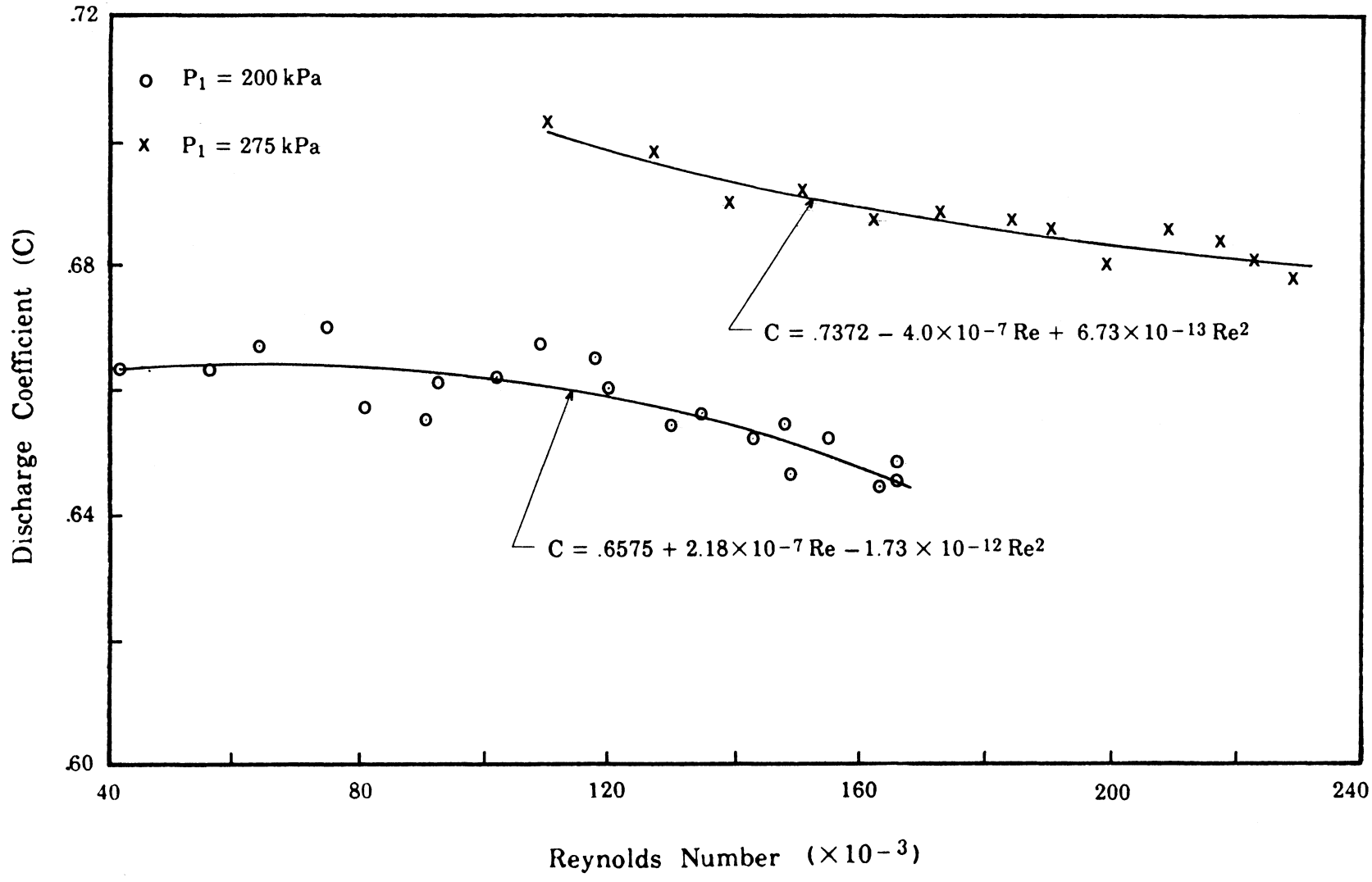

Figure A.1 Calibration Results for the Orifice Meter

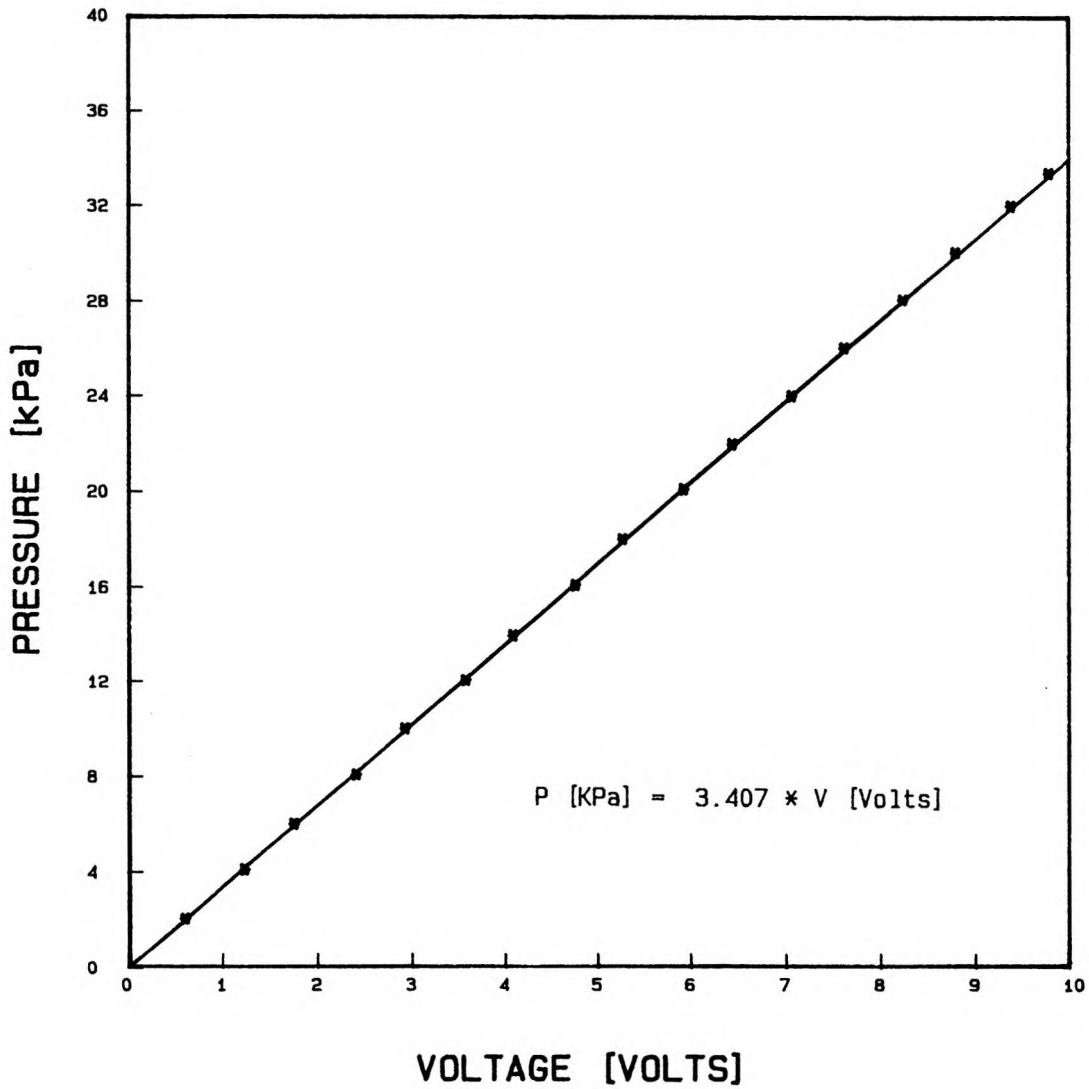

Figure A.2 Calibration Results for Pressure Transducer DP15-36

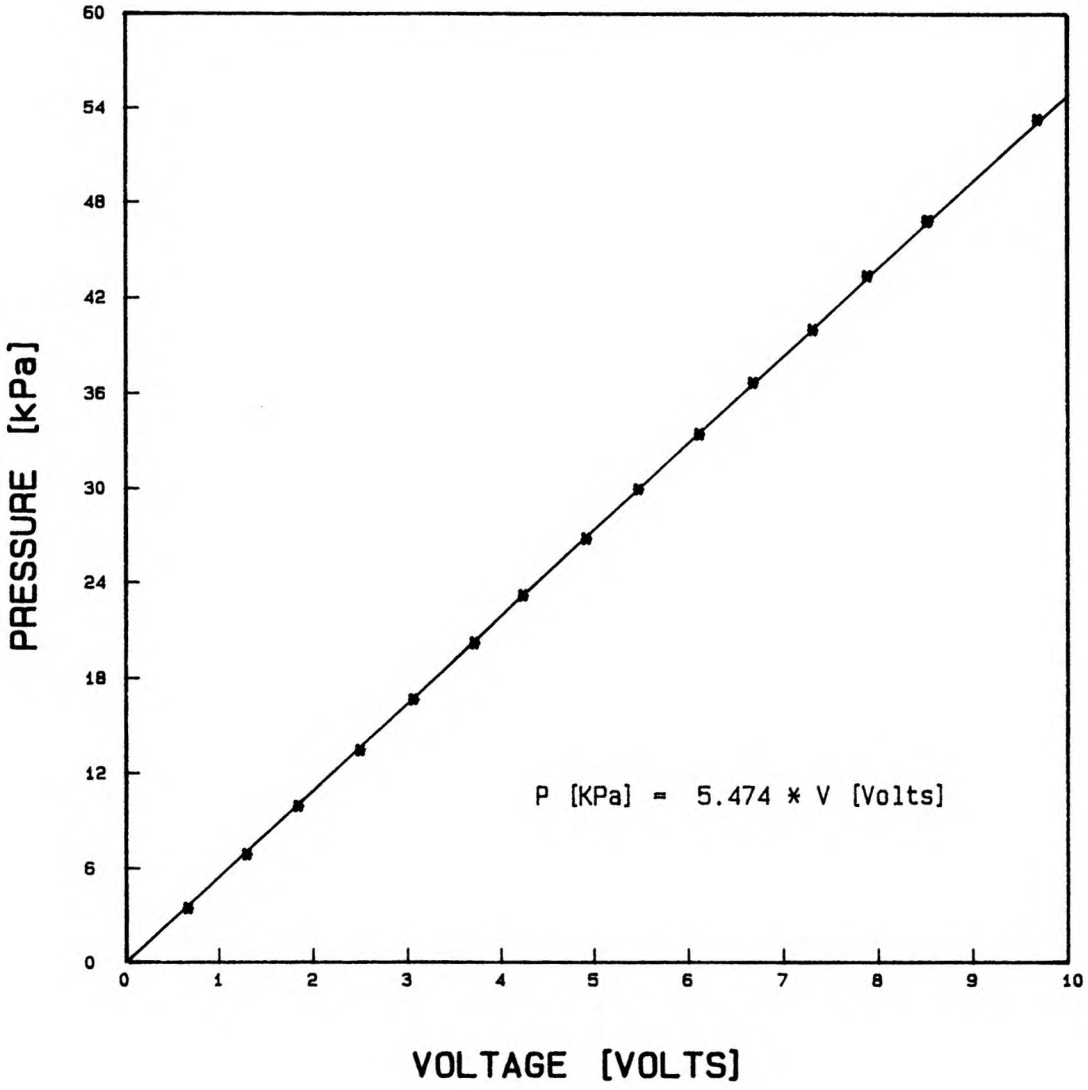

Figure A.3 Calibration Results for Pressure Transducer DP15-38

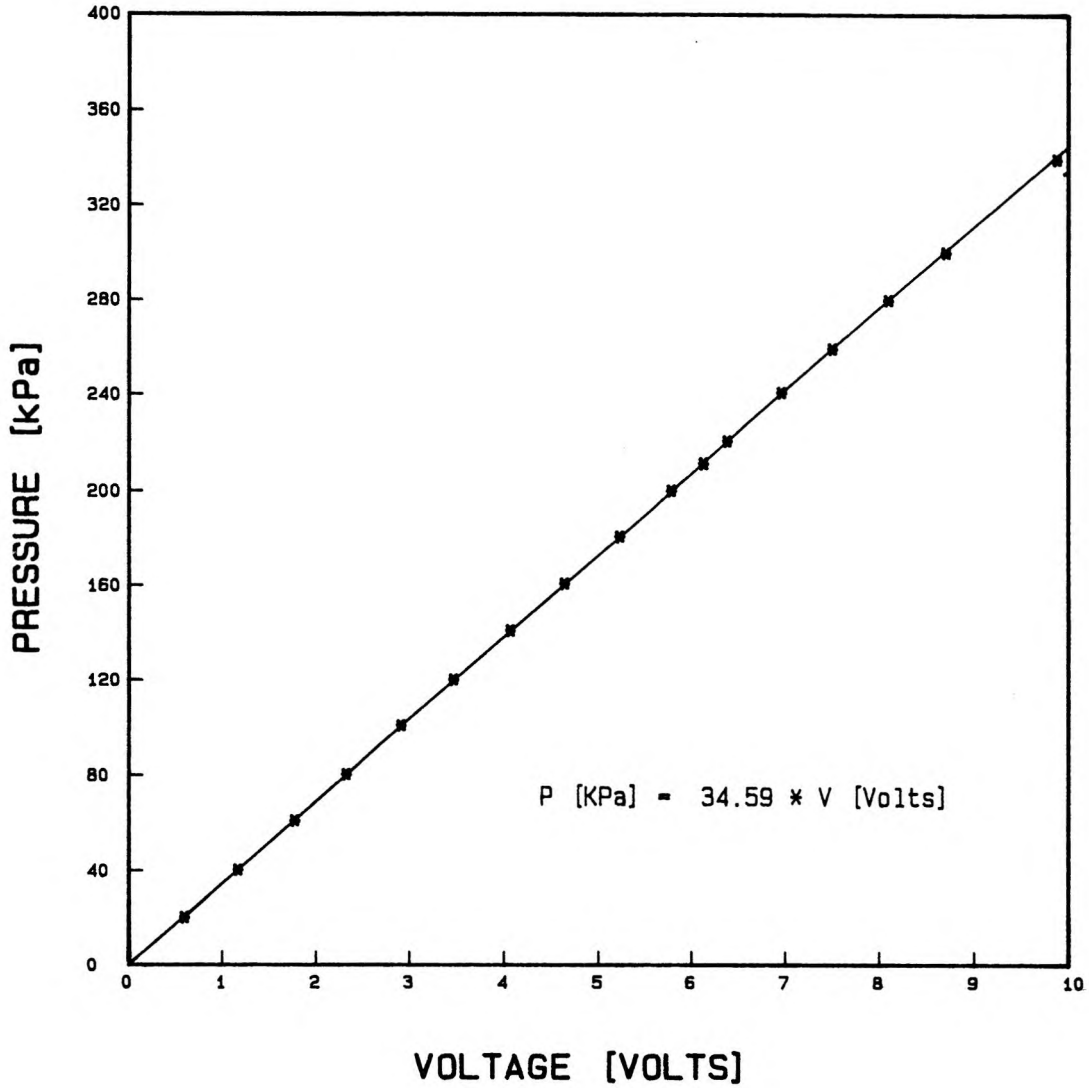

Figure A.4 Calibration Results for Pressure Transducer DP15-46

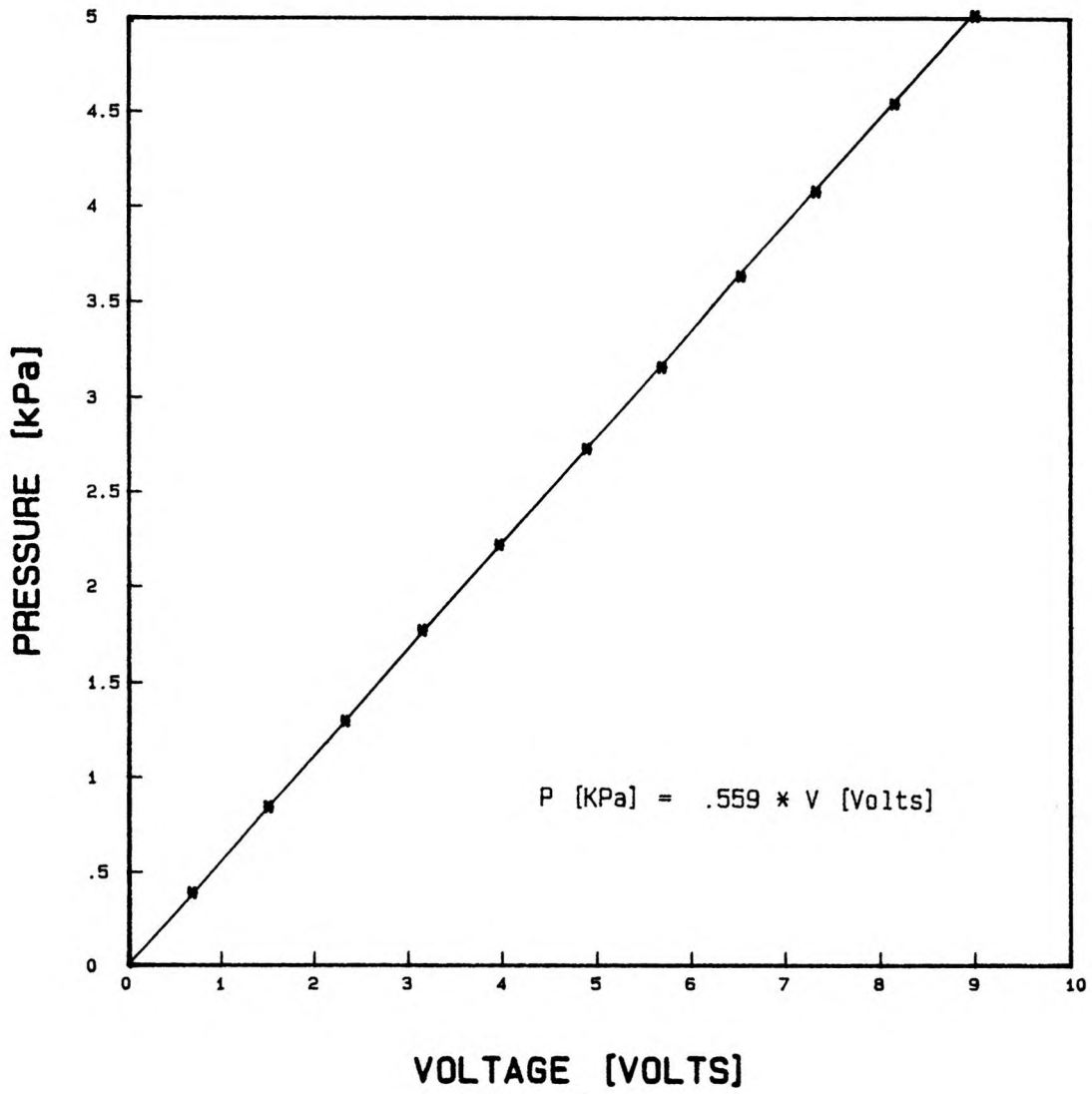

Figure A.5 Calibration Results for Pressure Transducer DP103-20

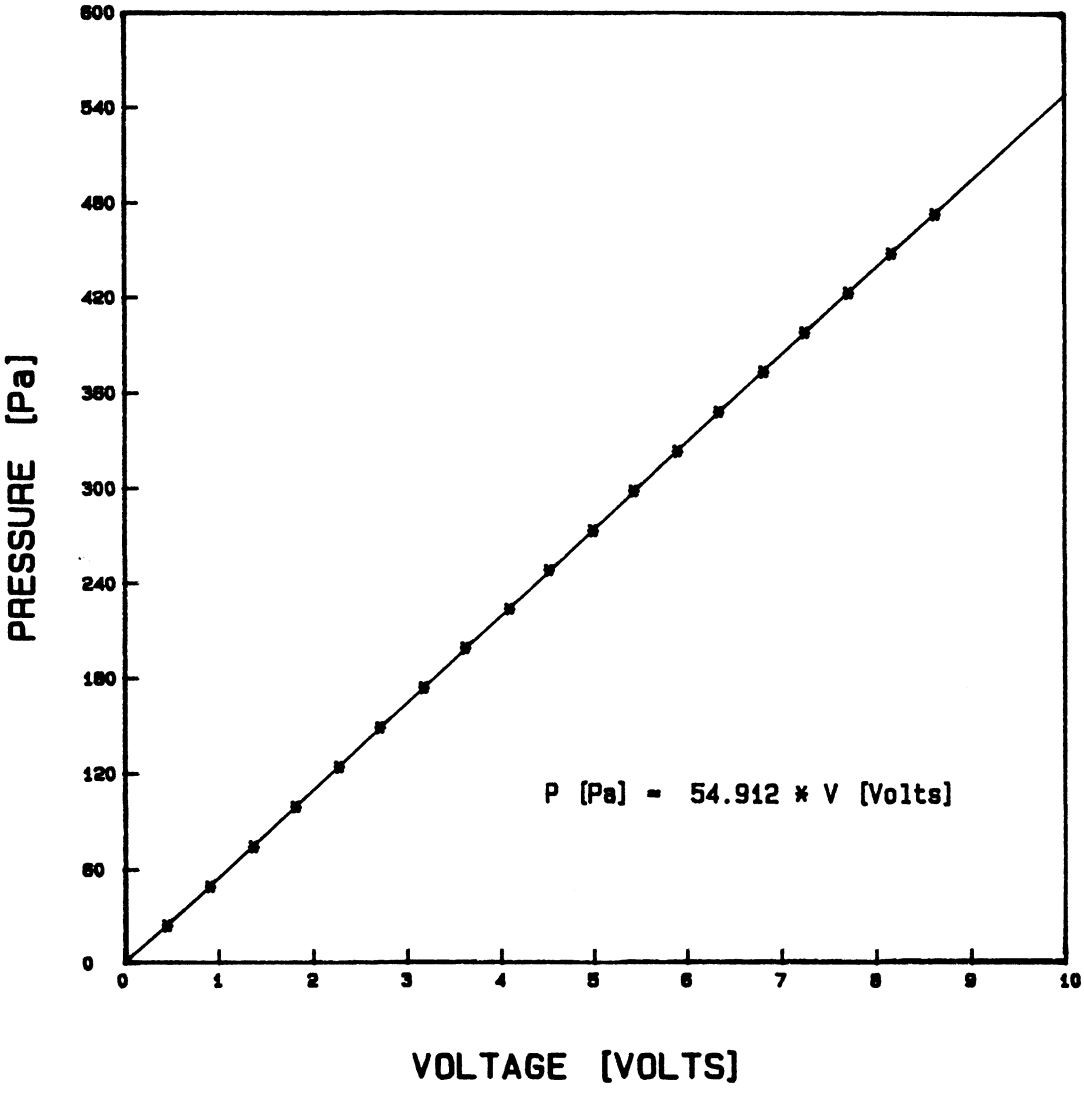

Figure A.6 Calibration Results for Pressure Transducer DP103-28

APPENDIX B

GAMMA DENSITOMETER

B.1 Operating Principle

Radiation attenuation is a widely used, non intrusive method of void fraction and phase distribution measurements in two-phase flows. The technique utilizes the exponential decay of radiation intensity as it passes through matter. The attenuated flux of a well collimated gamma beam is related to the incident flux by

$$N = N_0 e^{-\mu x} \tag{B.1}$$

where N is the emerging flux, N_0 is the incident flux, μ is the material absorption coefficient and x is the beam path length through the absorber.

Consider a test section of width L and wall thickness t with an absorption coefficient of μ_w. If the test section is completely filled with vapour ($\alpha = 1$) or liquid ($\alpha = 0$) equation B.1 may be written

$$N_{(\alpha = 1)} = N_0 e^{-2\mu_w t} e^{-\mu_g L} \tag{B.2}$$

or

$$N_{(\alpha = 0)} = N_0 e^{-2\mu_w t} e^{-\mu_\ell L} \tag{B.3}$$

respectively, where μ_g and μ_ℓ are the gas and liquid absorption coefficients. If the test section is filled with a mixture of the two phases where the total volume occupied by gas divided by the test section volume is denoted as α (the void fraction) equation B.1 becomes

$$N_{(\alpha)} = N_0 e^{-2\mu_w t} e^{-\alpha\mu_g L} e^{-(1-\alpha)\mu_\ell L} \tag{B.4}$$

From equations B.2 and B.3

$$\frac{N_{(\alpha=0)}}{N_{(\alpha=1)}} = e^{(\mu_g - \mu_\ell) L} \tag{B.5}$$

and from B.2 and B.4

$$\frac{N_{(\alpha)}}{N_{(\alpha=1)}} = e^{(\mu_g - \mu_\ell)(1-\alpha)L} \tag{B.6}$$

In general, the exponents in equations B.5 and B.6 are small and these equations may be approximated by the first two terms of an exponential series expansion, i.e.

$$\frac{N_{(\alpha=0)}}{N_{(\alpha=1)}} \simeq 1 + (\mu_g - \mu_\ell) L \tag{B.7}$$

and

$$\frac{N_{(\alpha)}}{N_{(\alpha=1)}} \simeq 1 + (\mu_g - \mu_\ell)(1 - \alpha) L \tag{B.8}$$

Combining equations B.7 and B.8 yields the linear interpolation equation

$$\alpha \simeq \frac{N_\alpha - N_{(\alpha=0)}}{N_{(\alpha=1)} - N_{(\alpha=0)}} \tag{B.9}$$

B.2 Densitometer Design

The procedure outlined by Chan et al. [19] was followed for the design of the gamma densitometer. The authors summarized the design procedure as follows:

1. specify the test section geometry and material;
2. choose the radioactive isotope (or gamma ray energy) with reference to (1);
3. calculate the required source strength;
4. estimate the shielding requirements;
5. choose the scintillator and counting system with reference to (3).

In general, the test section geometry and material are determined from the experimental requirements. For the experiments presented herein the test section was of 31.75 mm O.D. and 25.65 mm I.D. 304 stainless steel tubing.

With the test section specified, the particular source to be used is selected based on the following considerations:

1. transmission ratio through the pipe walls;

2. sensitivity to water content;

3. gamma source half-life;

4. emission ratio of the desired gammas;

5. cost and availability.

Based on constraints 5 and 4 and previous experience, Cesium-137 and Cobalt-57 were considered for this application. These have principal photon energies of 662 keV with an emission ratio of 85.1% and 122 keV with an emission ratio of 85.2% respectively. The half life of Cesium-137 is 30.1 years and that of Cobalt- 57 is 270.5 days.

The transmission ratio through the empty pipe can be estimated by using the mean beam path length through the tube walls and assuming a flat incident beam profile. From Figure B.1 the mean beam path length through the walls (L_w) for $0 \leq x \leq r_1$ is given by

$$\bar{L}_w = \frac{2}{r_1} \int_0^{r_1} \left[(r_2^2 - x^2)^{1/2} - (r_1^2 - x^2)^{1/2} \right] dx \qquad \text{(B.10)}$$

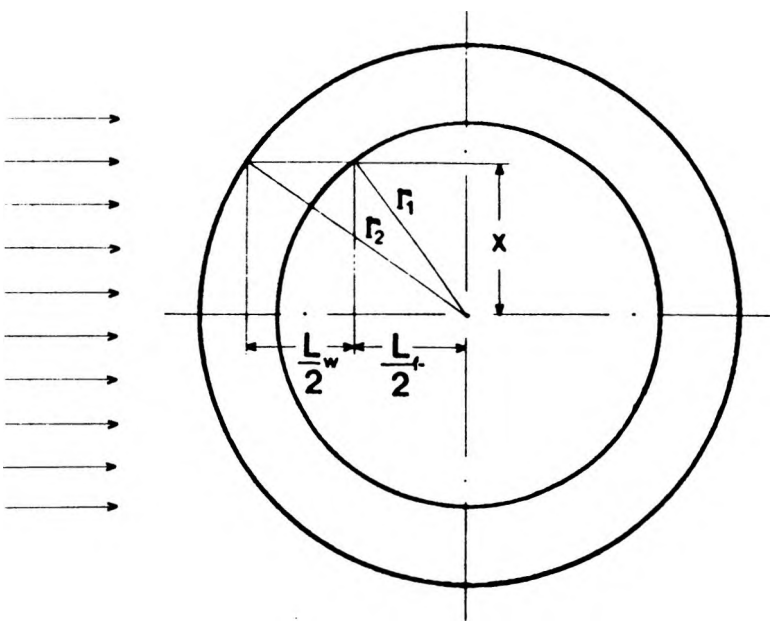

Figure B.1 Test Section Cross Section for Gamma Densitometer Design

Integrating B.10

$$\bar{L}_w = (r_2^2 - r_1^2)^{1/2} + \frac{r_2^2}{r_1} \mathrm{Sin}^{-1}\left(\frac{r_1}{r_2}\right) - r_1 \frac{\pi}{2} \tag{B.11}$$

For the present test section $r_1 = 12.827$ mm, $r_2 = 15.875$ mm and $L_w = 7.689$ mm. From equation B.1 the transmission ratio may be determined as;

$$\frac{N}{N_o} = e^{-\mu_w \bar{L}_w} \tag{B.12}$$

where μ_w is the attenuation coefficient of the test section material at the appropriate energy level. At 662 keV and 122 keV the pipe wall attenuation coefficient is $0.55\,cm^{-1}$ and $2.156\,cm^{-1}$ respectively. then, from eqn. B.12

$$\left(\frac{N}{N_o}\right)_{^{137}Cs} = e^{-(0.577)(0.7689)} = 0.6417$$

and

$$\left(\frac{N}{N_o}\right)_{^{57}Co} = e^{-(2.157)(0.7689)} = 0.1904$$

The gamma beam sensitivity to water content (S) may be defined as;

$$S = \frac{N_{(a=1)} - N_{(a=0)}}{(N_{(a=1)} + N_{(a=0)})/2} \tag{B.13}$$

The sensitivity may be estimated by again using the mean beam path length through the fluid and assuming a flat incident beam profile. The gamma attenuation coefficient for steam is close to zero and we can write

$$N_{(a=1)} \simeq N_o \tag{B.14}$$

From Figure B.1 the mean beam path length through the fluid (L_f) is given by

$$\bar{L}_f = \frac{2}{r_1} \int_o^{r_1} (r_1^2 - x^2)^{1/2} dx \tag{B.15}$$

Performing the integration

$$\bar{L}_f = \frac{r_1 \pi}{2} \tag{B.16}$$

For the present test section $r_1 = 12.827$ mm and $L_f = 20.149$ mm. The mass attenuation coefficient for water is $0.0858\,cm^{-1}$ and $0.157\,cm^{-1}$ at 662 keV and 122 keV respectively. From equations B.1, B.13 and B.14 we may write;

$$S_{^{137}Cs} = \frac{N_o - N_o e^{-0.0858\,(2.015)}}{[N_o + N_o e^{-0.0858\,(2.015)}]/2} = 0.1725$$

and

$$S_{^{57}Co} = \frac{N_o - N_o e^{-0.157\,(2.015)}}{[N_o + N_o e^{-0.157\,(2.015)}]/2} = 0.3137$$

This implies that the use of ^{57}Co is advantageous from sensitivity considerations.

Chan et al. [19] have shown that, to a first approximation, the statistical error in the void fraction measurement (neglecting geometric and flow regime related errors) may be expressed as

$$\epsilon_a \simeq \frac{1}{S\sqrt{N_a}} \tag{B.17}$$

Since the void fraction measurements are made at steady state, there is no constraint on the counting period. Assuming a 30 second counting period and an acceptable statistical error of 0.5% the required counting rate (N_R) may be determined from equation B.17 as

$$(N_R)_{^{137}Cs} = 44.81 \times 10^3 \text{ counts/sec}$$

and

$$(N_R)_{^{57}Co} = 13.55 \times 10^3 \text{ counts/sec}$$

The source strength (A) is estimated from the required counting rate as

$$A = \frac{N_R}{Gfe} \tag{B.18}$$

where f is the scintillator efficiency (100% for Na I(Tl)), e the source emission ratio and G is a geometric factor given by

$$G = T\,\Omega\,A_d \tag{B.19}$$

In equation B.19, T is the transmittance and may be approximated by the transmission ratio through the pipe (eqn. B.12). The solid angle factor (Ω) is given by

$$\Omega = \frac{1}{4\pi R^2} \tag{B.20}$$

and A_d is the effective detector area which is approximated by the collimator aperture area. This is assumed equal in length to the tube I.D. (25.65 mm) and 1/2" (12.7 mm) wide. The source-detector separation (R) is approximately 60 cm. Then, from equation B.18, B.19 and B.20, the required source strengths are

$$A_{^{137}Cs} = 1.14 \times 10^9 \text{ disintegrations/sec}$$

$$A_{^{57}Co} = 1.16 \times 10^9 \text{ disintegrations/sec}$$

These convert to 30.8 and 31.4 millicuries respectively. To account for further design requirements (aperture size, insulation etc.) source strengths of 100 mCi were recommended for both sources.

The shielding required to protect the experimenter is estimated from the following expression for dose rate (D)

$$D = A\,\Omega\,Q\,C \sum_i \left(\frac{\mu_t}{\rho_t}\right)_i T_i\, e_i\, E_i \tag{B.21}$$

where Q is the quality factor, which for gamma radiation is unity and C is a conversion factor to express the dose rate in mRem/h.

$$C = \frac{1000\,[\text{m Rem}]}{[\text{Rem}]} \; \frac{1.6021 \times 10^{-9}[\text{erg}]}{[\text{k eV}]} \; \frac{[\text{gm. rad}]}{100\,[\text{erg}]} \; \frac{3600\,[\text{s}]}{[\text{h}]} \tag{B.22}$$

The source strength (A) and solid angle factor (Ω) are as defined previously. The summation is carried out over the energy levels (E_i) emitted by the source, e_i is the corresponding emission ratio. T_i is the transmission ratio through the shielding material given by

$$T_i = e^{-\mu_{s_i} R} \tag{B.23}$$

where μ_{s_i} is the shielding material attenuation coefficient at the appropriate energy level and R is the shield thickness. The specific mass-energy absorption coefficient of human tissue is represented by $(\mu_t/\rho_t)_i$.

The maximum permissible annual whole body exposure as limited by the Atomic Energy Control Board, is set at 5 Rem. It is assumed that experiments are carried out over 20 weeks, 5 days per week and that the experimenter is in contact with the outside of the shield for 1 hour per day. The permissible dose rate is then given by

$$\frac{5}{20 \times 5 \times 1} = .05 \frac{\text{Rem}}{\text{hr}}$$

For design purposes a dose rate of .5 mRem per hour was used (S.F.~100).

For ^{137}Cs, treated as a mono-energetic emitter at 662 keV with stainless steel shielding, equation B.21 becomes

$$.5 = \frac{(.100)(3.7 \times 10^{10})}{4\pi R^2} (1)(57.68 \times 10^{-6})(.032)e^{-0.577R}(.851)(662)$$

From which R ≃ 14 cm. Similarly, the results for lead shielding and for ^{57}Co along with the estimated casket weights are shown in Table B.1.

Table B.1 - Shielding Thickness/Weight

	Stainless Steel	Lead
$^{137}C_s$	14 cm/190 kg	7 cm/45 kg
$^{57}C_o$	4.2 cm/10 kg	0.5 cm/1.0 kg

Although $^{137}C_s$ has a significantly longer half-life and is less expensive than ^{57}Co, a ^{57}Co was used for its higher sensitivity to void fraction changes and more practical shielding requirements. The stainless steel casket used is shown in Figure B.2. The reader is referred to Section 3.2.5 for a description of the signal processing system.

Figure B.2 Gamma Densitometer Source Casket

APPENDIX C

SATURATED WATER AND STEAM PROPERTIES

The empirical equations listed below were obtained by the least square method using the standard steam tables for pressures ranging from 1 to 10 bars. These equations are dimensional and SI units should be used throughout, i.e. $v = m^3/kg$, $h = kJ/kg$, $p = bar$, $\mu = Ns/m^2$, $\sigma = N/m$, $T = °C$, $Cp = kJ/kg°C$.

$$v_f = 0.99453 \times 10^{-3} + 48.7443 \times 10^{-6} (P)^{0.43503}$$

$$v_g = 3.6305672 \times 10^{-2} + 1.674019/P$$

$$v_{fg} = v_g - v_f$$

$$h_{fsat} = -127.422 + 545.254 (P)^{0.21265}$$

$$h_{fg} = 2474.56 - 217.561 (P)^{0.32378}$$

$$C_{Pf} = 4.11784 + 39.205 \times 10^{-4} (P)^{0.75965}$$

$$T_{sat} = -44.0965 + 143.7725 (P)^{0.19246}$$

$$\mu_f = 2.72737 \times 10^{-4} - 5.5749 \times 10^{-5} \ln (P)$$

$$\mu_g = 1.195 \times 10^{-5} + 1.314 \times 10^{-6} \ln (P)$$

$$\sigma = 7.5448 \times 10^{-2} - 1.3017 \times 10^{-4} T_{sat} - 3.5056 \times 10^{-7} T_{sat}^2$$

APPENDIX D

EXPERIMENTAL DATA

TABLE D.1

Single Phase Data

G_1 [kg/m^{2}s]	$\dot{m}_3/\dot{m}_1$	$(\Delta P_{2-1})_j$ [Pa]	$(\Delta P_{1-3})_j$ [Pa]
451.4	0.098	26.6	4.0
597.2	0.103	44.7	6.0
900.4	0.100	106.0	9.8
1213.6	0.098	176.6	13.0
448.4	0.305	64.5	0.3
599.8	0.301	113.4	−10.2
896.6	0.300	253.3	−12.5
1196.5	0.299	437.2	−3.3
447.5	0.504	81.7	16.9
599.8	0.500	149.4	22.0
900.1	0.502	327.2	55.6
1195.6	0.504	571.5	88.8
451.7	0.702	87.8	44.4
598.4	0.700	150.0	86.5
898.6	0.702	330.2	187.6
1181.8	0.702	573.9	326.6
451.6	0.905	78.8	95.5
599.4	0.903	140.3	163.0
897.9	0.904	306.5	375.7
449.4	1.000	75.8	127.3
598.1	1.000	128.3	217.0
896.9	1.000	285.7	472.7

Table D.2

Two-Phase Data for $G_1 = 450\ kg/m^2s$

$\dot{m}_3/\dot{m}_1$	G_1 [kg/m²s]	G_2 [kg/m²s]	G_3 [kg/m²s]	x_1	x_2	x_3	α_1	α_2	α_3	$(\Delta P_{2-1})_j$ [kPa]	$(\Delta P_{1-3})_j$ [kPa]	P_1 [kPa]
$x_1 = 4.7\%$												
0.115	445.9	394.8	51.1	.051	.044	.070	.879	.909	.867	0.685	−0.068	29.0
0.149	439.9	374.5	65.4	.049	.036	.126	.866	.918	.886	1.009	0.042	19.9
0.189	431.9	350.1	81.8	.051	.020	.190	.879	.874	.918	1.532	0.660	12.2
0.230	450.5	346.1	103.7	.045	.011	.169	.854	.865	.923	1.488	0.589	42.0
0.386	451.7	276.4	174.3	.043	.001	.112	.851	.017	.917	3.273	1.307	17.9
0.664	459.0	154.2	304.8	.044	.008	.063	.908	.120	.846	3.075	2.168	23.8
1.000	450.7	0.0	465.6	.046	.000	.043	.907	.091	.898	2.340	3.598	37.6
$x_1 = 15.2\%$												
0.077	446.8	412.4	34.4	.152	.129	.384	.977	.977	.957	2.693	0.004	88.8
0.105	454.4	406.5	47.9	.152	.113	.446	.991	.992	.968	4.877	0.379	73.3
0.160	447.5	376.0	71.4	.152	.079	.524	.976	.949	.982	8.241	2.489	35.4
0.220	454.6	354.7	99.9	.152	.067	.479	.981	.976	.976	9.755	4.921	37.8
0.297	452.4	316.6	134.4	.152	.049	.417	.988	.976	.969	11.580	7.302	52.5
0.453	450.6	246.5	204.1	.151	.012	.328	.987	.948	.984	11.023	11.923	75.3
0.603	442.7	175.6	267.2	.152	.004	.248	.979	.039	.979	11.303	14.999	88.0
1.000	411.1	0.0	417.3	.150	.000	.147	.995	.113	.955	9.580	17.694	105.9

Table D.3

Two-Phase Data for G_1 = 600 kg/m²s

$\dot{m}_3/\dot{m}_1$	G_1 [kg/m²s]	G_2 [kg/m²s]	G_3 [kg/m²s]	x_1	x_2	x_3	α_1	α_2	α_3	$(\Delta P_{2-1})_j$ [kPa]	$(\Delta P_{1-3})_j$ [kPa]	P_1 [kPa]
x_1 = 2.2%												
.073	601.5	557.8	43.7	.020	.019	.009	.804	.801	.909	0.240	−.120	30.7
.160	583.8	490.5	93.3	.023	.010	.067	.806	.816	.895	0.546	.271	17.6
.168	588.4	494.0	98.7	.021	.005	.093	.790	.685	.901	0.609	.494	12.8
.222	593.6	463.7	132.0	.025	.004	.106	.808	.739	.909	0.810	1.027	17.6
.402	620.6	369.2	249.7	.019	.001	.044	.804	.187	.860	1.839	1.015	14.0
.708	583.4	170.3	413.1	.025	.002	.034	.803	.080	.813	2.096	1.984	25.8
1.000	602.2	0.0	605.1	.023	.000	.023	.816	.042	.848	2.071	2.837	39.5
x_1 = 4.6%												
0.095	598.7	541.7	57.0	.045	.042	.043	.861	.883	.921	0.963	−0.184	54.1
0.125	596.1	521.6	74.6	.046	.034	.120	.878	.885	.933	1.419	−0.016	39.1
0.141	591.8	508.5	83.3	.046	.035	.124	.886	.852	.906	1.532	0.201	34.3
0.178	598.9	492.5	106.3	.045	.023	.162	.879	.894	.923	2.143	0.839	20.7
0.218	598.1	467.7	130.6	.044	.007	.173	.874	.766	.989	3.641	1.332	21.4
0.264	597.5	432.8	158.0	.046	.000	.171	.890	.067	.966	7.708	2.178	29.0
0.311	609.0	417.8	189.5	.049	.002	.157	.926	.072	.910	8.459	2.544	44.6
0.370	594.6	375.5	220.1	.047	.002	.121	.905	.045	.990	8.156	2.845	28.4
0.453	593.5	322.8	269.0	.048	.002	.103	.889	.020	.990	8.090	3.626	33.6
0.673	596.0	194.7	401.3	.045	.003	.065	.865	.031	.903	6.478	4.172	42.7
1.000	610.1	0.0	615.5	.045	.000	.044	.883	.007	.922	4.560	6.360	65.3
x_1 = 8.0%												
081	600.6	551.8	48.8	.080	.075	.089	.889	.915	.850	1.613	−.351	98.1
122	593.5	520.2	72.7	.081	.061	.203	.876	.976	.931	2.689	0.057	67.9
154	597.1	503.4	92.0	.079	.050	.229	.908	.942	.940	4.099	0.782	51.0
200	596.6	476.4	119.1	.081	.038	.244	.963	.898	.948	5.541	2.381	31.0
269	598.1	437.2	161.1	.083	.025	.256	.983	.875	.946	8.339	4.300	45.1
325	594.1	401.0	193.2	.081	.014	.231	.925	.878	.967	8.343	5.920	51.4
456	601.3	326.5	274.3	.078	.006	.170	.940	.104	.946	9.265	8.469	60.6
808	596.6	114.8	481.9	.081	.010	.098	.864	.062	.919	9.873	11.903	92.8
1.000	599.9	0.0	606.8	.080	.000	.079	.935	.153	.942	9.250	13.459	109.5

Table D.4

Two-Phase Data for G_1 = 900 kg/m²s

$\dot{m}_3/\dot{m}_1$	G_1 [kg/m²s]	G_2 [kg/m²s]	G_3 [kg/m²s]	x_1	x_2	x_3	α_1	α_2	α_3	$(\Delta P_{2-1})_j$ [kPa]	$(\Delta P_{1-3})_j$ [kPa]	P_1 [kPa]
x_1 = 2.0%												
0.107	901.6	801.9	96.0	.021	.018	.027	.749	.781	.860	0.806	0.362	59.2
0.140	892.4	765.0	125.4	.021	.012	.065	.780	.781	.939	1.216	0.266	44.9
0.179	907.5	744.3	163.0	.020	.008	.078	.787	.787	.921	1.346	0.731	30.9
0.242	901.9	680.0	218.6	.020	.001	.075	.779	.060	.914	4.144	1.465	38.5
0.313	907.6	620.5	284.8	.020	.001	.058	.776	.131	.926	4.579	1.940	32.1
0.490	896.6	451.2	439.1	.021	.001	.043	.784	.086	.882	4.815	3.354	36.7
0.664	906.9	296.1	602.1	.020	.000	.029	.784	.076	.835	3.952	3.969	49.3
1.000	898.1	0.0	898.1	.020	.000	.020	.807	.073	.845	3.538	4.852	81.3
x_1 = 4.3%												
0.125	873.0	760.9	108.8	.044	.040	.093	.831	.922	.892	2.048	0.030	96.3
0.147	901.2	767.4	132.4	.044	.035	.102	.911	.901	.874	2.720	0.380	87.3
0.222	888.8	689.9	196.9	.042	.017	.135	.888	.900	.942	4.792	2.478	36.0
0.294	890.7	625.6	261.7	.042	.003	.144	.824	.220	.956	11.930	5.027	49.3
0.357	905.9	580.4	323.0	.042	.006	.119	.913	.122	.936	13.815	5.892	56.7
0.445	902.9	494.9	401.9	.043	.004	.096	.864	.154	.921	13.265	6.913	67.0
0.608	883.8	343.1	537.2	.043	.004	.069	.905	.185	.900	11.401	8.145	80.7
1.000	826.6	0.0	823.7	.044	.000	.044	.869	.197	.898	7.210	10.928	114.5

Table D.5

Two-Phase Data for G_1 = 1200 kg/m²s

$\dot{m}_3/\dot{m}_1$	G_1 [kg/m²s]	G_2 [kg/m²s]	G_3 [kg/m²s]	x_1	x_2	x_3	α_1	α_2	α_3	$(\Delta P_{2-1})_j$ [kPa]	$(\Delta P_{1-3})_j$ [kPa]	P_1 [kPa]
x_1 = 2.0%												
0.122	1189.4	1045.0	144.6	.020	.017	.039	.780	.852	.880	1.249	0.488	102.4
0.169	1194.2	988.8	202.0	.020	.011	.065	.809	.847	.906	1.722	0.829	68.7
0.218	1191.2	930.2	259.4	.020	.007	.076	.772	.799	.935	2.159	2.021	41.2
0.267	1189.5	868.5	318.0	.020	.003	.076	.769	.062	.921	8.534	3.981	38.3
0.398	1198.5	712.3	477.5	.020	.003	.049	.778	.111	.901	7.695	5.511	51.6
0.655	1196.7	407.9	783.3	.020	.003	.032	.779	.053	.894	6.453	6.402	84.7